THE UNIVERSITY OF
WARWICK

AUTHOR: **Andrew James Turner** DEGREE: **Ph.D.**

TITLE: **Turbulence in the Solar Wind**

DATE OF DEPOSIT: .....

I agree that this thesis shall be available in accordance with the regulations governing the University of Warwick theses.

I agree that the summary of this thesis may be submitted for publication.

I **agree** that the thesis may be photocopied (single copies for study purposes only).

Theses with no restriction on photocopying will also be made available to the British Library for microfilming. The British Library may supply copies to individuals or libraries. subject to a statement from them that the copy is supplied for non-publishing purposes. All copies supplied by the British Library will carry the following statement:

> "Attention is drawn to the fact that the copyright of this thesis rests with its author. This copy of the thesis has been supplied on the condition that anyone who consults it is understood to recognise that its copyright rests with its author and that no quotation from the thesis and no information derived from it may be published without the author's written consent."

AUTHOR'S SIGNATURE: .....

USER'S DECLARATION

1. I undertake not to quote or make use of any information from this thesis without making acknowledgement to the author.
2. I further undertake to allow no-one else to use this thesis while it is in my care.

DATE SIGNATURE ADDRESS

.....

.....

.....

.....

.....

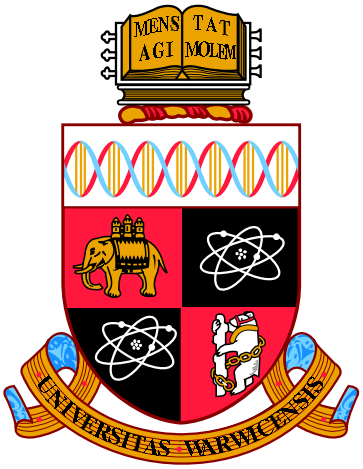

Turbulence in the Solar Wind

by

Andrew James Turner

Thesis

Submitted to the University of Warwick

for the degree of

Doctor of Philosophy

CFSA, Department of Physics

June 2013

THE UNIVERSITY OF
WARWICK

Contents

List of Figures

Acknowledgments

I would like to thank my supervisor, Prof. S. C. Chapman, for giving me the opportunity to undertake this period of research as well as for help and guidance throughout my PhD. I would also like to acknowledge my CFSA colleagues, particularly Girgol Gogoberidze for support, patience and many helpful and amusing discussions.

I wish to thank the STEREO, CLUSTER and Ulysses data teams for data provision and STFC for financial support provided throughout my PhD.

This thesis was typeset with LaTeX 2$_\varepsilon$[1] by the author.

[1] LaTeX 2$_\varepsilon$ is an extension of LaTeX. LaTeX is a collection of macros for TeX. TeX is a trademark of the American Mathematical Society. The style package *warwickthesis* was used.

Declarations

I declare that the work presented in this thesis is my own except where stated otherwise, and was carried out entirely at the University of Warwick, during the period of September 2009 to March 2013, under the supervision of Prof. S. C. Chapman. The research reported here has not been submitted, either wholly or in part, in this or any other academic institution for admission to a higher degree.

Some parts of the work reported in this thesis have been published, as listed below:

Published Papers

1. A. J. Turner, G. Gogoberidze, S. C. Chapman, B. Hnat and W. -C. Müller, Phys. Rev. Lett., **107**, 095002 (2011)

2. A. J. Turner, G. Gogoberidze and S. C. Chapman, Phys. Rev. Lett., **108**, 085001 (2012)

Oral Presentations

1. A. J. Turner, G. Gogoberidze, S. C. Chapman, B. Hnat and W. -C. Müller, *Nonaxisymmetric Anisotropy of the Inertial Range Power Spectrum*, Magnetosphere Ionosphere Solar-Terrestrial (MIST) Fall meeting (2011)

2. A. J. Turner, G. Gogoberidze, S. C. Chapman, B. Hnat and W. -C. Müller, *Nonaxisymmetric Anisotropy of the Magnetic Field Fluctuations in the Solar Wind Kinetic Range*, American Geophysical Union (AGU) Fall meeting (2011)

3. A. J. Turner, G. Gogoberidze, S. C. Chapman, B. Hnat and W. -C. Müller, *A Direct Test for Models of Magnetohydrodynamic Turbulence in the Solar Wind*, UK-Germany National Astronomy Meting (NAM) (2012)

4. A. J. Turner, G. Gogoberidze, S. C. Chapman, B. Hnat and W. -C. Müller, *Full Three-Dimensional Correlation Tensor as a Diagnostic of Turbulence and Discontinuities in the Solar Wind*, Meudon Turbulence Workshop (2012)

5. A. J. Turner, G. Gogoberidze and S. C. Chapman, *How do discontinuities Change Our Understanding of Turbulence in the Solar Wind?*, Magnetosphere Ionosphere Solar-Terrestrial (MIST) Fall meeting (2012)

Poster Presentations

1. A. J. Turner, K. H. Kiyani, S. C. Chapman, Y. V. Khotyaintsev and F. Sahraoui, *Variance Anisotropy of small-scale magnetic fluctuations in Solar Wind*, Magnetosphere Ionosphere Solar-Terrestrial (MIST) Fall meeting (2010)

2. A. J. Turner, G. Gogoberidze and S. C. Chapman, *Nonaxisymmetric Anisotropy of Solar wind Turbulence as a Direct Test for Models of Magnetohydrodynamic Turbulence*, American Geophysical Union (AGU) Fall meeting (2011)

3. A. J. Turner, G. Gogoberidze, S. C. Chapman, B. Hnat and W. -C. Müller, *The Solar Wind as a Turbulence Laboratory Some New Quantitative Points of Contact Between Theory, Simulation and Solar Wind observation*, European Geoscience Union (EGU) General Assembly (2012)

4. A. J. Turner, G. Gogoberidze and S. C. Chapman, *How do Discontinuities Affect Our Understanding of Solar Wind Turbulence?*, American Geophysical Union (AGU) Fall meeting (2012)

A. J. Turner

June 2013

Abstract

The solar wind provides a unique natural "laboratory" in which plasma turbulence may be investigated *in-situ*. Turbulence is statistically reproducible. Thus, in this thesis we investigate plasma turbulence in the solar wind through the statistical study of magnetic field observations. In particular, we investigate single-satellite time-series of the magnetic field.

We discuss hydrodynamic turbulence, and make parallels between hydrodynamic and magnetohydrodynamic turbulence. In hydrodynamic turbulence a unique scaling relation may be determined from dimensional analysis. Importantly, one may not derive a unique scaling relation for magnetohydrodynamic turbulence from dimensional analysis. Therefore, comparison of observations and turbulence models are key to determining the underlying physics for specific plasma parameters.

The inertial range is a range of scales over which energy cascades from large to small temporal-spatial scales. This thesis will predominantly be focused on the anisotropy and scaling of the inertial range within the solar wind. We investigate how sampling a solenoid field, i.e. $\nabla \cdot \mathbf{B} = 0$, with a single satellite produces an apparent nonaxisymmetry with respect to the background magnetic field. We also investigate how time-series discontinuities produced by non-turbulent structures alter the statistical analysis of various anisotropy measures. We will find that the commonly held picture of the solar wind, that specific temporal-spatial scales have a distinct physical origin, is an over simplified model. We will show that non-turbulent structures must be removed from the observations in order to analysis the statistics of the turbulence accurately. The work in this thesis helps to constrain theories of plasma turbulence where there is a background magnetic field with a greater magnitude than the root-mean-square magnitude of the turbulent fluctuations.

Chapter 1

Introduction

1.1 Introduction to Turbulence

Turbulence is a ubiquitous phenomenon in fluids. The study of turbulence has a long history in the hydrodynamic context, due to the abundance of hydrodynamic turbulence present on Earth, such as in the atmosphere, rivers and oceans. However, the study of electromagnetically conducting fluids is a relatively new area of research (e.g. see Alfvén [1942]; Kadomstev [1965] and references within). Consequently, the subject of plasma turbulence is not itself separate from hydrodynamic turbulence, as it calls upon the previous findings, knowledge and statistical measures albeit with differing governing equations. However, contrary to hydrodynamic turbulence, there is no requirement for universality in the equations of plasma turbulence.

We choose to start this thesis with a brief introduction to hydrodynamic history and theory. We will present the governing equations of hydrodynamics, highlight the significance of the dimensionless Reynolds number and show how the nonlinear effects manifest in Fourier space. We will then define what is meant by homogeneous, isotropic and stationary. We will introduce Taylor's Hypothesis, which is of crucial importance for most experimental investigations of turbulence, and then introduce the most famous hydrodynamic turbulence theory, that of Kolmogorov 1941. This will be followed by an introduction to magnetohydrodynamic (MHD) turbulence with the presentation of the governing equations of momentum and induction. We will present the Elsässer variables, which allow two variables to describe the coupled equations of velocity and magnetic field fluctuations. We will present the seminal MHD theories of Iroshnikov-Kraichnan and Goldriech-Sridhar, and note additional models of interest to the solar wind environment. For completeness we will conclude the introduction with a brief discussion of numerical simulations of

turbulence.

1.2 Hydrodynamic Turbulence

1.2.1 Hydrodynamic Background

We begin with the Navier-Stokes equation (Navier (1822), Stoke (1845)) of fluid dynamics. The Navier-Stokes equation builds on the previous work of Newton (1687), Bernoulli (1738) and Euler (1757). The Euler equations are derived by fulfilling the criteria of conserving mass, momentum and energy between fluid elements. This is equivalent to the Navier-Stokes equation in the absence of viscosity and heat transfer. The Navier-Stokes equation and incompressibility condition are presented under the conditions of a homogeneous, Newtonian, incompressible fluid without gravity or centrifugal force and for velocities smaller than the sound speed of the medium.

$$\rho\left(\frac{\partial \mathbf{v}}{\partial t} + (\mathbf{v}\cdot\nabla)\mathbf{v}\right) = -\nabla p + \mu\nabla^2\mathbf{v} \tag{1.1}$$

$$\nabla\cdot\mathbf{v} = 0 \tag{1.2}$$

where ρ is the density, $\mathbf{v}$ is the velocity, p is the pressure and μ is the dynamic viscosity. The left-hand-side of equation (1.1) is the inertia per volume and the right-hand-side is the divergence of stress.

In 1883 Osborne Reynolds published a paper on the transition to turbulence [Reynolds, 1883]. In order to understand the method and result of Reynolds it is necessary to conduct a dimensional analysis of equation (1.1), specifically the convective term $(\mathbf{v}\cdot\nabla)\mathbf{v}$, which is the source of the nonlinear interactions, and the viscous term $\frac{\mu}{\rho}\nabla^2\mathbf{v}$. This leads to

$$R_v = \frac{[(\mathbf{v}\cdot\nabla)\mathbf{v}]}{[\frac{\mu}{\rho}\nabla^2\mathbf{v}]} = \frac{V^2/L}{\nu V/L^2} = \frac{VL}{\nu} \tag{1.3}$$

where V is a characteristic velocity, L is a characteristic length-scale, ν is the kinematic viscosity and R_v is the kinetic Reynolds number.

It is not possible to know what result a specific Reynolds number will have on a hydrodynamic flow from equation (1.1) alone. A simple attempt to understand critical values for the onset of turbulence from theory is to estimate the time-scale for perpendicular fluctuations to cross from one side of a pipe to the other as, $\tau_\perp \sim D/v_\perp$ and the diffusion time-scale $\tau_\nu \sim D^2/\nu$. Therefore, if $\tau_\nu/\tau_\perp \sim v_\perp D/\nu > 1$ perpendicular fluctuations are able to cover the cross-section of a pipe of diameter

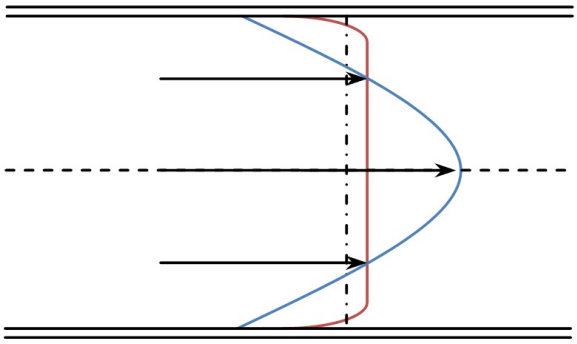

Figure 1.1: Schematic representation of flow in a tube that is laminar or turbulent. The blue velocity profile is for a laminar profile. The red velocity profile is for a turbulent profile. The vertical dot-dash line represents the average of the flow profiles for both the turbulent and laminar case. These profiles represent the fully-developed case, such that the profile does not change with time or distance along the tube.

D without being dissipated [Lesieur, 1997].

Reynolds was able to determine experimentally the values of equation (1.3) that lead to turbulence by systematically varying the flow speed of fluid and altering the diameter of tubes. He found that a hydrodynamic flow will remain laminar for $R_v < 2000$, there is a transition to turbulence in the region of $2000 \leq R_v \leq 4000$ and turbulence will result for $R_v > 4000$. The universality of the Reynolds number for the onset of turbulence has been central to nautical, aeronautical and automotive design and development, as it allows models of various aspect ratios to behave like the final product with respect to turbulence.

Interestingly, it is not only the apparent flow behavior that changes when the flow becomes turbulent, as seen by injecting dye into a tube, but the fully developed cross-sectional flow profile in a tube is fundamentally changed. A laminar flow (i.e. $R_v < 2000$) has a well defined parabolic cross-sectional profile known as a Hagen-Poiseuille flow. This is defined as $v(r) = v_c[1 - (\frac{r}{R})^2]$, where v_c is the velocity at the center of a tube, r is the distance from the center of the tube and R is the Radius of a tube [Sutera and Skalak, 1993]. Conversely, when $R_v > 4000$ the cross-sectional profile is characterized by strong gradients at the boundaries and approximately flat for the majority of the tube cross-section, such that $v_{m,t} - v_{av,t} < v_{m,l} - v_{av,l}$, where subscript av, m, l and t denote average, maximum, laminar and turbulent respectively. A schematic of this is shown in Fig. 1.1.

1.2.2 Fourier Transform of Navier-Stokes Equation

It is generally useful in the context of homogeneous turbulence to consider Fourier-space instead of configuration space. Here we will show the Fourier transform of the Navier-Stokes equation under the incompressibility condition. The linear terms of equation (1.1) are simple to Fourier transform. The nonlinear term requires slightly more care and yields important information regarding the nonlinear interactions. The nonlinear term, $(\mathbf{v}\cdot\nabla)\mathbf{v}$, is a product operation in configuration space. Thus, in Fourier space the nonlinear term is a convolution, which we express by summing repeated indices using Einstein convention, such that $\mathcal{F}((\mathbf{v}\cdot\nabla)\mathbf{v}) = \mathcal{F}(v_j\frac{\partial v_i}{\partial x_j}) = \mathcal{F}(\frac{\partial v_j v_i}{\partial x_j}) = ik_j\int_{\mathbf{p}+\mathbf{q}=\mathbf{k}}\tilde{v}_i(\mathbf{p},t)\tilde{v}_j(\mathbf{q},t)d\mathbf{p}$, where $\mathbf{q}=\mathbf{k}-\mathbf{p}$ and $\mathcal{F}$ denotes the Fourier transform operator. It is clear from this transform that interactions occur between triads of wave vectors. In the literature (e.g. see Diamond et al. [2010] and references within) the nonlinear interactions are separated into two different classes; a) local interactions where all three wave vectors are of approximately the same magnitude b) nonlocal interactions where there is a large difference in the magnitude of two wave vectors with respect to the remaining wave vector. Throughout the thesis we will only consider the case of local interactions.

For completeness we present the full Fourier transform in the plane perpendicular to the wave vector $\mathbf{k}$ for the incompressible Navier-Stokes equation. We note that due to the incompressibility condition, $\mathcal{F}(\nabla\cdot v(\mathbf{x},t)) = \mathbf{k}\cdot\tilde{\mathbf{v}}(\mathbf{k},t) = 0$. Therefore, nonlinear interactions occur only in the perpendicular plane with respect to the wave vector. Thus we use the perpendicular projection operator, defined $\Pi_{ij}(\mathbf{k}) = (\delta_{ij} - \frac{k_i k_j}{k^2})$, to describe the Fourier transformed Navier-Stokes equation with nonlinear interactions

$$\left(\frac{\partial}{\partial t} + \nu k^2\right)\tilde{u}_i(\mathbf{k},t) = ik_m\Pi_{ij}(\mathbf{k})\int_{\mathbf{p}+\mathbf{q}=\mathbf{k}}\tilde{v}_j(\mathbf{p},t)\tilde{v}_m(\mathbf{q},t)d\mathbf{p} \tag{1.4}$$

1.3 Statistical Definitions

Turbulent systems contain many degrees of freedom, such that three-dimensional turbulence may be shown to contain approximately $R_v^{9/4}$ degrees of freedom [Lesieur, 1997; Batchelor, 1953]. As highlighted in Section 1.2.1, for turbulence to exist R_v must exceed $\mathcal{O}(10^3)$, so the degrees of freedom must exceed $\mathcal{O}(10^7)$. Thus, given observations at time t it is not possible to predict the observations at $t+\tau$, due to the many degrees of freedom.

The mathematical description defines a sample space and allows the velocity, $\mathbf{v}(\mathbf{x},t)$, to be a random function within this space. Under such a treatment one con-

ducts an experiment , which corresponds to studying a point in sample space (e.g. a hot-wire observation of wind velocity). One then repeats N times and considers ensemble averages preformed over independent realizations. Using ergodic theory as $N \to \infty$ the system mean quantities are determined. Therefore, the study of turbulence lends itself to statistical study over many independent ensembles to understand the probabilistic nature of the system. Here we introduce and explain some of the statistical language required and the practical concept of Taylor's hypothesis.

1.3.1 Homogeneous

An important concept for the theory of turbulence is homogeneity, i.e. the mean quantities built with a set of n points in coordinate space are invariant under any spatial translation of the set. Such that

$$\langle u_{\alpha,1}(\mathbf{x}_1, t_1)...u_{\alpha.n}(\mathbf{x}_n, t_1)\rangle = \langle u_{\alpha,1}(\mathbf{x}_1 + y, t_1)...u_{\alpha.n}(\mathbf{x}_n + y, t_1)\rangle. \tag{1.5}$$

This implies that the second-order correlation tensor is given as

$$U_{ij}(\mathbf{r}, t_1, t_2) = U_{ji}(-\mathbf{r}, t_1, t_2) = \langle u_i(\mathbf{x}_1, t_1)u_j(\mathbf{x}_1 + \mathbf{r}, t_2)\rangle. \tag{1.6}$$

1.3.2 Isotropic

Mean quantities built with a set of n points in coordinate space are invariant under any number of simultaneous rotations. Is should be noted that the condition of isotropy is a stricter condition than that of the homogeneous criteria, as any translation my be decomposed by two simultaneous rotations [Lesieur, 1997]. A random function that is isotropic leads to the condition that the spatial average is zero, such that $\langle v(\mathbf{x}, t)\rangle = 0$. Therefore, the first nontrivial correlation is the second-order correlation tensor if isotropy is assumed, such as far from a boundary or interface in hydrodynamic turbulence.

1.3.3 Stationary

Stationary is a temporal analogue to the spatial homogeneous condition, such that the mean quantities for n points in coordinate space are invariant under any temporal translation of the set. Such that

$$\langle u_{\alpha,1}(\mathbf{x}_1, t_1)...u_{\alpha.n}(\mathbf{x}_1, t_n)\rangle = \langle u_{\alpha,1}(\mathbf{x}_1, t_1 + \tau)...u_{\alpha.n}(\mathbf{x}_1, t_n + \tau)\rangle. \tag{1.7}$$

The condition shown in equation 1.7 is referred to as "strong" stationarity. Strong stationarity applies only if equation 1.7 is true for all moments. Usually in the context of signal analysis only the first and second moments are required to be stationary, this is referred to as "weak" stationarity (e.g. see [Paschmann and Daly, 1998; Ghil et al., 2002] and references within). The stationary condition implies that the mean kinetic energy per unit mass is independent of time. In reality such a condition may only be realized if there is a constant forcing to balance the effect of dissipation from the Navier-Stokes equation. The stationary condition is the fundamental difference between turbulence that is modeled as freely-decaying or forced.

1.3.4 Taylor's Hypothesis

In 1938 G. I. Taylor published a paper that would have widespread experimental/observational use. Originally formulated in the context of hydrodynamic turbulence, where generally it is possible to transform to the reference frame of the flow without affecting the properties of the turbulent fluctuations, it was hypothesized that observations recorded at a fixed point in space, as a time-series, may be considered as measuring the spatial pattern of turbulence without temporal evolution [Taylor, 1938]. This is known as the "frozen-in" condition. This has clear application in the context of wind tunnels, where the mean flow velocity is much greater than the root-mean-square fluctuations of the flow.

1.3.5 Kolmogorov 1941 theory (K41)

Here we will concern ourselves only with the predicted energy spectrum of the inertial range, leaving such features as intermittency to Chapter 2. Consider isotropic turbulence that is stationary, such that there is a large-scale forcing and a small-scale dissipation. Assume that the separation between the forcing-scale, k_i, and the dissipation-scale, k_d, is large. Therefore, the Reynolds number is large, not only to induce turbulence but to extend the inertial range of nonlinear energy cascade (the relation $R_v^{9/4} \sim (k_i/k_d)^3$ [Lesieur, 1997] for isotropic turbulence requires that a greater inertial range results from a larger Reynolds number). As the turbulence is stationary the input energy at the forcing-scale is equal to the output energy at the dissipative scale.

The original Kolmogorov theory of isotropic turbulence is constructed under the assumption of stationarity, such that the energy flux through nonlinear interactions is independent of $\mathbf{k}$ and equal to the viscous dissipation rate, ϵ. Another key

assumption is that of a local cascade introduced by Richardson [1926]. This condition means that in order for energy to move from $k_i \rightarrow k_d$ it must be transfered through all intermediate k. Therefore, providing the intermediate k are completely free of forcing and/or dissipative effects they may be considered indistinctive/self-similar as they are independent of the particular details of the forcing or dissipative physics.

With the previous *a priori* assumptions it is possible to predict the energy spectrum as a function of $\mathbf{k}$ (or as a function of k due to the isotropic condition). One needs to solve $E(k) \sim \epsilon^{\alpha} k^{\beta}$, where α and β are exponents that must lead to the correct physical dimensions for kinetic energy spectrum. The energy per wavenumber, $E(k)$, has the dimensions of $[L]^3[T]^{-2}$. The dissipation rate, ϵ, is the energy per second, with dimensions of $[L]^2[T]^{-3}$. Therefore, the equation $[L]^{2\alpha-\beta}[T]^{-3\alpha} = [L]^3[T]^{-2}$, must be solved for α and β. The unique solution is that, $\alpha = 2/3$ and $\beta = -5/3$. Thus, we arrive at the result of the Kolmogorov 1941 theory, that the energy spectrum as a function of wavenumber in the inertial range of isotropic stationary turbulence goes as

$$E(k) = C_k \epsilon^{2/3} k^{-5/3}, \tag{1.8}$$

where C_k is called the Kolmogorov constant, which must be found experimentally and has a typical value of 1.7 ± 0.2 [Bohr et al., 1998]. Note that this relation for $E(k)$ may also be found by considering the nonlinear time from the triple-velocity correlation function, as done by Oboukhov [1941].

1.4 Magnetohydrodynamic (MHD) Turbulence

A plasma is an ionized gas, such that a simple plasma has a composition of equal numbers of electrons and ions. In order to describe the system completely the position and velocity of all particles must be known and evolved in time. However, analogous to hydrodynamic, it is possible to construct macroscopic quantities, such as temperature, density, average velocity and pressure, which allows the large-scale plasma dynamics to be evolved. The simplest of such fluid-like representations is that of magnetohydrodynamics, which is a one-fluid model applicable at scales larger than the characteristic scales of the particle dynamics within the plasma.

Characteristic plasma scales are the Debye-length, the ion-cyclotron frequency and the effective Hall length. The Debye length is related to a sphere of influence, where charge interactions between individual particles are important. The Debye length may be written as, $l_D = \sqrt{\epsilon_0 k_B T / n e^2}$, where ϵ_0 is the permittivity

of free-space, k_B is the Boltzmann constant, T is the temperature, n is the number density and e is the electron charge. The ion-cyclotron frequency is the inverse time required for an ion to complete one gyration around the magnetic field. The ion-cyclotron frequency may be written as $\omega_{i,c} = q_i B/m_i$, where q_i is the charge of the ion, B is the magnetic field magnitude and m_i is the mass of the gyrating ion. By substituting the ion mass for the electron mass it is possible to see that the electrons gyrate at a much faster rate than the ions, such that if one wants to consider a one-fluid model it is necessary to only consider temporal scales much longer than the ion-cyclotron frequency.

The generalized Ohm's law in the absence of the electron inertia term may be written as

$$\mathbf{E} = -(\mathbf{v} \times \mathbf{B}) + \frac{\mathbf{j}}{\sigma} + \frac{1}{en_e}(\mathbf{j} \times \mathbf{B}) - \frac{1}{en_e}\nabla p_e, \tag{1.9}$$

where $\mathbf{E}$ is the electric field, $\mathbf{v}$ is the bulk velocity, $\mathbf{B}$ is the magnetic field, $\mathbf{j}$ is the electric current density, σ is the electrical conductivity, e is the electron charge, n_e is the electron number density and p_e is the electron pressure. The individual terms on the RHS of equation 1.9 are called the Induction, Ohmic, Hall and Battery term respectively. The Hall term is negligible when the length-scale, L, is large enough that the ions perform many gyro-rotations per Alfvén transit time, such that $L \gg v_A/\omega_{c,i}$, where v_A is the Alfvén velocity. In Goossens [2003] it is demonstrated that for parameters comparable to those found in the solar wind the relative importance of the Ohmic, Hall and Battery term as a fraction of the Inertial term at large scales ($L = 10^6\ m$) is $10^{-12}, 0.1, 10^{-2}$ respectively.

This implies a minimum length-scale for which the MHD model is applicable. The smallest-scale considered must be greater than $v_A/\omega_{c,i}$. There is no upper length-scale or temporal-scale for the MHD model, as the conditions for validity becoming increasingly well satisfied as $L \to \infty$ and $T \to \infty$ [Krall and Trivelpiece, 1973; Goossens, 2003]. Note that formally the MHD model assumes a nearly Maxwellian distribution function for ions and electrons due to collisions. Therefore, the MHD model requires that the collisional time-scale is much less than the global time-scales of the system. However, if a collisionless plasma is incompressible then the magnetic field may preform the role of collisions, such that the MHD model may be used.

We may now write the fluid equations for a conducting medium. The continuity (mass conservation) and incompressible equations ($\nabla \cdot v = 0$) of hydrodynamics are unchanged for MHD. Under the condition of incompressibility ($\nabla \cdot v = 0$) the

MHD momentum, induction and solenoid equations are as follows

$$\frac{\partial \mathbf{V}}{\partial t} + (\mathbf{V}\cdot\nabla)\mathbf{V} - (\mathbf{B}\cdot\nabla)\mathbf{B} = -\nabla P + \nu\nabla^2\mathbf{V} \tag{1.10}$$

$$\frac{\partial \mathbf{B}}{\partial t} + (\mathbf{V}\cdot\nabla)\mathbf{B} - (\mathbf{B}\cdot\nabla)\mathbf{V} = \eta\nabla^2\mathbf{B} \tag{1.11}$$

$$\nabla\cdot\mathbf{B} = 0 \tag{1.12}$$

where $P = \frac{1}{\rho}(p+\nabla B^2/(2\mu\rho))$, $\mathbf{B}$ is the magnetic field and η is the magnetic magnetic diffusivity.

It can be seen from equation (1.10) and equation (1.11) that the magnetic field and velocity are coupled. A more informative way of expressing these equations is to rewrite them using a coupled variable, know as the Elsässer variable, such that $\mathbf{z}^{\pm} = \mathbf{v} \pm \mathbf{b}$, where the magnetic field is expressed in units of Alfvén velocity, $V_A = B/\sqrt{\mu_0\rho_0}$. Elsässer variables are the eigenfunctions of noninteracting and counter-propagating Alfvén waves that satisfy the incompressible MHD equations [Elsässer, 1950]. The incompressible MHD equations may be rewritten in terms of Elsässer variables by using $\mathbf{V} = \mathbf{V}_0 + \mathbf{v}$ and $\mathbf{B} = \mathbf{B}_0 + \mathbf{b}$, where the bulk velocity and background magnetic field are denoted $\mathbf{V}_0$, $\mathbf{B}_0$ and the fluctuations of the velocity and magnetic field are denoted $\mathbf{v}$, $\mathbf{b}$ respectively. With substitution for $\mathbf{V}$ and $\mathbf{B}$ and subtraction (addition) of equation (1.11) from (to) equation (1.10) the MHD equations in terms of Elsässer variables may be written as

$$\frac{\partial \mathbf{z}^{\pm}}{\partial t} \mp (\mathbf{B}_0\cdot\nabla)\,\mathbf{z}^{\pm} + \left(\mathbf{z}^{\mp}\cdot\nabla\right)\mathbf{z}^{\pm} = -\nabla P + \frac{1}{2}\left(\xi_-\nabla^2\mathbf{z}^{\mp} + \xi_+\nabla^2\mathbf{z}^{\pm}\right) \tag{1.13}$$

where $\xi_{\pm} = \nu \pm \eta$. The second term on the LHS of equation (1.13) implies that there is no coordinate system that may be constructed to remove the dynamics of the background field, $\mathbf{B}_0$.

1.4.1 Iroshnikov-Kraichnan Theory (IK)

Here we present a derivation for the inertial range spectrum of MHD turbulence under the assumption of isotropy, which was first presented by Iroshnikov [1963] and Kraichnan [1965]. We consider the nonlinear part of equation 1.13. The first observation is that for a cascade to take place oppositely traveling Elsässer variables are required. We have assumed that the plasma is incompressible. Therefore, the envisaged scenario is of counter-propagating Alfvén waves, $\mathbf{z}^{\pm}$, interacting to form an inertial range. We now consider the characteristic time-scale for nonlinear

interactions

$$\left(\frac{\partial \mathbf{z}^{\pm}}{\partial t}\right)_{nonlinear} = \left(\mathbf{z}^{\mp} \cdot \nabla\right) \mathbf{z}^{\pm} \tag{1.14}$$

By using dimensional analysis and the condition of local interactions, we can estimate a time-scale of interaction as, $\tau \sim [zk]^{-1}$, where z is in units of velocity and may be written as $z = \sqrt{(}v_0^2 + b_0^2)$, where b_0 and v_0 are the root-mean-square of the magnetic field and velocity fluctuations, in units of velocity, such that b_0 may be expressed in terms of the Alfvén velocity if desired. Therefore, if one considers the case of a strong background magnetic field the time-scale of interaction may be expressed as, $\tau \sim [b_0 k]^{-1}$.

Now we conduct the full dimensional analysis, as was done in Section 1.3.5. We use the following quantities; the energy dissipation rate $\epsilon = [L]^2[T]^{-3}$, propagation velocity $b_0 = [L][T]^{-1}$, wavenumber $k = [L]^{-1}$ and the energy per wavenumber $E(k) = [L]^3[T]^{-2}$. We use the starting point that $\epsilon \sim b_0^{\alpha} k^{\beta} E(k)^{\gamma}$. Therefore, we have the two equations to solve, $\alpha - \beta + 3\gamma = 2$ and $2\gamma + \alpha = 3$. Under the phenomenology that $\alpha = 1$, i.e. there is one externally applied characteristic velocity [Iroshnikov, 1963; Kraichnan, 1965], one finds a solution for the energy spectra,

$$E(k) = C_{Ik}(\epsilon b_0)^{1/2} k^{-3/2}, \tag{1.15}$$

where C_{IK} is a constant to be found experimentally.

Iroshnikov [1963] and Kraichnan [1965] reasoned that if one uses the viral theorem the magnetic and kinetic energy for Alfvén waves is expected to be equal. Thus, if there is a negligible magnetic field to kinetic energy in the scales larger than the inertial range the characteristic time-scale is that of velocity fluctuations, $\tau \sim [v_k k]^{-1}$. Thus, by removing the background magnetic field and forcing the system with kinetic energy at scales larger than the inertial range returns the K41 cascade [Iroshnikov, 1963; Kraichnan, 1965]. This has been found in simulations (e.g. see Biskamp [2003]; Müller and Grappin [2005] and references within). Therefore, it may be seen that the addition of a background magnetic field reduces the strength of the nonlinear cascade from large-scales to dissipation scales.

1.4.2 Goldreich-Sridhar Theory (GS)

Goldreich and Sridhar [1995] presented the first anisotropic theory for the inertial-range of MHD turbulence. As highlighted in section 1.4.1 there are two principal time-scales that may be considered for MHD turbulence. The linear time-scale proportional to the magnetic field strength, corresponding to the Alfvén wave period,

and the nonlinear time-scales proportional to the intensity of velocity/magnetic field nonlinear interactions. Their key assumption was to consider the case where the nonlinear and linear time-scale are equal, a criteria known as "critical balance". It is assumed that the nonlinear cascade is purely two-dimensional in the perpendicular plane and has the characteristics of three-dimensional hydrodynamic turbulence, such that the energy spectra in the perpendicular plane is proportional to $k_\perp^{-5/3}$. We will present a dimensional analysis that returns the key result that $k_\parallel \sim k_\perp^{2/3}$. We will then state the reduced one-dimensional energy spectra for the perpendicular and parallel wave vectors predicted by the GS model.

We start by stating the perpendicular time-scale, $\tau_\perp \sim [v_\perp k_\perp]^{-1}$, and the parallel time-scale, $\tau_\parallel \sim [v_A k_\parallel]^{-1}$. The next step is to equate the two time-scales, which corresponds to the distance that the perpendicular plane must be advected in the parallel direction before a loss of correlation, $v_A k_\parallel \sim v_\perp k_\perp$. We note that the fluctuations in the perpendicular plane are exactly the same as those in three-dimensional hydrodynamic turbulence, such that $v_\perp \sim k_\perp^{-1/3}$. Therefore, one arrives at the relation that $k_\parallel \sim k_\perp^{2/3}$. For dimensional consistency this may be written as $k_\parallel \sim k_\perp^{2/3} k_0^{1/3}$, where k_0 is the inverse length scale at the beginning of the inertial range. Isotropy is assumed between $k_\perp$ and $k_\parallel$ at the beginning (lowest wavenumber) of the inertial range.

Goldreich and Sridhar [1995] wrote the three-dimensional energy spectrum as

$$E(k_\perp, k_\parallel) = C_{GS} \frac{v_A^2}{k_\perp^{10/3} L^{1/3}} g\left(\frac{k_\parallel L^{1/3}}{k_\perp^{2/3}}\right), \tag{1.16}$$

where C_{GS} is a dimensionless constant, L is a the energy containing length-scale, such that $g(\alpha)$ is a dimensionless quantity, $g(\alpha)$ is some function that has the property $\int g(\alpha) d\alpha = 1$. By integrating the three-dimensional energy spectrum one can obtain the one-dimensional energy spectrum for either $k_\parallel$ or $k_\perp$ (e.g. See Tessein et al. [2009]), which scale as $E(k_\perp) \sim k_\perp^{-5/3}$ and $E(k_\parallel) \sim k_\parallel^{-2}$. It may be noted that the GS theory is in contradiction to the IK theory.

1.4.3 Other MHD Turbulence theories

The IK and GS MHD turbulence theories represent pioneering models for the isotropic and anisotropic case respectively. However, there are many more theories of MHD turbulence that are noteworthy and of particular interest to the solar wind. These may be separated into strong and weak turbulence models, as well as balanced and imbalanced. The term "strong" or "weak" refers to the whether there is a resonant condition that limits the volume of interacting wave vectors, such that

for strong turbulence no resonance criteria is needed. For more information on the distinction between strong and weak MHD turbulence see Kadomstev [1965]; Galtier et al. [2000]; Gogoberidze et al. [2009].The term "balanced" or "imbalanced" refers to whether there is an equal amount of energy in the cascade for both Elsässer variables, $\mathbf{z}^{\pm}$. More information on imbalanced MHD turbulence theories can be found in Lithwick et al. [2007]; Beresnyak and Lazarian [2008]; Chandran [2008]; Perez and Boldyrev [2009].

Strong balanced theories, in addition to IK and GS, include; Boldyrev [2005] suggested that the turbulent eddies are three-dimensionally anisotropic with a $E(k_\perp) \sim k_\perp^{-(5+\alpha)/(3+\alpha)}$ where $\alpha = 0$ for K41 and $\alpha = 1$ for IK, Gogoberidze [2007] suggested that MHD turbulence may be capable of displaying both K41 and IK spectra due to the presence of both local and nonlocal interactions, Grappin et al. [2012] proposed a "quasi-isotropic" cascade, such that the $k_\parallel$ and $k_\perp$ spectral exponents are equal but the power is not equal in both directions.

1.5 Introduction to the Solar Wind

The Sun is a typical G2 main-sequence star. Therefore, the study of the Sun and solar wind is likely to be of relevance to other solar-type systems [Cassinelli, 1979]. Observations of sunspots, which are areas of enhanced magnetic field, have been conducted since as early as approximately 165 B.C. However, it is the routine measurements from 1750 to the present day that illustrate the variable nature of the Sun [Stephenson, 1990]. The observations of sunspots have revealed several characteristic time-scales associated with the Sun. These are the solar rotation, which has a period of approximately 28 days (the corresponding frequency may clearly be seen in the radial component of *in-situ* magnetic field measurements), and the "solar cycle", which from the sun-spots record may be seen as a prominent oscillation of approximately 11 years. The 11 year cycle can be seen in Fig. 1.2, which on the bottom panel shows the daily sunspot area per day averaged over a 28 day period against time. The top panel of this figure shows the characteristic movement of sunspots from large latitudes to the equator as the solar cycle progresses to completion.

The Sun is not limited to variations on the temporal-scales of days and years and spatial-scale of Sun-spots. The outer regions of the Sun display spatial-temporal variation on all scales, such as; the granulation and supergranulation pattern of convective cells on the photosphere, regions of open and closed magnetic field that demonstrate structure across a broad range of observational scales and event-like phenomena, such as micro-flares, flares and coronal mass ejections. A demonstra-

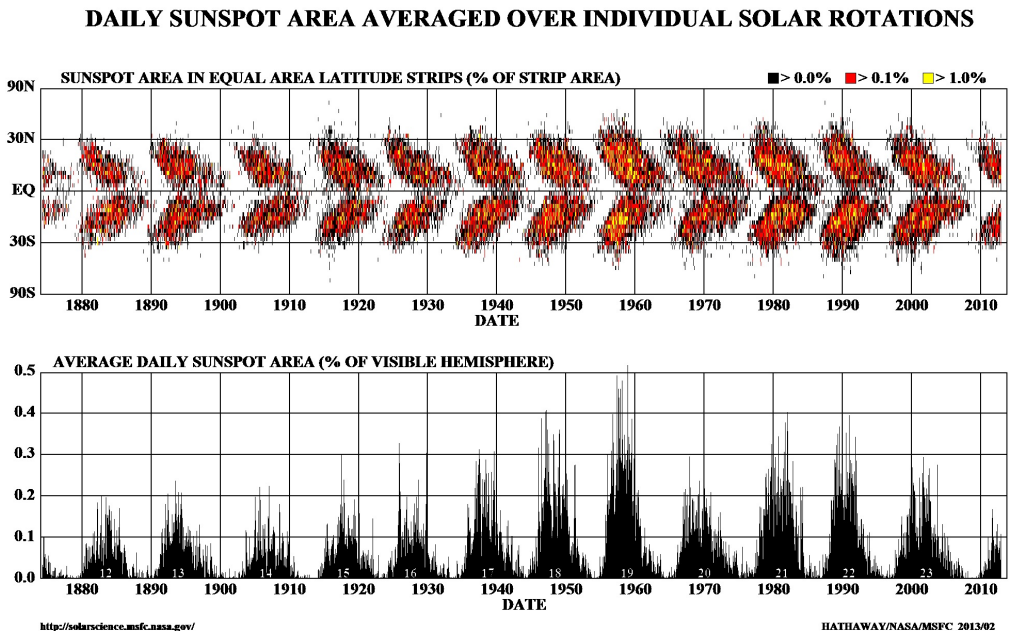

Figure 1.2: Sunspot History. Top panel: Sunspot density as a function of latitude. Bottom panel: Day sunspot percentage averaged over a solar rotation period.Plot courtesy of NASA online resources. NASA [2013a]

tion of the large range of structural scales observed on the solar surface is presented in Fig. 1.3, which is an adaptation from Borovsky [2008]. All of these constitute the constantly evolving spatial-temporal magnetic field produced at the Sun, which is carried into the interstellar medium by the expansion of the corona, known as the solar wind. The high degree of spatial variability can be seen at different wavelengths, corresponding to emission at different altitudes, in Fig. 1.4.

Generally, the coronal magnetic field depends upon the stage at which the Sun is at within the 11 year cycle. At Solar minimum there is a tendency for the global magnetic field to be well characterized by a dipolar field. The dipolar magnetic field produces coronal holes (regions of open magnetic field lines observed as dark regions due to the low density of particles) over the large latitudes of both the poles. The equatorial plane is usually a complex ensemble of open and closed magnetic field regions. However, this complex region expands to cover increasing latitudes of the Sun as the solar cycle moves from minimum to maximum, filling the coronal holes.

The hot corona of the Sun cannot be in thermal equilibrium with the surrounding interstellar medium, as it is a hot plasma with a density much greater than the interstellar medium. Therefore, there must be a flow of material from the solar

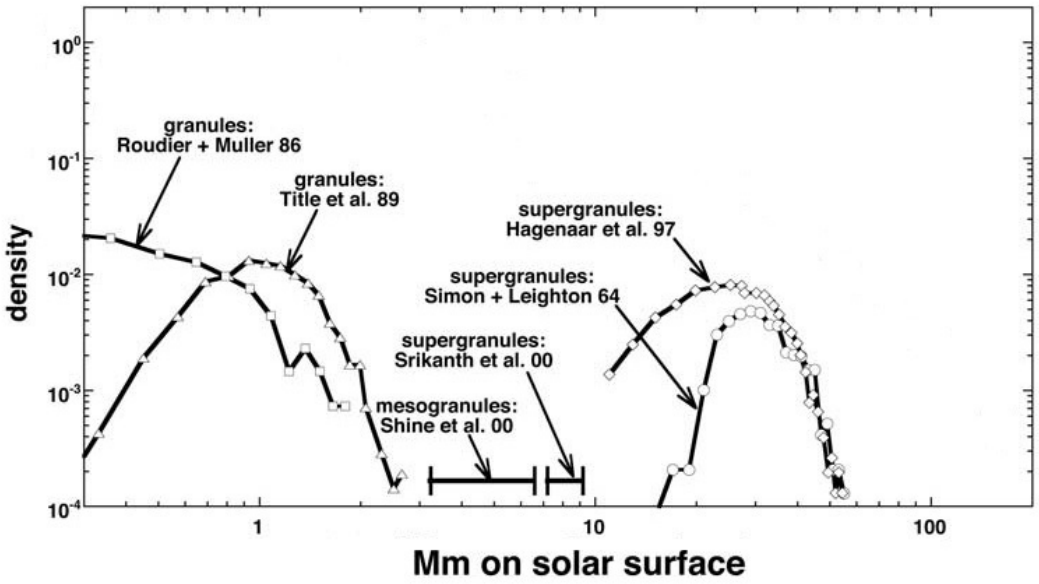

Figure 1.3: This is an adaptation of figure 11 from Borovsky [2008]. The probability density vs. scale in Mm of structures on the solar surface are displayed by collating the studies of Simon and Leighton [1964]; Roudier and Muller [1986]; Title et al. [1989]; Haganaar et al. [1997]; Srikanth et al. [2000]; Shine et al. [2000]

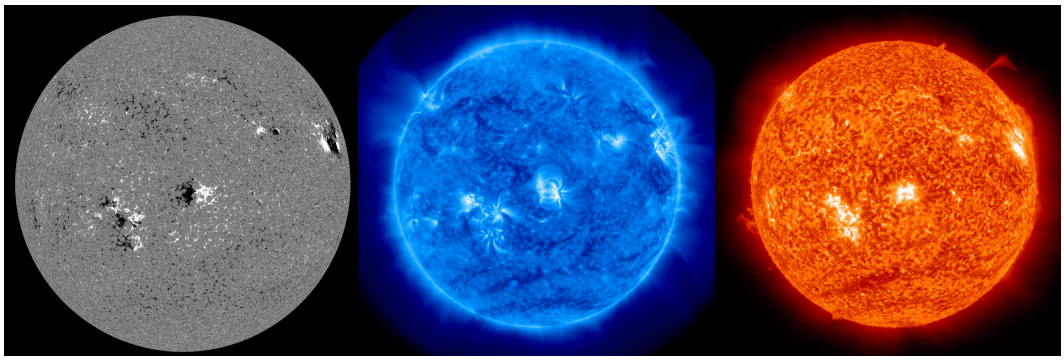

Figure 1.4: The Sun. Left: Magnetogram produced by Zeeman splitting displays the "magnetic carpet" of the photosphere, where white and black represent inward and outward magnetic field. Middle and Right: observation at 171 and 304 Å. Plot courtesy of NASA online resources. NASA [2013b].

surface to a point where the pressure of the solar particle flow equals the pressure of the interstellar medium [Goossens, 2003]. This flow of material is called the solar wind. The velocity of such a solar wind was not obvious, however Parker predicted a wind speed of a few hundreds of km/s at the Earth's orbit by using a stationary equilibrium condition [Parker, 1958]. Parker also predicted an Archimedean spiral for the marcoscale magnetic field in the interplanetary medium due to the solar rotation. By 1962 extended *in-situ* measurements had confirmed that the solar wind was continuous [Goossens, 2003]. The Solar wind has been found to vary from $300-800\ km/s$, where a flow below 400 km/s is refereed to as slow and a flow speed above 500 km/s is said to be fast. Slow wind seems to originate from closed field regions, whilst fast wind comes from coronal holes. In addition to the flow velocity of the wind, slow solar wind is characterized by larger particle number densities and larger ratios of O^{6+}/O^{7+} than fast solar wind (e.g. see Perri and Balogh [2010] and references within). The mechanism for solar wind acceleration is still unknown for fast wind. Fast wind is generally used for solar wind turbulence studies due to the increasingly well realized Taylor's hypothesis and the generally less structured composition, often referred to as "clean" solar wind.

1.6 Scaling in the Solar Wind

The first in-situ measurements of the solar wind that suggested turbulence were analyzed by Coleman [1968]. In this paper Coleman analyzed the velocity and magnetic field measurements of the Mariner 2 satellite across a frequency range of approximately 32 days to 75 seconds in the ecliptic plane at approximately 1 A.U. The noise of in the power spectral density of the magnetic field exists for approximately $f > 4 \times 10^{-3}$ Hz, corresponding to approximately 4 minutes. It was determined that turbulent magnetic field perturbations occur at frequencies above $f \sim 10^{-4}$ Hz, whereas below $f \sim 10^{-5}$ Hz the magnetic spectra are primarily due to changes in the background field intensity, resulting in a peak of intensity at approximately one cycle per 27 days. It was also concluded that the main cause of power in the range $f \sim 2\times10^{-5} \rightarrow 2.3\times10^{-3}$ Hz is due to the change in direction of the magnetic field, not magnitude. Coleman tentatively estimated an inertial-range scaling of approximately $f^{-1.2}$.

The next influential work to study the solar wind was conducted by Belcher and Davis [1971], where two key results where found. Firstly, there is a large correlation between the velocity and magnetic field fluctuations, such that Alfvén waves are suspected to be the dominant component of the interplanetary medium, with the

strongest Alfvénic correlation found in fast solar wind. Secondly, it was generally found that no more than 20% of the fluctuation energy is parallel to the background field direction, with a slight anisotropy in the perpendicular plane. Belcher and Davis [1971] found that the magnetic field power spectral density scales as $f^{-\alpha}$ where $1.5 < \alpha < 2.2$ in the time-scale range of approximately 107 minutes to 25 seconds.

Since the first *in-situ* measurements of the solar wind the instrument cadence and accuracy has improved, such that now a full range of temporal scales from the solar rotation period to 1/450 seconds may be recorded using a combination of magnetometers and search-coils (e.g. for the CLUSTER mission see Balogh et al. [1997] and Cornilleau-Wehrlin et al. [1997]). The *in-situ* data has lead to a piece-wise power-law classification of the observed energy spectrum into three distinct ranges [Tu and Marsch, 1995; Bruno and Carbone, 2005]. The low frequency range is characterized by f^{-1} and has been attributed to structures, a remnant of the magnetic carpet or the energy containing/injection scale analogous to hydrodynamic turbulence [Coleman, 1968; Matthaeus and Goldstein, 1982; Tu and Marsch, 1995; Horbury et al., 1996; Goldstein, 2001]. Typically at approximately 1 AU there is a transition between $10^{-4} < f < 10^{-3}$ Hz to a $f^{-\alpha}$ scaling range, where $1 < \alpha < 2$ [Tessein et al., 2009]. This range is known as the "inertial" range and is thought to be where a turbulence cascade begins. There is another transition that occurs approximately at the scales where MHD theory breaks down, such that around the ion-gyro scale a $f^{-\beta}$ scaling range exists, where $2 < \beta < 4$. This range is known as the "kinetic" range. In this thesis we will mainly discuss scales above the ion-gyro scale, this is in part because the validity of Taylor's hypothesis is debatable within the kinetic range, since Kinetic Alfvén Waves (KAW) and Whistler waves are thought to play a significant rule in this area (e.g. see Howes [2009]; Gary and Smith [2009]; Salem et al. [2012] and references within). Unlike the Alfvén wave both the KAW and whistler wave are dispersive, with a dispersion relation that may be crudely approximated as $\omega^2 \sim k_\parallel^2 v_A^2 (1 + k_\perp^2 \rho_i^2)$, where ω is the frequency, $k_{\perp,\parallel}$ are the wavenumber parallel and perpendicular to the background magnetic field, v_A is the Alfvén velocity and ρ_i is the ion gyro-scale [Hasegawa, 1976; Lysak and Lotko, 1996]. One can see that the group/phase velocity may increase as $k_\perp \rho_i$ increases, which corresponds to the kinetic range. Therefore, Taylor's hypothesis may be invalidated for these scales as the group/phase speed may not be much less than the solar wind advection velocity.

The three distinct scaling regions of the power spectral density are displayed in Fig. 1.5. The two panels correspond to observations at different distances from

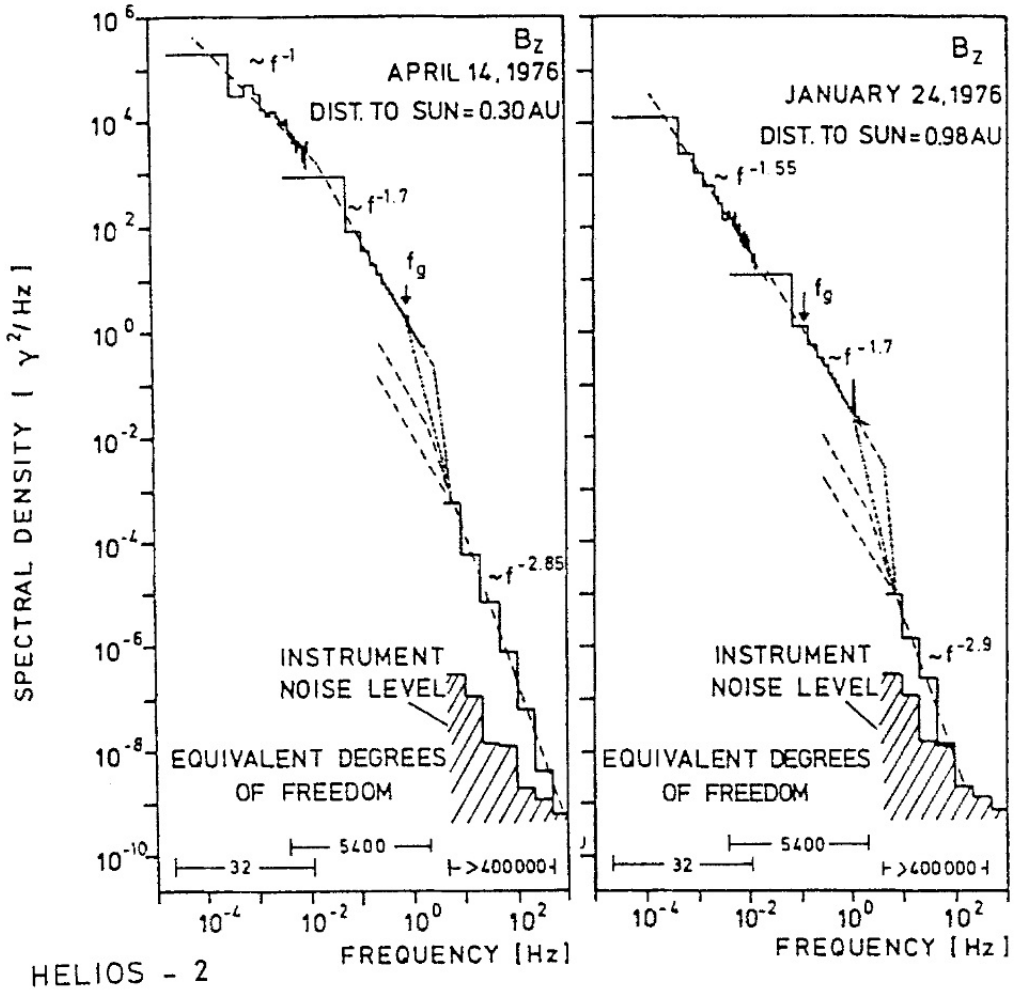

Figure 1.5: Power spectra of B_z at 0.3 and 0.98 AU. Left panel: All three sections of the "classic" spectrum can be seen. Right panel: Uncertainty and variability of the spectral exponent are clear . Figure from Denskat et al. [1983]

the Sun, such that the left and right panel correspond to 0.3 and 0.98 AU respectively. The left panel displays the f^{-1}, inertial and kinetic ranges. The right panel displays two estimates for the inertial range spectral exponent, which highlights the uncertainty within estimating the spectral exponent from observations.

1.6.1 The "Inertial" range

The early measurements of Coleman [1968] suggested that the spectra of magnetic field fluctuations may be due to turbulence and Belcher and Davis [1971] concluded that the main contribution to the solar wind was from correlated velocity and magnetic field perturbation reminiscent of Alfén waves. Thus, there where two interpre-

tations, one of dominant wave or turbulence phenomenology.

Throughout the 1970's the wave description was widely accepted. However, in the 1980's a statistical approach using MHD invariants seemed to be consistent with the predictions of incompressible homogeneous MHD turbulence theory (See [Tu and Marsch, 1995] and references within). Helios observations where used to study the radial evolution of plasma fluctuations, in an attempt to understand whether the turbulence actively evolves during its advection through the interplanetary medium or is the remnant of solar activity. There is a tendency for the outer-scale of f^{-1} to move to lower frequencies as the radial distance increases, as seen in Fig. 1.5. This was interpreted by Tu et al. [1984] as evidence of an active nonlinear cascade within the solar wind. This interpretation is complicated by rapid expansion effects, which may not allow a turbulence cascade to develop *in-situ*, and so the observations shown in Fig. 1.5 may be due to expansion, not a cascade process (See Goldstein and Roberts [1999] and references within). However, if the interpretation of a developing *in-situ* cascade is correct the study by Wicks et al. [2010] imply that the nonlinear cascade of the solar wind is fully developed by approximately 1 AU, as the inertial range length does not increase significantly between 1 to 3 AU.

1.6.2 Structures

The picture of incompressible homogeneous MHD turbulence is not sufficient to explain the observations. There is a need for non-turbulent magnetic structures (e.g. see Tu and Marsch [1995]; Bruno and Carbone [2005]; Borovsky [2008]). However, the introduction of additional magnetic structures may invalidate the condition of homogeneity on some scales [Tu and Marsch, 1995]. This is not surprising when one considers the highly textured source of the solar wind.

The structure of the interplanetary magnetic field is governed by the Parker spiral on the large scale, with bundles of filamentary tubes of various sizes on the medium scale (See [Ness et al., 1966] and references within), to quote Ness et al. [1966]: "*The general picture that emerges from these data is that the interplanetary field is composed of a large number of separate filamentary tubes that originate at the sun*". The filamentary structures known as stream tubes or flux tubes have been studied as well as the waiting-time between discontinuities, which may be hypothesized to correspond to the "walls" between respective filaments (e.g. see Mariani et al. [1973]; Thieme et al. [1990]; Tu and Marsch [1995]; Bruno and Carbone [2005]; Borovsky [2008] and references within).

It has been shown by Matthaeus et al. [1986] that a time-series of the solar wind tends to time-stationary on scales of order $2-10$ hrs. Therefore, the solar wind

may be considered homogeneous with respect to structure at a scale considerably larger than the inertial range of turbulent fluctuations, which typically exist on temporal scales of up to 30 minutes. In addition to filamentary structures there are also Coronal Mass Ejections (CMEs), Co-rotating streams and planetary wakes that affect the local structure of the interplanetary medium.

1.7 Numerical Simulation

For completeness, we briefly consider direct numerical simulations (DNS) of turbulence where the magneto/hydrodynamic equations are evolved in space and time. Therefore, numerical simulations provide a tool for investigating turbulence, where the initial conditions and measurable quantities are known at all points of the domain. Part of the attraction of numerical simulations is the wealth of data that may be produced and analyzed in both space and time, such that Taylor's hypothesis need not be evoked. However, due to the computational cost, numerical simulations are limited to relatively low Reynolds numbers, domain sizes, temporal evolution and simple geometry. Generally, these limitations result in an inertial range that is too short to display power-law scaling. For information on numerical simulations of turbulence see Rogallo and Moin [1984]; Moin and Mahesh [1998]; Knaepen and Moteau [2008]; Biskamp [2003] and references within.

In this thesis we will mainly analyze *in-situ* data from the solar wind. However, there will also be an examination of simulation data generated with the pseudo-spectral method, where the linear terms are progressed in physical space and the nonlinear terms are evolved in Fourier space, for reasons of computational efficiency (e.g. see Canuto et al. [1991, 2007] and references within). Full details of the specific simulations we will use can be found in Müller and Grappin [2005].

Chapter 2

Methodology

Turbulence is a statistically reproducible phenomena, thus methods for quantifying turbulence in the solar wind depend on the statistical properties of the observational time-series. In this chapter we briefly detail the statistical methods used in turbulence studies and this thesis. We begin by explaining the correlation tensor and the power spectral density, which are important in determining the energy per unit scale or frequency respectively. The power spectral density is commonly calculated via two methods, that of the Fourier and the wavelet transform. The similarities of these two methods will be covered. Then we will describe the methods used to quantify the probability distribution and intermittency of fluctuations. Finally, we explain anisotropy analysis. Due to the magnetic field that imposes ordering upon the plasma there are two different types of anisotropy. That of the fluctuations with respect to the background magnetic field, known as variance anisotropy, and that of wave vector anisotropy, which may be estimated via Taylor's hypothesis by the angle between the sampling direction and the background magnetic field.

2.1 Fluctuations

The term "fluctuation" is used frequently to refer to deviations from the equilibrium/mean of a field. Throughout this thesis there are two distinct uses of the term fluctuation, $\Delta\mathbf{S}(t)$ and $\delta\mathbf{S}(t,\tau)$, which are related. Let $\mathbf{S}(t)$ be the time-series of a field. One may calculate a fluctuation that is centered on time, t, as $\delta\mathbf{S}(t,\tau) = \mathbf{S}(t) - \mathbf{S}(t+\tau)$. Therefore, the fluctuation $\delta\mathbf{S}(t,\tau)$ is centered at time, t, and dependent on the temporal-scale, τ, and so localized in frequency.

To define $\Delta\mathbf{S}(t)$ let the time-series $\mathbf{S}(t)$ be written as, $\mathbf{S}(t) = \mathbf{S}_0(t) + \Delta\mathbf{S}(t)$, where $\mathbf{S}_0(t)$ is the mean value defined over some temporal-scale much greater than

the fluctuating scales of interest and $\Delta\mathbf{S}(t)$ is the deviation from $\mathbf{S}_0(t)$ at time, t, such that

$$\Delta\mathbf{S}(t) = \sum_{\tau} \delta\mathbf{S}(t,\tau). \tag{2.1}$$

Note that $\Delta\mathbf{S}(t)$ contains all frequencies less than $\mathbf{S}_0(t)$. Whereas, $\delta\mathbf{S}(t,\tau)$ is a bandpass filter, and so contains a narrow range of frequencies.

In analytical/theoretical treatments of turbulence it is assumed that the fluctuations are that described by $\Delta\mathbf{S}(t)$. Therefore, if we relate this notation to that in the previous Chapter the fluctuations of the magnetic field, $\mathbf{b}$, and velocity, $\mathbf{v}$, may be seen to be $\Delta\mathbf{S}(t)$, whilst the bulk flow, $\mathbf{V}_0$, and background magnetic field, $\mathbf{B}_0$, are $\mathbf{S}_0(t)$. We use $\Delta\mathbf{S}(t)$ and $\delta\mathbf{S}(t,\tau)$ when discussing observations and lower case symbol (e.g. v, b) when discussing theory.

2.2 Correlation Tensor

The correlation between fluctuation components is central to the study of turbulence, especially in determining the transfer of energy and the dissipation rate [Batchelor, 1953; Lesieur, 1997]. The correlations may not be determined directly from the Navier-Stokes equation due to the closure problem (e.g. see Lesieur [1997]). Empirically the simplest non-trivial correlation is the second-order correlation tensor. The most general form of the second-order correlation tensor is the two-point two-time correlation tensor, which for the velocity may be defined as

$$R^v_{ij}(\mathbf{r},t) = \langle v_i(\mathbf{x},t) v_j(\mathbf{x}+\mathbf{r},t+\tau)\rangle \tag{2.2}$$

where $R_{ij}(\mathbf{r},t)$ is the correlation tensor, $\langle ...\rangle$ denotes a time averaged ensemble, $\mathbf{r}$ is a spatial scale of separation, τ is a temporal scale of separation, v is the fluctuating velocity about a background value as defined in Section 1.4.

We consider the case where the measurements are made at a fixed-point in space, such that the correlation tensor is only a function of time. One must consequently evoke Taylor's hypothesis, such that we may estimate the spatial correlation by the substitution $\mathbf{r} = V\tau\hat{\mathbf{e}}_r$. The turbulence is assumed to be statistically homogeneous, such that the correlation tensor is an even positive function of $\mathbf{r}$. Thus, the estimated two-point one-time correlation tensor may be expressed in terms of a time-lag, τ, as

$$R^v_{ij}(V\tau\hat{\mathbf{e}}_V) = \langle v_i(\mathbf{x}) v_j(\mathbf{x}+\tau V\hat{\mathbf{e}}_V)\rangle \tag{2.3}$$

The two-point one-time correlation tensor of R_{ij} is a 3×3 tensor that is

necessary and sufficient to determine the energy per unit mass associated between arbitrary components of a fluctuating field, such as the velocity, magnetic field or Elsässer variables [Batchelor, 1953; Lesieur, 1997]. By using the Wiener-Krintchine theorem one may Fourier transform the elements of the correlation tensor to power spectral density elements, such that $P_{ij}(f) = \frac{1}{2\pi}\int R_{ij}(\tau')\exp(-i2\pi f\tau')d\tau'$, where P_{ij} is the power spectral density tensor and frequency corresponds to $f = 1/\tau$. The study of anisotropy between various elements of the power spectral density tensor is termed "variance anisotropy" and is discussed in Section 2.5.1, whilst a study of the summed diagonal elements of the power spectral density tensor is termed "power anisotropy" and is discussed in section 2.5.2. One may note that an explicit collection of fluctuations and time-averaging is not necessary, as the correlation between two stationary processes may be written as a convolution, such that $R_{ij}(\tau) = v_i(t) * v_j^{\star}(t)$, where $\star$ is the complex conjugate and $*$ is the convolution operator. The correlation is sometimes normalized, such that $-1 \leq R_{ij} \leq 1$. This is achieved by dividing the correlation by the standard deviation of both signals, such that $R_{ij}^{NORM}(\tau) = (v_i(t) * v_j^{\star}(t))/(\sigma_i\sigma_j)$, where $\sigma_{i,j} = \langle |v_{i,j}|^2 \rangle$ (e.g. see Davidson [2004] and references within).

2.3 Power Spectral Density (PSD)

As mentioned in the previous section, the PSD is the Fourier transform of the two-point correlation, and so is important in describing the relation of second-order nonlinear interactions. The PSD is a measure of the energy per unit frequency contained within a time-series or signal, $u(t)$, that is usually assumed to be produced by a slowly varying or stationary process. The PSD is an even positive function. If one has Fourier or Wavelet coefficients, denoted as $\tilde{u}(f)$. Then the PSD is

$$P(f) \sim |\tilde{u}(f)|^2 \tag{2.4}$$

such that, $|\tilde{u}(f)|^2 = \tilde{u}(f)\tilde{u}^{\star}(f)$, where $\tilde{u}^{\star}(f)$ is the complex conjugate of $\tilde{u}(f)$. A key consequence of using $|\tilde{u}(f)|^2$, is that the original phase information may not be reconstructed from the PSD. Two common methods for constructing the PSD are via Fourier transform or wavelet transform [Paschmann and Daly, 1998]. Therefore we will present both the Fourier and wavelet transform to highlight the similarity of both approaches.

2.3.1 Fourier Coefficients

Under the condition that a time-series, $u(t)$, has a finite number of discontinuities and that $\int_{-\infty}^{+\infty} u(t)dt$ exists it is possible to conduct a Fourier transform. The kernel of the Fourier transform is, $g(t) = \cos(2\pi f_n t) - i\sin(2\pi f_n t)$, which may be expressed as $g(t) = \exp(-i2\pi f_n t)$. A finite and piece-wise signal may be written as,

$$u(t) = \sum_{n=-\infty}^{\infty} \tilde{u}[n] \exp\left(-2\pi i f_n t\right), \tag{2.5}$$

where $f_n = n/T$ is the periodic oscillation frequency, T is the temporal length of the signal and $\tilde{u}[n]$ is the Fourier coefficient for the n-th frequency.

One may write the complex Fourier coefficients as,

$$\tilde{u}(f_n) = \frac{1}{T} \int_{t_0}^{t_0+T} u(t) \exp\left(\frac{2\pi i n t}{T}\right) dt, \tag{2.6}$$

where t_0 is the beginning of the temporal window [Paschmann and Daly, 1998].

For a discretely sampled signal of N points the periodic frequencies are $f_n = n/T$. The uncertainty in frequency may be written as $\Delta f = f_s/N$, where f_s is the sampling frequency. Thus, as the sampling frequency tends to zero the discrete and continuous Fourier transform coincide, such that the uncertainty in frequency is proportional to the temporal length of the signal, T. Spectral leakage may occur when the discretely sampled signal is not periodic [Paschmann and Daly, 1998].. Spectral leakage is a term used to define power measured away from the central-frequency of the kernel, $g(t)$.

A window-function that reduces spectral-leakage has the general characteristics of a temporal function that is a minimum at windows edges and maximum at the center. The spectral-leakage of four different window functions from top-left to bottom-right using a rectangular, triangular, Hanning and Gaussian window for a test signal composed a cosine with a frequency of $f = f_s/4$, where f_s is the sampling frequency, and a window width of 128 points for all window functions is displayed in Fig. 2.1. A technique commonly used for estimating the PSD that makes use of overlapping subintervals and a window-function to reduce uncertainty is the Welch spectral method [Paschmann and Daly, 1998].

2.3.2 Wavelet Coefficients

A wavelet is a transformation kernel that makes the desired compromise between temporal and frequency resolution, where the uncertainty principle of $\Delta f \Delta t \geq 1$

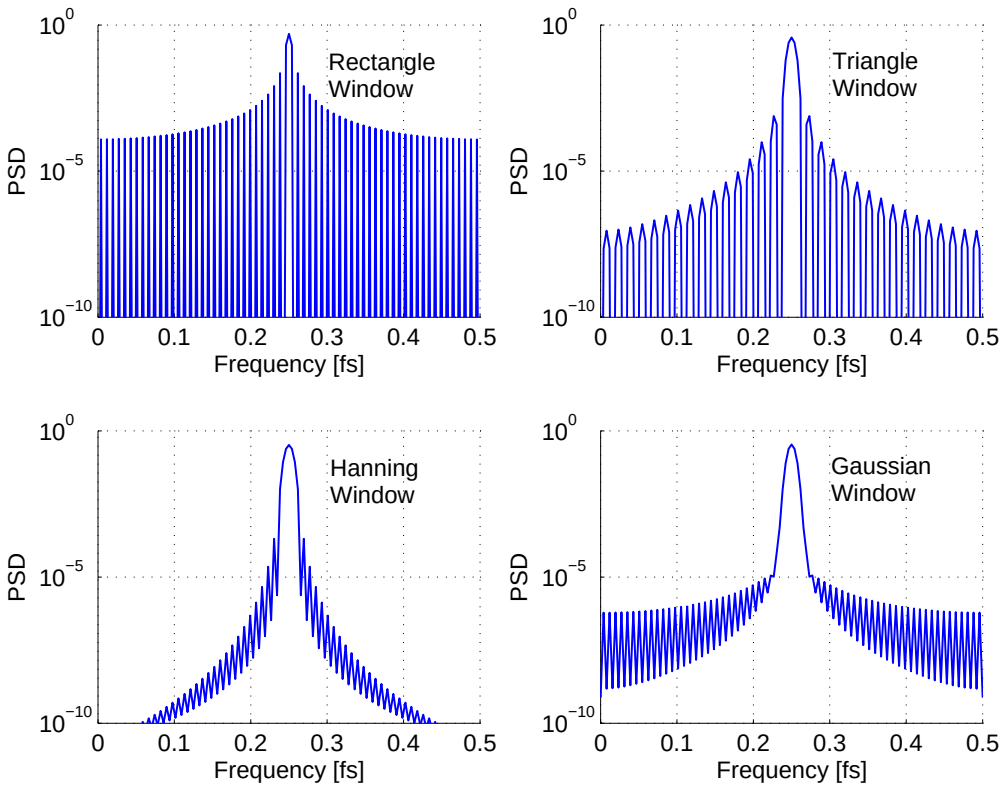

Figure 2.1: Spectral leakage for four different window functions for a test signal that contains a sinusoidal function centered at $f = f_s/4$. The window function is 128 points in length for all windows. The total area in all plots is normalized to unity.

applies. A Gaussian wave packet is the only form that allows optimization in both frequency and time, as it's the only form for which $\Delta f \Delta t = 1$ [Landau and Lifshitz, 1977]. Due to the time locality property, wavelets are better suited than conventional Fourier methods to study time variable signals and anisotropy of the solar wind due to the high variability of the background magnetic field direction. We shall mainly use the wavelet method throughout the thesis, as the background magnetic field of the solar wind varies over a large range of scales, such that *a priori* selection of window size using the Fourier Welch method is untenable.

Generally a wavelet may be described by a translation and scale parameter, such that

$$\psi_{a,t'}(t) = \frac{1}{\sqrt{a}}\psi\left(\frac{t-t'}{a}\right), \tag{2.7}$$

where a is positive and defines the scale and t' is a real number that defines the temporal shift. Let us consider the Morlet wavelet, where the mother wavelet may be described as

$$M(t) = \exp\left(-t^2/2\right)\exp\left(-i\omega_0 t\right), \tag{2.8}$$

where ω_0 is a free parameter to be chosen that defines the number of oscillations that are contained within the Gaussian wave-packet. Convention places the number of oscillations within a Gaussian wave-packet as $5 \leq \omega_0 \leq 2\pi$ [Paschmann and Daly, 1998]. The daughter wavelets are the family of wavelets that may be created by re-scaling the mother wavelet, and so may be used to measure lower frequencies in a time-series or signal. The scale parameter may be written in terms of frequency as, $f = 1/a$. Therefore the daughter wavelet of the Morlet may be written as

$$M_{f,t'}(t) = \sqrt{f}\exp\left(-2\pi i f(t-t')\right)\cdot\exp\left(\frac{-f^2(t-t')^2}{2}\right). \tag{2.9}$$

We may now compare the wavelet transform to that of the Fourier transform. The Fourier transform of equation 2.6 may be written as, $\tilde{u}(f_n) = \int u(t)g(t)dt$. We replace the Fourier transform kernel of $g(t) = \exp(-i2\pi f_n t)$ with the wavelet kernel of $M_{f,t'}(t)$, such that

$$\tilde{u}(f_n, t') = \sqrt{f}\int_{-\infty}^{+\infty}\exp\left(\frac{-f^2(t-t')^2}{2}\right)u(t)\exp\left(-2\pi i f(t-t')\right)dt. \tag{2.10}$$

It is possible to see that the wavelet coefficients are equivalent to the Fourier coefficients localized in time with a window-function to reduce spectral leakage in a similar way the Welch method [Paschmann and Daly, 1998].

We present a schematic to demonstrate how the temporal-frequency domain

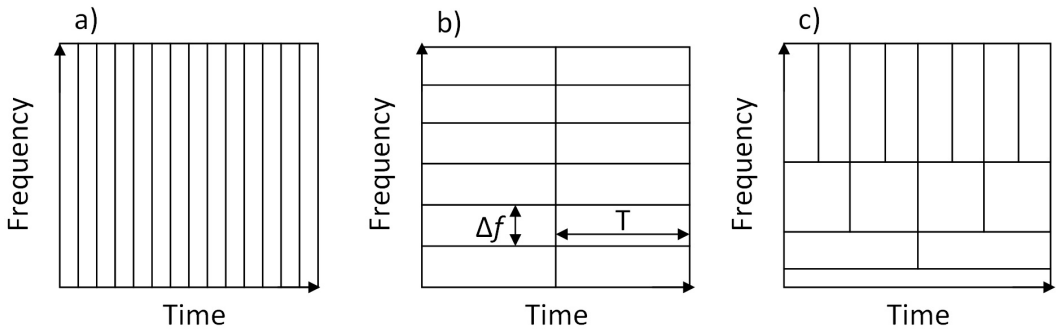

Figure 2.2: An example of temporal, Fourier and wavelet coverage of the temporal-frequency domain is shown in panel a, b and c respectively. The temporal window of the time-series is T and the frequency band is Δf. Each box in the temporal-frequency domain ($T\Delta f$) have equal area.

is tiled by the Fourier and wavelet transform in Fig. 2.2. The temporal, Fourier and wavelet coverage of the temporal-frequency domain is shown in panel a, b and c respectively. In all panels the total area of each box ($T\Delta f$) is the same, however how the domain is covered is different. One can see that for the Fourier representation the domain is covered in identical boxes, therefore $T \to \infty$ where $\Delta f \to 0$. However, in the wavelet method the temporal scale is increased as the frequency decreases, thus $\Delta f \sim f$.

Using the assumption that the signal or time-series is time-stationary one creates a PSD estimate by selecting wavelet coefficients that overlap by no more than 50% and conduct a time-average, such that $\langle|\tilde{u}(f,\tau)|^2\rangle_\tau = |\tilde{u}(f)|^2$. Normalization for the wavelet PSD is, $P(f) = 2\Delta t|\tilde{u}(f)|^2$, where Δt is the sampling cadence. The wavelet method of constructing a PSD via ensemble average allows increasingly accurate estimates as the ensemble tends to infinity. Due to the uncertainty principle, as the frequency decreases the ensemble size for a given finite data interval decreases. Thus, the higher frequencies are more accurately estimated than the lower frequencies for a given interval.

2.4 Probability Distributions

2.4.1 Generalized Structure Functions (GSF)

The generalized structure function (GSF) is a method for quantifying the scaling of moments of a probability distribution function (PDF). Let $\delta(\mathbf{r})$ be the fluctuation of some turbulent quantity over a spatial separation of $\mathbf{r}$, e.g. $\delta(\mathbf{r}) = f(\mathbf{x}) - f(\mathbf{x}+\mathbf{r})$, where f may be velocity, magnetic field or Elsässer variable. In many turbulence

studies it is not possible to have a full array of probes that are capable of calculating the spatial fluctuations. Therefore, Taylor hypothesis is evoked, such that the fluctuations are defined from a time-series recorded at a singe spatial point as a function of time-lag as, $\delta(\tau)$ [Frisch, 1995]

The moments of the temporal ensemble of fluctuations may be defined as $\langle \delta^m(\tau) \rangle_t$, where $\langle ... \rangle_t$ denotes a temporal average and m is the moment of the probability ensemble to be determined. In the context of turbulence the second and third-order moments are of great interest as they constitute direct measurements of the energy density and dissipation rate respectively [Frisch, 1995]. According to Kolmogorov's four-fifths law the dissipation rate is exactly related to the third-order of the parallel structure function with respect to the flow velocity, such that $\langle (\delta v_{\parallel}(\mathbf{r}, \mathbf{l}))^3 \rangle = -\frac{4}{5}\epsilon l$ [Kolmogorov, 1991]. Thus, an exact measurement of the third-order structure function is fundamental in determining whether turbulence is present and the dissipation rate. However, odd moments have a large degree of uncertainty due to extreme values and finite-ensemble size. Therefore, the GSF is defined as $\langle |\delta(\tau)|^m \rangle_t$. Thus, for a self-similar/fractal process $S_m(\tau) = \langle |\delta(\tau)|^m \rangle_t \sim \tau^{\zeta(m)}$, for all m [Frisch, 1995]. Note it is not possible to exactly determine the dissipation rate of the third-order moment with the GSF formalism.

To find $\zeta(m)$ one measures the gradient of $\log_{10}(S_m)$ against $\log_{10}(\tau)$. Thus, a plot of $\zeta(m)$ against m displays the form of $\zeta(m)$. A linear fit, $\zeta = hm$, characterizes a self-similar/fractal process, where the gradient is the value of h known as the Hurst exponent. Ideally, the accurate determination of $\zeta(m)$ over a large range of m is desired to create a good estimate of h or determine whether the process is indeed fractal, as opposed to another model, such as bi-fractal [Frisch, 1995]. However, there are strong data limitations on the maximum degree of moments that may be calculated, such that rarely is it possible to accurately investigate $m \geq 6$ (e.g. see Dudok de Wit and Krasnosel'skikh [1996]; Horbury and Balogh [1997] and references within).

A recent publication [Guadagnini et al., 2012] has shown that calculating $\zeta(m)$ may not be sufficient to determine whether a process is multi-fractal, however a fractal detection does confirm a fractal process. The issue is that a self-similar process that exists only over a finite range of scales may display spurious multi-fractal scaling. It may also be shown that where a finite scaling range does not alter the fractal nature of a time-series it may introduce a systematic uncertainty in the estimate of H (e.g. see Kiyani et al. [2006, 2009] and references within). We show the PSD for a Brownian ($H = 0.5$) time-series of 10^6 data points that has been calculated via the Welch method in the top panels of Fig. 2.3. The top-left panel

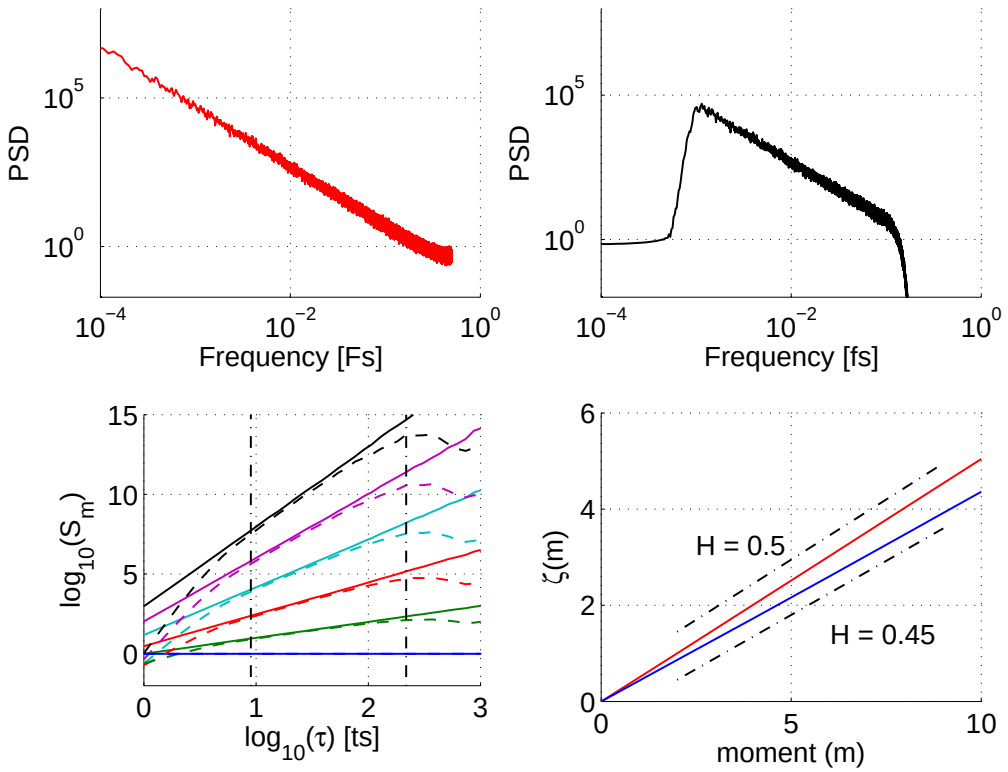

Figure 2.3: Uncertainty in estimating the Hurst exponent, H, with a fractal time-series that has been filtered to have a finite scaling range. Top panels: display the same Brownian time-series PSD, where the left panel comes from the raw time-series with scaling on all scales of the time-series and the right panel comes from a filtering the time-series in Fourier space, such that there is a scaling range of approximately two decades. Bottom-left panel: Structure function for $m = [0, 2, 4, 6, 8, 10]$ in dark blue, green, red, light blue, magenta and black respectively. Solid and dashed lines correspond to the raw and filtered time-series respectively. Bottom-right: $\zeta(m)$ for the raw and filtered case, measured between the vertical dot-dashed black lines in the bottom-left panel, are shown in red and blue respectively. The correct scaling is $H = 0.5$ for these time-series, where H is to be determined from the gradient of the solid lines in the bottom-right panel.

shows the PSD where scaling is present for all scales within the time-series, the top-right panel shows the PSD for the same data filtered in Fourier space to contain only a limited scaling range of two decades, which is a similar length of scaling range observed in the inertial range of the solar wind. The bottom-left panel shows the structure function, S_m, for the moments $m = [0, 2, 4, 6, 8, 10]$ in dark blue, green, red, light blue, magenta and black respectively. The solid lines and the dashed lines display the full scaling case and finite scaling case respectively. The bottom-right panel displays $\zeta(m)$ in red and blue for the full scaling case and finite scaling case respectively. It can be seen a systematic uncertainty of ± 0.05 may be expected from a finite scaling range of similar length to the solar wind inertial range when using an interval of 10^6 data points.

2.4.2 Intermittency

In the context of turbulence it is important to determine the probability and joint probability distribution of fluctuations. The probability and joint probability function must be known in order to close the linearized Navier-Stokes equation. A mathematically convenient "dummy" PDF is the Gaussian PDF. However, a Gaussian PDF is not sufficient to describe a turbulent field, such as the velocity and magnetic field fluctuations, as all the odd moments are equal to zero, and so there would be no energy cascade, which is described by the third-moment. An example of a closure which is based on the Gaussian distribution but does not prohibit an energy cascade is the Eddy Damped Quasi-Normal Markovian (EDQNM) assumption, where it is assumed that the fourth-moment of the PDF may be described by a product of second-order moments, such that for the velocity fluctuations $\langle vvvv \rangle = \langle vv \rangle \langle vv \rangle$. The EDQNM formalization is a self-similar/fractal phenomenology [Lesieur, 1997].

In three-dimensional hydrodynamic turbulence vortex tubes are created and stretched. As the vortex tubes are stretched the cross-sectional area is decreased and the mean vorticity increases across a cross-section of the tube. These thin structures are limited to a few Kolmogorov dissipation scales in width and are extended to a length of order the integration scale. The increased gradients associated with these structures are the source of increased dissipation of kinetic energy and are surrounded by comparatively low dissipation flow (Lesieur [1997]). Therefore, there are localized areas of strong dissipation, which leads to a phenomenology known as intermittency or internal intermittency.

In the original K41 and IK formalism the energy dissipation rate, ϵ, is a constant. However, due to the filamentary structure the original ϵ is replaced by $\tilde{\epsilon}_l = \langle \epsilon \rangle = 1/V_l \int_{V_l} \epsilon(x) dx$, such that there is a spatial average dissipation rate with local

fluctuations of the dissipation rate. The spatial-temporal fluctuations of dissipation rate lead to $\tilde{\epsilon}_l/\epsilon \sim (l/l_0)^{\alpha(l)}$, where l is the spatial-scale under investigation, l_0 is the integral scales and $\alpha(l)$ is some scaling function. This phenomenology is called intermittency. The topology of such a phenomenology is not obvious, however direct numerical simulations of three-dimensional isotropic turbulence shows that the thin tubes of high vorticity are unequally distributed throughout space (See Lesieur [1997] and references within), i.e. the dissipation is not a fractal/self-similar distribution in space. Thus, pdfs of the velocity increments have fat tails that scale as $\exp(-|x|)$, instead of the Gaussian expectation of $\exp(-x^2)$ [Lesieur, 1997]. Multi-fractal scaling has also been shown observationally to exist in the solar wind and in MHD simulations (e.g. see Burlaga [1991]; Tu and Marsch [1995]; Bruno and Carbone [2005]; Martin et al. [2012]; Plunian et al. [2013]; Wan et al. [2012] and references within).

It is hypothesized that current-sheets are responsible for the observed intermittency for MHD turbulence in an analogous way to vortex tubes in hydrodynamic turbulence. For MHD turbulence the scaling relation of the Elsässer fields, such that $\mathbf{z}^{\pm} = \mathbf{v} \pm \mathbf{b}$, are the key quantity of interest, specifically as the dissipation may be estimated by as, $\epsilon^{\mp} = \langle \mathbf{z}^{\pm} | \mathbf{z}^{\mp} |^2 \rangle$. However, the scaling of the velocity and magnetic field fluctuations has attracted attention separately. The goal of intermittency studies is to predict the observed non-self-similar nature by phenomenological models. For example the Kolmogorov-Oboukhov-Yaglom model of "self-similar breakdown of turbulent eddies" (also know as the log-normal model), Novikov-Stewart model equivalent to the β model where an inertial range eddy only contains turbulence in a fraction, β, of its volume, p-model and She-Leveque model (See [She and Leveque, 1994; Politano and Pouquet, 1995; Frisch, 1995; Lesieur, 1997; Biskamp, 2003] and references within).

The standard way that intermittency is quantified is to measure the scaling relation of fluctuation distribution. The moments are defined as, $S_i^m = \langle |\delta B_i(t,\tau)|^m \rangle_t \sim \tau^{\zeta(m)}$, where i is the component, m is the moment and $\langle ... \rangle$ indicates an ensemble average over t. Self-similar scaling as assumed in Kolmogorov (1941) and IK theory may been seen if and only if $\zeta(m) = hm$, such that there is a linear relation in with respect to ζ that passes through the origin.

2.5 Anisotropy

The background magnetic field direction and magnitude is an important quantity that governs the temporal evolution of the Elsässer variables, as highlighted in

equation 1.13. This is contrary to the Navier-Stokes equation, where the background flow may be removed by a transform. Therefore, in studies of MHD turbulence there is a natural coordinate system in which to study the fluctuations.

Due to the important role of the background magnetic field on the dynamics of the system it is crucial to determine what the physically relevant background magnetic field is. This is a controversial topic within the MHD turbulence community, and will be covered in detail in Chapter 4 of the thesis. It is sufficient at this stage to assume one may produce a reliable estimate of the background magnetic field from *in-situ* observation. Studies of anisotropy with respect to the background magnetic field may be broken into two definitions, that of "Variance" and of "Trace" anisotropy.

2.5.1 Variance Anisotropy

Variance anisotropy is the study of the components of fluctuations with respect to the background magnetic field. If we define the background magnetic field as, $\mathbf{B}_0 = B_0\hat{\mathbf{e}}_z$, it is possible to decompose the fluctuations, $\delta\mathbf{B}$, into parallel fluctuations, $\delta B_\parallel = \delta\mathbf{B}\cdot\hat{\mathbf{e}}_z$, and perpendicular fluctuations, $\delta B_\perp = \delta\mathbf{B}\times\hat{\mathbf{e}}_z$. It is possible to use the solar wind flow velocity, which is equivalent to the *in-situ* sampling direction, to decompose the perpendicular direction, such that $\hat{\mathbf{e}}_x = \hat{\mathbf{e}}_z \times \hat{\mathbf{e}}_v$, where $\hat{\mathbf{e}}_v$ is the unit vector of the solar wind flow, and $\hat{\mathbf{e}}_y = \hat{\mathbf{e}}_z \times \hat{\mathbf{e}}_x$ completes the orthogonal set. One can then perform the standard statistical tests of intermittency, correlation, PSD ,etc on the distributions of $\delta B_\parallel$, $\delta B_{\perp,x}$ and $\delta B_{\perp,y}$. The decomposition of a fluctuation into this coordinate system may be seen in Fig. 2.4, where ϕ is the angle from the $\hat{\mathbf{e}}_x$ unit vector and θ is the angle between the solar wind velocity and the background magnetic field.

The seminal study of variance anisotropy was conducted by Belcher and Davis [1971]. They found that the average power anisotropy in the solar wind is 5:4:1 in the coordinate system of $\mathbf{e}_x, \mathbf{e}_y, \mathbf{e}_z$. Throughout the inertial range other authors, such as Belcher and Solodyna [1975]; Chang and Nishida [1973]; Burlaga and Turner [1976]; Marsch and Tu [1990]; Klein et al. [1991], found similar results.

A method closely related to variance anisotropy is that of minimum variance. Sonnerup and Cahill [1967] introduced minimum variance analysis to determine the normal vector to discontinuities in the magnetosphere. For the minimum variance method one determines the matrix, $S_{ij} = \langle B_i B_j\rangle - \langle B_i\rangle\langle B_j\rangle$, where i and j are components of the magnetic field. This matrix is then diagonalized to find the three eigenvectors that correspond to minimum, medium and maximal variance, denoted as $\mathbf{e}_1, \mathbf{e}_2, \mathbf{e}_3$ with eigenvalues $\lambda_1, \lambda_2, \lambda_3$. It was shown by Sonnerup and Cahill [1967]

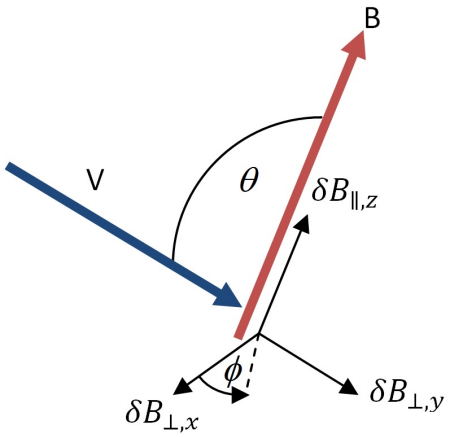

Figure 2.4: The local coordinate system. The background magnetic field, B, is red and the solar wind velocity, V, is blue. The angle from the background magnetic field is θ and the angle from $\hat{\mathbf{e}}_{\perp,x}$ is ϕ. Three orthogonal fluctuations in the direction of the local coordinate unit vectors are shown as $\delta B_{\parallel,z}$, $\delta B_{\perp,x}$ and $\delta B_{\perp,y}$.

that the direction of $\mathbf{e}_1$ corresponds to the normal of a discontinuity and in the solar wind $\mathbf{e}_1$ shows good agreement with the direction of the background magnetic field. In the solar wind it is usually found that $\lambda_3 > \lambda_2 \gg \lambda_1$, which demonstrates anisotropy in correlation length parallel and perpendicular the background magnetic field. Minimum variance has also been used as a scale-dependent process in the kinetic scales [Perri et al., 2009]. The variance anisotropy will be investigated in detail in Chapter 3.

2.5.2 Trace Anisotropy

The trace of the magnetic field or velocity fluctuations represents the energy density [Batchelor, 1953] and is defined as $P^T = \Sigma_i P_{ii}$, where P_{ii} are the diagonal components of the PSD tensor. This has been used extensively in an attempt to measure the reduced one-dimensional energy spectra of the solar wind for $k_\perp$ and $k_\parallel$, where perpendicular and parallel are taken with respect to the background magnetic field direction (e.g. see Horbury et al. [2008]; Podesta [2009]; Tessein et al. [2009]; Wicks et al. [2010]; Forman et al. [2011]; Li et al. [2011] and references within).

Sampling the solar wind at-a-point with a satellite evoking Taylor's hypothesis does not allow one to isolate a unique $\mathbf{k}$. Instead a reduced one-dimensional spectral density, $\tilde{P}_{ij}(f, \theta)$, may be determined. Evoking Taylor's hypothesis results in measuring the spectral density, $P_{ij}(\mathbf{k})$, integrated over the plane defined by $\mathbf{k} \cdot \mathbf{V}_{sw} = 2\pi f$ in $\mathbf{k}$ space, where $\mathbf{V}_{sw}$ is the solar wind velocity. Therefore,

the observed reduced one-dimensional spectral density is defined as $\tilde{P}_{ij}(f,\theta) = \int d^3k P_{ij}(\mathbf{k})\delta(2\pi f - \mathbf{k}\cdot\mathbf{V}_{sw})$, where θ is the angle between the background magnetic field and solar wind flow velocity. For clarity we expand the delta function to, $\delta(2\pi f/V_{SW} - k_\perp \sin\theta - k_\parallel \cos\theta)$. Thus, if one collects data where $\theta = 0$ or $\theta = \pi/2$ the results are dependent only on $k_\parallel$ of $k_\perp$, regardless of any assumptions about the ratio of $k_\parallel$:$k_\perp$.

The trace anisotropy has two aspects of interest; the spectral exponents and the relative power of $P_\perp^T$ and $P_\parallel^T$ (e.g. see Chen et al. [2010] and references within). The interest is due to the predictions of theories, especially that of Goldreich and Sridhar [1995] where the spectral exponents and power at a specific scale are anisotropic. The trace anisotropy has been found to depend strongly on the method used to calculate the background magnetic field, with regard to spectral anisotropy (e.g. see Tessein et al. [2009]; Wicks et al. [2010] and references within). However, the power is always found to anisotropic. The topic of trace anisotropy and the importance of accurately calculating the background magnetic field will be considered in detail in Chapter 4.

Chapter 3

Nonaxisymmetric Observations Test Turbulence Theories

3.1 Nonaxisymmetric Variance Anisotropy

The presence of a background magnetic field, $\mathbf{B}_0$, introduces a preferred coordinate system. The preferred coordinate system can be seen by the presence the term $(\mathbf{B}_0 \cdot \nabla)\mathbf{z}^{\pm}$ in equation 1.13. Therefore, an anisotropy between the perpendicular and parallel direction with respect to the background magnetic field may be expected. Belcher and Davis [1971] were the first to observe that the variance power is nonaxisymmetric, that is, the variance power is not homogeneous within the perpendicular plane with respect to the background magnetic field. Such nonaxisymmetry is unexpected, as it implies there is another natural coordinate system, in addition to that set by the background magnetic field direction, that influences the dynamics of the turbulence.

In this chapter we use *in-situ* data from three satellites to investigate the nonaxisymmetric power distribution within the perpendicular plane with respect to the background magnetic field. It is found that the preferred direction within the perpendicular plane is the macroscopic velocity of the solar wind, and so the direction of sampling. We model the turbulent dynamics under the hypothesis of axisymmetry and find that *in-situ* sampling at-a-point is responsible for the observed nonaxisymmetry. We demonstrate that the observed nonaxisymmetry may be used as a tool to discriminate between models of turbulence.

3.2 Data Sets

In this section we will analyze two intervals [January 20, 2007, 1200-1315 UT and January 30, 2007, 0000-0100 UT] of fast quiet solar wind observed by CLUSTER spacecraft 4 whilst the magnetic field instruments FGM (cadence of 67 Hz) and STAFF-SC (cadence of 450 Hz) where both instruments are operating in burst mode, providing high-resolution data capable of observing both the inertial and kinetic scales simultaneously. To create a single time-series from the two instruments we use a similar procedure as Chen et al. [2010]; Alexandrova et al. [2004]. First the two time-series are placed on the same sample basis by linearly interpolating the FGM signal to the same times as the STAFF-SC time-series. A discrete wavelet transform is applied to all three geometric components for both instrument time-series. A times-series that contains only frequencies approximately greater than 0.9 Hz is generated from the STAFF-SC data, whilst a time-series containing only frequencies approximately less than 0.9 Hz is created from the FGM data. The two time-series are then added together to create a single time-series that contains the lowest frequency from the FGM data and highest frequency from the STAFF-SC data.

The raw x component from FGM and STAFF-SC are shown in blue and red respectively for the January 30th interval in panel (a) of Fig. 3.1. One can see that the two signals are in approximate agreement at 1 Hz, however the FGM signal above and the STAFF-SC signal below 1 Hz are contaminated with noise, hence the selected merging frequency of the two data sets. Panel (b) shows the FGM signal after linear interpolation and the wavelet transform in blue and the STAFF-SC signal after the wavelet transform in red. Panel (c) shows the resulting PSD when the two signals have been merged. Panel (d) displays the estimated noise to signal percentage (NSP) by comparing the PSD obtained in the lobes of the magnetosphere [30 June, 2007, 15:00-15:20 UT] and the PSD obtained for the solar wind intervals. It is assumed that the lobes of the magnetosphere signal are dominated by instrument noise, and so provide a good proxy for the actually noise floor of the instruments. The x and z components of the magnetic field are displayed in black and red respectively. It can be seen that in the recorded reference frame of the measurements the z component is cleaner than the x component. This is due to the spin of the satellite, which is orientated in the x-y plane. One can see a clear peak at approximately 0.25 Hz in the x component, which corresponds exactly to the spin-tone of the satellite.

In addition to the CLUSTER data we also consider magnetometer data from

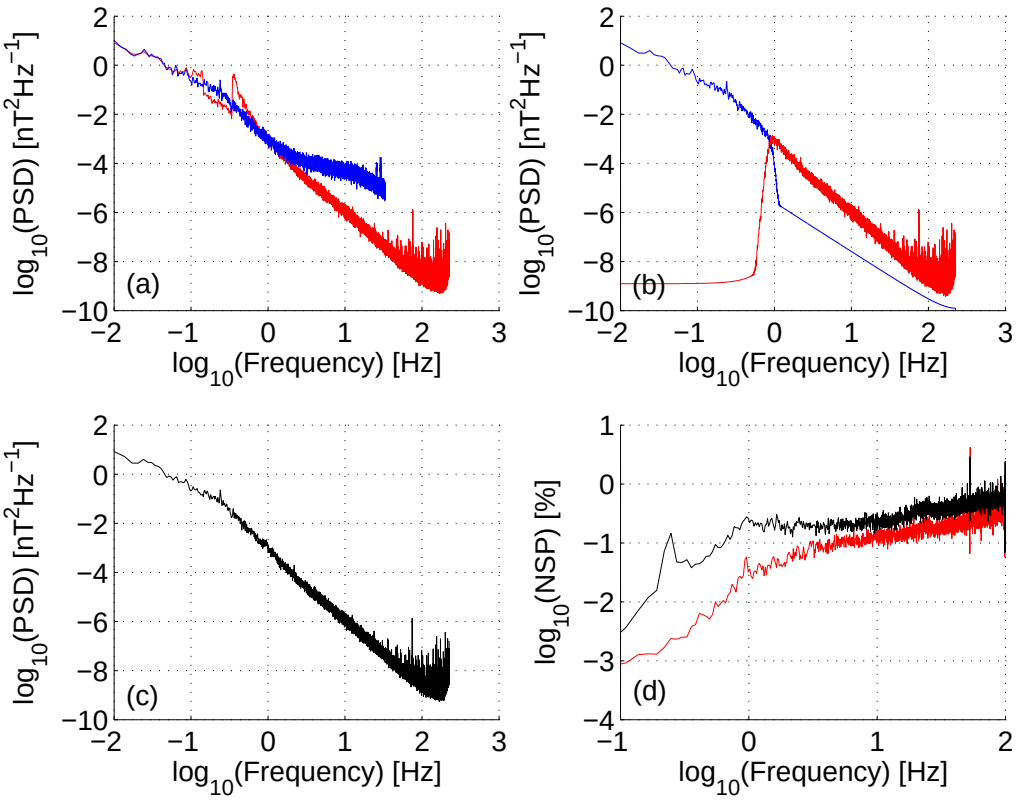

Figure 3.1: Panel a) PSD of the x component for the FGM and STAFF-SC instruments in blue and red respectively. Panel b) The interpolated and filtered PSD of the x component for the FGM and STAFF-SC instruments in blue and red respectively. Panel c) The combined PSD for the x component for the FGM and STAFF-SC instruments. Panel d) The estimated noise to signal percentage as a function of frequency for the x and z component in black and red respectively.

STEREO-A [February 15-17, 2008] and Ulysses [day 91 - 146, 1995] in fast solar wind. The STEREO-A interval is recorded at a cadence of 8 Hz. However, the noise-floor for the magnetometer is realized at approximately 1 Hz, such that only the inertial range scales are accessible. The STEREO-A satellite does not spin and so provides analysis of an interval that is not affected by satellite spin.

The Ulysses interval is recorded at a cadence of 1 Hz. In this interval Ulysses moved from a heliographic latitude of 21° to 58° and a radial distance of 1.36 to 1.58 AU. This interval is of fast solar wind with an average flow speed of 756 km/s and average Alfvén speed $\simeq$ 56 km/s. Due to the Ulysses orbit, which leaves the ecliptic plane, long uninterrupted intervals of data in fast solar wind streams may be observed.

3.3 Source of Nonaxisymmetry

3.3.1 The Local Coordinate System

We will work in the local coordinate system, where the principal axis is the direction of the background magnetic field, which orders the dynamics of the system. In order to make progress it is necessary to define a working definition for the background field, and so we use a scale-dependent local background magnetic field. The local background magnetic field is defined as $\hat{\mathbf{e}}_B(t,f) = \frac{\overline{\mathbf{B}}(t,f)}{|\overline{\mathbf{B}}(t,f)|}$, where $\overline{\mathbf{B}}(t,f)$ is the scale-dependent local average conducted with a Gaussian function due to the optimized characteristics in both temporal and frequency space.

The frequency spectrum of the local magnetic field may be seen for a specific scale on a test time-series in Fig. 3.2. The test signal is displayed in blue and has a flat spectrum of f^0. The specific scale of interest is shown by the vertical black dashed line, which is the centre of the wavelet spectral response, shown in red. The Gaussian average over which the local background field is defined for two different standard deviations are shown in magenta and black. The Gaussian window described by the Morlet envelope function is shown in magenta, whilst the Gaussian window used throughout this thesis is shown in black. The standard deviation of the Gaussian window used in this thesis is less than that of the Morlet envelope function, hence the presence of slightly more intermediate frequencies within the local background magnetic field estimate.

The local background field may be viewed as the sum of two components; a) the sum of spatial-temporal turbulent fluctuations on scales greater than the scale of interest b) an externally applied large-scale background field, which may in principle be zero. For turbulence within the solar wind, the Parker spiral may be seen as the

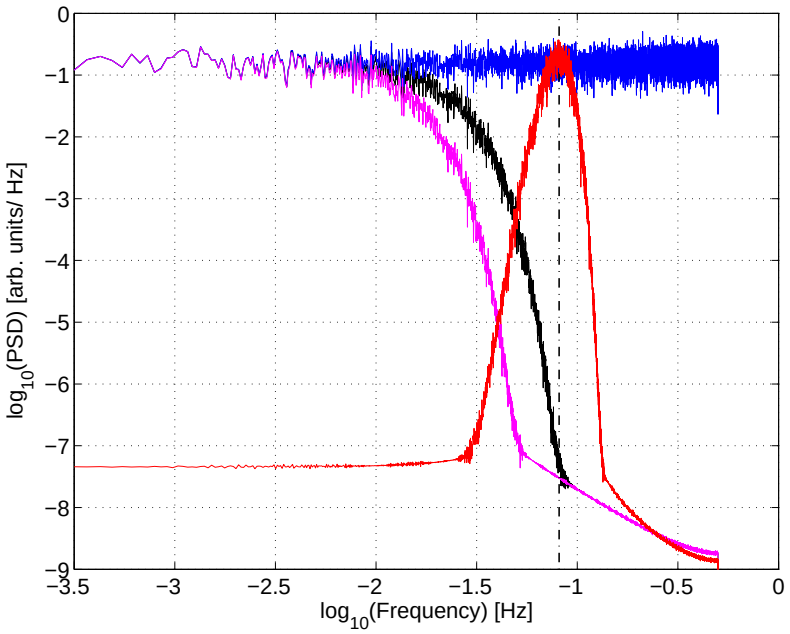

Figure 3.2: Demonstration of the frequency response for the local background magnetic field and fluctuations at a specific scale, indicated by the vertical dashed black line. The test signal is produced by a pseudo-random number at a cadence of 1 Hz to produce f^0 power spectral density, shown in blue. The frequency response for the Morlet wavelet centred on approximately 0.09 Hz is shown in red. The local background field produced by using the Gaussian wave packet for the Morlet wavelet and the prescribed Gaussian used to determine the local background field in this thesis are shown in magenta and black respectively.

large-scale externally applied magnetic field. Thus, the local background field is the background magnetic field actually experienced by an Alfvén wave on a specific spatial-temporal scale.

In the local coordinate system we use the velocity unit vector as a reference to decompose the perpendicular plane. In principle one would chose to use a scale-dependent velocity unit vector in conjunction with the magnetic field scale, however this is not possible due to the cadence of the velocity measurement. Thus, we use the unit vector that results from averaging over the entire interval. The solar wind velocity is dominated by the expansion, hence the velocity unit vector may be approximated by the radial direction, which is the unit vector directed from the Sun to the satellite. We define the perpendicular unit vectors as $\hat{\mathbf{e}}_{\perp,x}(t,f) = \hat{\mathbf{e}}_B(t,f) \times \frac{\overline{\mathbf{V}}}{|\overline{\mathbf{V}}|}$ and $\hat{\mathbf{e}}_{\perp,y}(t,f) = \hat{\mathbf{e}}_B(t,f) \times \hat{\mathbf{e}}_{\perp,x}$. This local coordinate system may be seen in Fig. 2.4, where the angle from the background magnetic field is defined as θ and the angle from $\hat{\mathbf{e}}_{\perp,x}$ is defined a ϕ.

We decompose fluctuations into the local coordinate system to produce a PSD estimate for the three components. This is shown in the main panel of Fig. 3.3, where blue, red and black correspond to the power in the direction of $\hat{\mathbf{e}}_{\perp,x}$, $\hat{\mathbf{e}}_{\perp,y}$ and $\hat{\mathbf{e}}_{\parallel,z}$ respectively. Error-bars are not displayed as they are typically less than the line widths used. The insert of Fig. 3.3 shows the power ratio for the two components of the perpendicular plane in the local coordinate system.

It can be seen from Fig. 3.3 that there is a nonuniform distribution of power within the perpendicular plane, which increases as the scale decreases. This analysis implies that the fluctuations in the perpendicular plane are not statistically axisymmetric with respect to the direction of the local background magnetic field. However, Fig. 3.3 is insufficient to demonstrate that the bulk flow direction is ordering the turbulence, as the bulk flow direction was chosen *ad hoc* to decompose the perpendicular plane. To conclusively demonstrate whether the bulk flow is important for the observed nonaxisymmetry we produce a power map as a function of θ and ϕ, which are angles within the local coordinate system, and statistically measure the alignment between the local coordinate system and the minimum variance coordinate system, which requires no *a priori* direction.

3.3.2 Power Distribution

We map the variance power as a function of frequency to investigate the variance anisotropy. We map the variance power within the local coordinate system, such that we bin power according to constant solid angle on the surface of a sphere of constant frequency/wavelet scale. We us 18 bins of θ covering $0^\circ - 180^\circ$ with

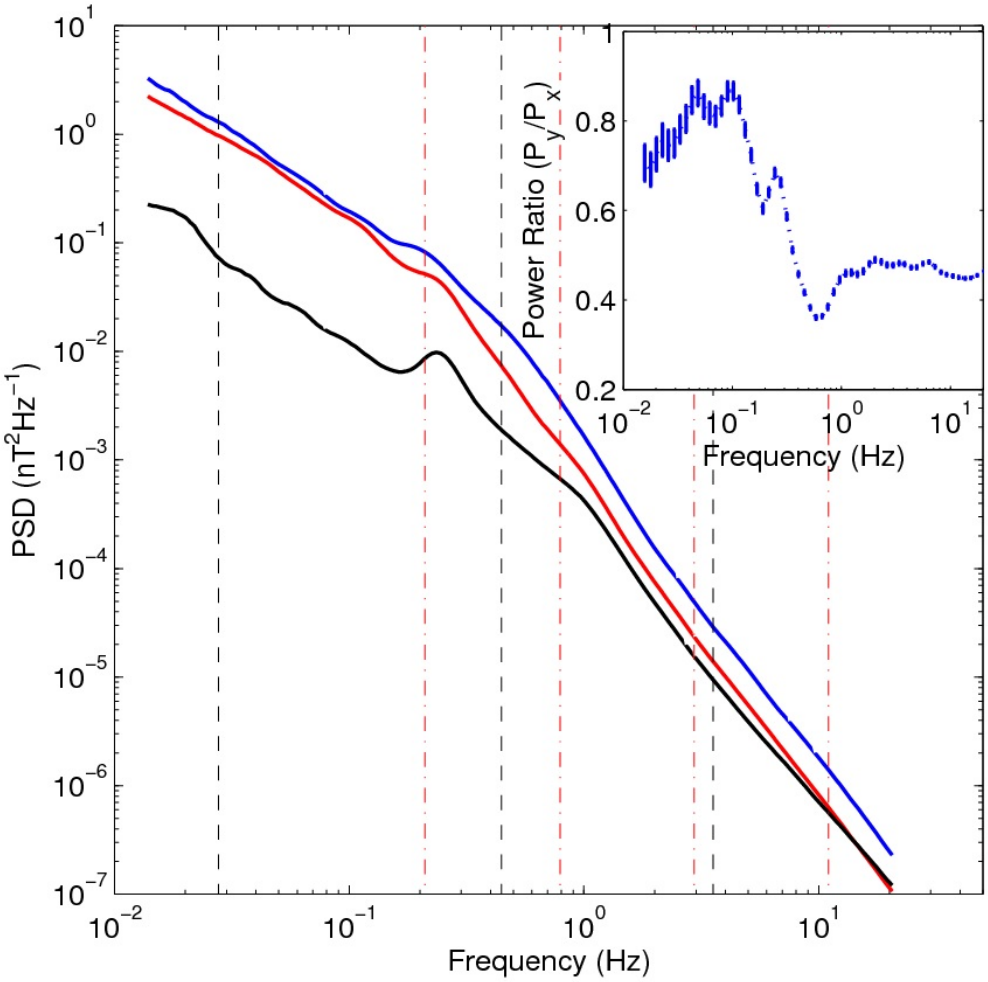

Figure 3.3: Main panel: The PSD for the three components of the local coordinate system, where $\hat{\mathbf{e}}_z, \hat{\mathbf{e}}_x, \hat{\mathbf{e}}_y$ are shown in black, blue and red respectively. The vertical black dashed lines correspond to the frequencies used in section 3.3.3. The vertical red dot-dashed lines correspond to the frequencies used in section 3.3.2. Insert: The ratio P_y/P_x highlights the degree of observed nonaxisymmetry.

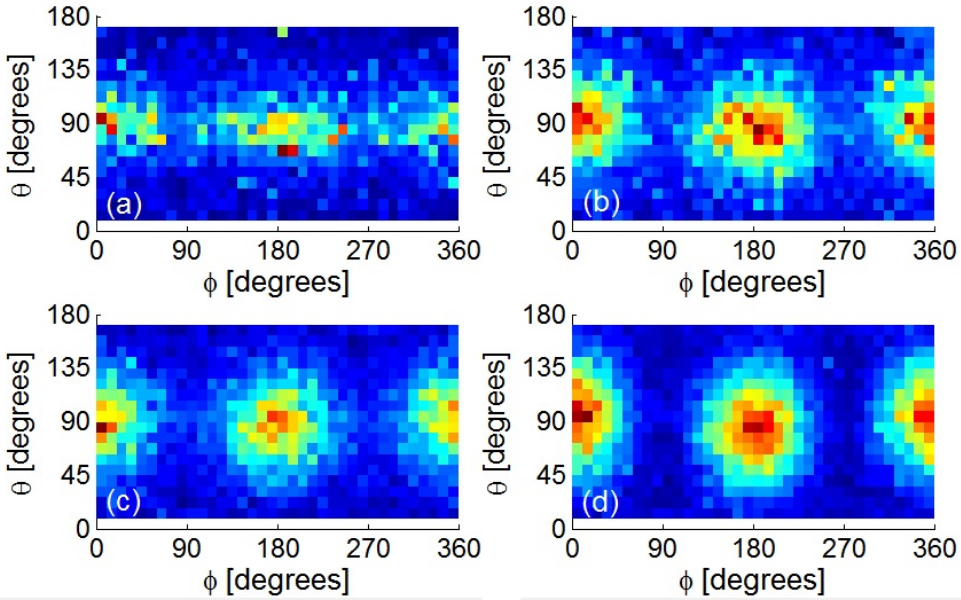

Figure 3.4: Power map displaying the power as a function of equal solid angle within the local coordinate system. The colour displays power in arbitrary units, where the difference between blue and red is approximately a factor of ten. The panels display different scales; a) 0.21 Hz ($\tau = 4.8$ s) b) 0.79 Hz ($\tau = 1.3$ s) c) 2.94 Hz ($\tau = 0.34$ s) d) 11 Hz ($\tau = 0.09$ s).

an inverse cosine distribution and 36 bins of ϕ covering $0° - 360°$ with a linear distribution. Thus the fluctuation power is separated into 648 bins per frequency, $P(f, \theta, \phi) = 2\Delta t|\tilde{u}(f, \theta, \phi)|^2$. Due to the number of bins there are strong limitations on accuracy and scale of producing such power maps. Thus, we limit our largest time-scale to approximately 4.8 s for a 75 minute interval.

We present power maps for the January 20th interval recorded by CLUSTER in Fig. 3.4. The scales that are shown are; a) 0.21 Hz ($\tau = 4.8$ s) b) 0.79 Hz ($\tau = 1.3$ s) c) 2.94 Hz ($\tau = 0.34$ s) d) 11 Hz ($\tau = 0.09$ s). The colour scale is numerically different for all panels, however the difference between red and blue is a factor of 10 in all panels. One can see that the power is predominantly perpendicular to the background magnetic field direction. In addition, there is a strong difference in power between the two perpendicular directions, with a preference on the direction that is perpendicular to both the background magnetic field and the solar wind flow velocity. The observed preference appears to increase as the scale decreases, however from the power maps it is not possible to determine whether this is due to higher accuracy at the smaller scales or is a consequence of physics.

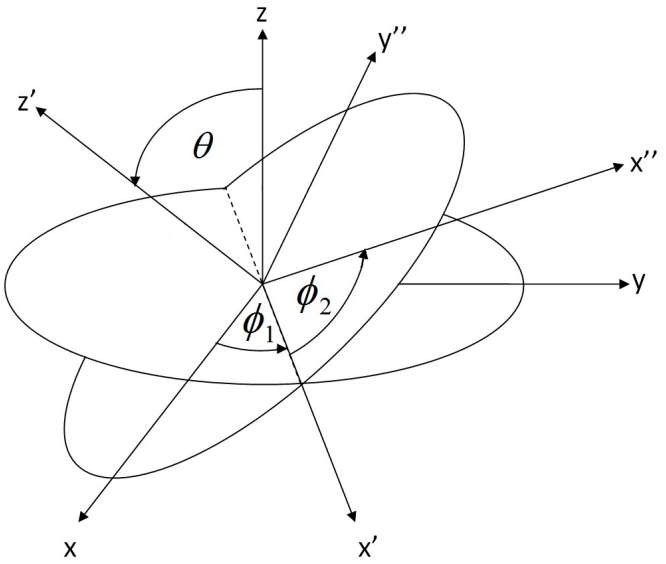

Figure 3.5: A diagram that displays how the coordinate system xyz undergoes the Euler rotations "ZXZ" to $x''y''z'$. The first rotation, ϕ_1, is about the z axis, the second rotation, θ, is about the x' axis and the third rotation, ϕ_2 is about the z' axis.

3.3.3 Minimum Variance Coordinate System

Minimum variance analysis (MVA) was described in Chapter 2. The key to MVA is that is produces an orthogonal coordinate system that is independent of the any *a priori* coordinate system. Thus, we chose to calculate the MVA coordinate system to find the principle axis of the fluctuations on a given scale. Then we will use Euler rotations to calculate the statistical correlation between the intrinsic axis of the fluctuations and the local coordinate system.

Euler's rotation theorem is that any rotation may be described completely by a maximum of three angles. The order of rotations is important, but not unique. Here we use the "ZXZ" sequence. The first rotation, ϕ_1, is performed with respect to the background magnetic field axis (Z), the second rotation, θ, is preformed with respect to the $\hat{\mathbf{e}}_{\perp,x}$ axis (X) and the third rotation, ϕ_2, is performed with respect to the Z axis again. The Euler angles are shown in Fig. 3.5, where the initial coordinate system is xyz and the final coordinate system is x"y"z' (NB: z' = z"). For the MVA and local coordinate system to be identical all angles (i.e. θ, ϕ_1, ϕ_2) must be zero.

By using this the above definition for the Euler angles it is possible to directly compare the results obtained with respect to θ with previous studies that have predominantly concentrated on the correlation between the background magnetic

field direction and the direction of minimum variance (e.g. see Perri et al. [2009] and references within). The angles $\phi_{1,2}$ allow for one to quantify the dependence of the nonaxisymmetric observations upon the macroscopic direction of the flow velocity.

First we display the statistical results for θ as a function of scale. This can be seen in Fig. 3.6. The probability distribution for θ is shown for four different scales and bin size has been selected by the inverse cosine function to conserve solid angle. The smallest time-scale shown is 0.009 s ($\sim$ 100 Hz), shown in black, and corresponds a ensemble average of four data points. The smallest scale is dominated by instrument noise (e.g. instrument sensitivity and measurement discretization), and as such provides an excellent test to show whether our method is correct, as well as displaying any bias that may exist in the data. It can be seen that the noise provides a distribution that is approximately uniform, with a value of one with our normalization, which is the expectation for an isotropic random variable, such as instrument noise. The other scales that are displayed are that of 0.282 s, 2.25 s and 36.0 s in red, magenta and blue respectively. It can be seen that as the scale increases the correlation between the local coordinate system and the direction of minimum variance increases, as the distribution tends to $\theta = 0$. This is in general agreement with previous studies of the inertial range scales, however there is a contradiction with the results of [Perri et al., 2009], who claim that as the time-scale tends to $\tau = 0.009$ s the distribution becomes predominantly perpendicular. It is likely that the authors of [Perri et al., 2009] have not accounted for the solid angle effect, and so use a linear distribution of θ bin size instead of the inverse cosine distribution of bin size used here. The use of a linear distribution of bin size leads to a greater solid angle bin size as $\theta \rightarrow 90^{\circ}$. Therefore, there is a greater probability for the minimum variance direction being analyzed as perpendicular to the background magnetic field direction if the underlying distribution is uniform across θ when an inverse cosine function is not used for the bin size to correct for solid angle effects.

We have shown that our method is normalized correctly and returns the standard result for θ. Now we extend the analysis to the generalized case by considering the distribution of the $\phi_{1,2}$, which are necessary to uniquely describe the alignment of the two coordinate systems. The bin sizes are a linear function of angle for $\phi_{1,2}$. Recall that for a perfect agreement between the two coordinate systems it is necessary that the both $\phi_{1,2} = 0$. In panels (a) and (c) of Fig. 3.7 the same time-scales are shown as for the θ case, such that 0.009 s (111 Hz), 0.282 s (3.54 Hz), 2.25 s (0.44 Hz) and 36.0 s (0.028 Hz) are displayed in black, red, magenta and blue respectively. In panels (b) and (d) we display the fraction of counts in

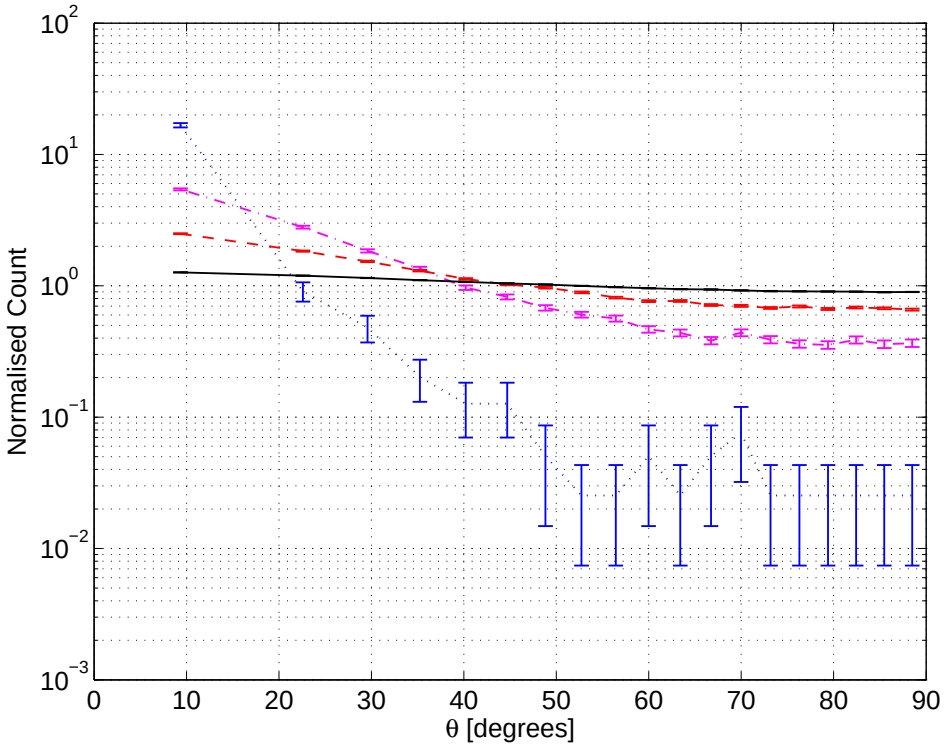

Figure 3.6: Alignment between the minimum variance and local background magnetic field direction, measured by θ. The bins are inverse cosine distributed to conserve solid angle. The smallest scale, 0.009 s is dominated by noise and displayed in black. The other scales shown are that of 0.282 s, 2.25 s and 36.0 s displayed in red, magenta and blue respectively.

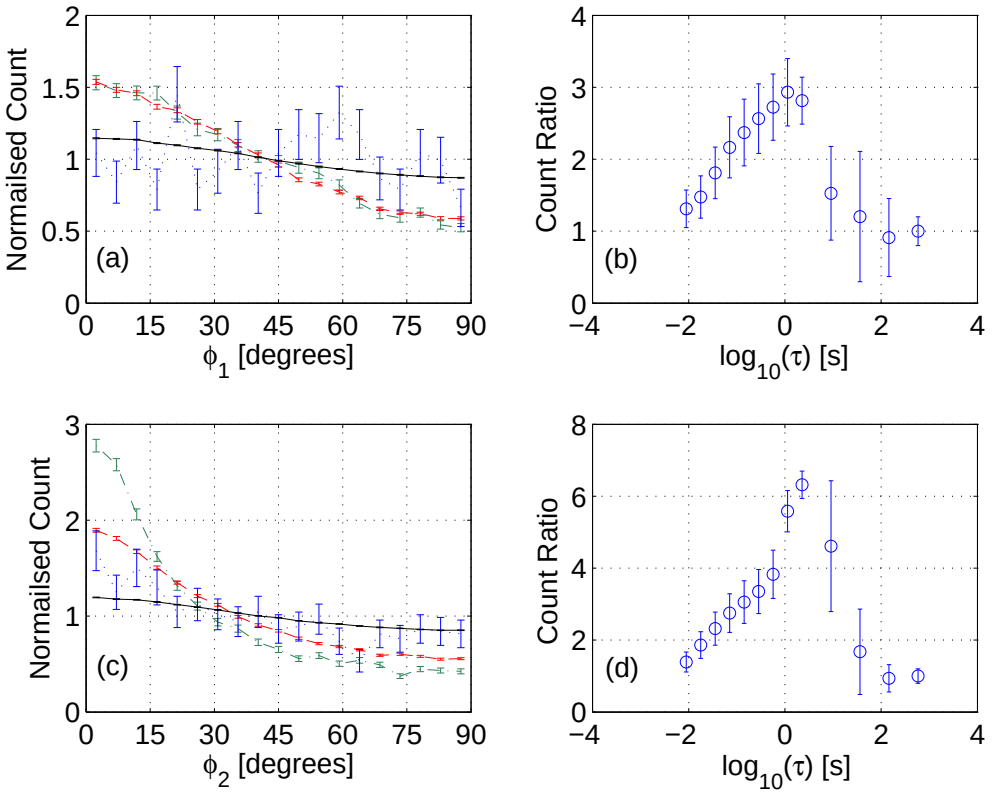

Figure 3.7: Left hand panels: Alignment between the maximal variance and maximal power for the local coordinate system. The bins are linearly distributed. The smallest temporal scale, 0.009 s, is dominated by noise and displayed in black. The other temporal scales shown are that of 0.282 s, 2.25 s and 36.0 s displayed in red, magenta and blue respectively. Right hand panels: Ratio of counts in the range $0° \rightarrow 10°/80° \rightarrow 90°$ to quantify the degree of alignment.

the range $0° - 10°$ divided by the counts in the range $80° - 90°$. We use this measure to quantify the degree of agreement between the two coordinates systems as the angular distribution is a smooth function. A value larger than one shows an increasing strong alignment, less than one shows increasing anti-alignment and a value of one shows no agreement between the to coordinate systems. Interestingly, the best alignment between the direction of maximum variance and $\hat{\mathbf{e}}_{\perp,x}$ is achieved in the kinetic scales, as seen in the power maps of section 3.3.2 and PSD of section 3.3.1.

We have established that the power measured *in-situ* is not axisymmetric about the background magnetic field. The distribution is a smooth function of ϕ that oscillates, with a maximum power that corresponds to alignment to $\pm\hat{\mathbf{e}}_{\perp,x}$. The observed nonaxisymmetric power is unlikely to be directly due to plasma physics, as this would imply that the velocity can not be removed via a Galilean transformation and the influence of the macroscopic flow affects the kinetic scale dynamics. Therefore, the most likely interpretation is that the observed nonaxisymmetry is due to *in-situ* sampling at-a-point via Taylor's hypothesis. We begin by constructing a simple model by superposition of waves and then sample a MHD simulation to replicate a satellite sampling via Taylor's hypothesis. Finally, we will analytically model the nonaxisymmetric observations, which be able to explain why the observed nonaxisymmetry is greater in the kinetic range.

3.4 Two-Dimensional Model

3.4.1 Linear Model

Our model data must fulfill the solenoid criteria, such that $\nabla\cdot\mathbf{B} = 0$. This is achieved by summing a series of transverse plane wave, such that the wave vector, $\mathbf{k}$, is always perpendicular to the fluctuations. We limit ourselves to the two-dimensional case, such that wave vectors lie in the x-y plane, and sum the waves such that the distribution is axisymmetric about the background magnetic field direction, $B_0\hat{\mathbf{e}}_z$. The orientation is $\mathbf{k} \perp \mathbf{B}_0$, $\delta\mathbf{B} \perp \mathbf{k}$ and $\delta\mathbf{B} \perp \mathbf{B}_0$, such that the linear model represents noninteracting Alfvén-type waves with $\mathbf{k}$ perpendicular to the background field direction. This orientation is shown in Fig. 3.8, where a wave vector is shown in blue and a set of fluctuations are shown in red for the case $\theta = \xi = 0$.

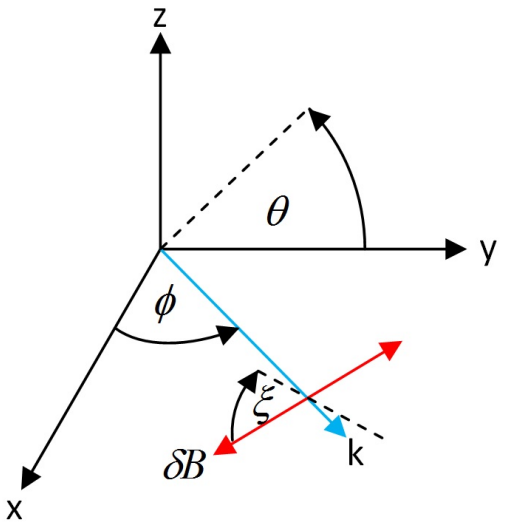

Figure 3.8: Diagram of the coordinate system necessary for the generalised superposition model of transverse wave. The wave vector, $\mathbf{k}$ is shown in blue. The fluctuations, δB, are shown in red. ϕ is the angle between the wave vector, $\mathbf{k}$, and $\hat{\mathbf{e}}_x$. θ is the angle between the wave vector, $\mathbf{k}$, and the x-y plane. ξ is the polarization of the fluctuations with respect to the x-y plane, where $\xi = 0$ and $\xi = \pi/2$ correspond to δB parallel and normal to the x-y plane respectively.

The general equations of the individual components are:

$$\begin{aligned} B_x &= k^{\alpha}[\sin(\theta)\sin(\xi)\cos(\phi) - \sin(\phi)\cos(\xi)]\cos(\mathbf{k}\cdot\mathbf{r} + \psi) \\ B_y &= k^{\alpha}[\sin(\theta)\sin(\xi)\sin(\phi) - \cos(\phi)\cos(\xi)]\cos(\mathbf{k}\cdot\mathbf{r} + \psi) \\ B_z &= k^{\alpha}[\cos(\theta)\sin(\xi)]\cos(\mathbf{k}\cdot\mathbf{r} + \psi). \end{aligned}$$

For our model we use $\theta = \xi = 0$ and sum over k_j and ϕ_i. Thus, the equations for the individual components after superposition are:

$$\begin{aligned} B_x &= \Sigma_{i,j}\ k_j^{-h}\sin(\phi_i)\cos(k_j[x\cos(\phi_i) + y\sin(\phi_i)] + \psi) \\ B_y &= \Sigma_{i,j}\ k_j^{-h}\cos(\phi_i)\cos(k_j[x\cos(\phi_i) + y\sin(\phi_i)] + \psi), \end{aligned}$$

where a $\Sigma_{i,j}$ denotes a sum over ϕ and wavenumber respectively, h corresponds to the Hurst exponent and prescribes a scaling exponent to simulate an inertial range in the PSD, x and y correspond to the spatial domain and ψ is a random phase generated for every iteration, such that $-\pi \leq \psi < \pi$. Note that for our chosen geometry the only difference between B_x and B_y is highlighted in red text.

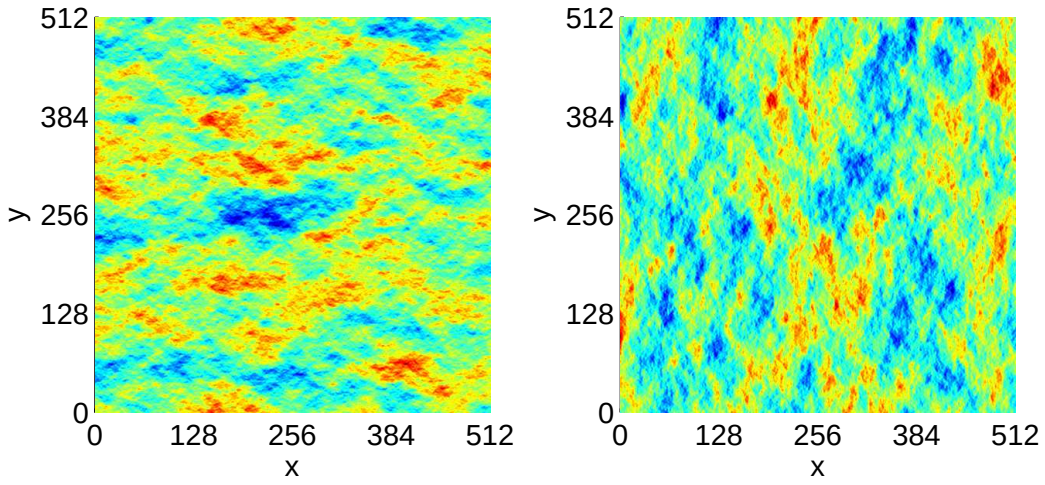

Figure 3.9: An example of the output for the linear model composed of 160 different frequencies spread equally on a logarithmic scale from 10^{-4} to 1 Hz, with each frequency composed of 900 different ϕ, with a distribution $\phi = [0 : 0.4 : 359.6]$. The red and blue colours refer to positive and negative values respectively. B_x and B_y are shown in the left and right panels respectively.

Here we present the B_x and B_y components of the random field generated by the linear model over a domain of 512^2 in Fig. 3.9. The B_z component is not displayed, as it is an arbitrary constant value under the conditions set above. The left and right panels of Fig. 3.9 show the magnetic field components B_x and B_y, where red and blue correspond to positive and negative values respectively. It can be seen that the model magnetic field of B_x varies more rapidly in the y direction than the x direction and vise versa for B_y.

To quantify the difference in power we sample both B_x and B_y in the same direction to model a satellite sampling our model data under Taylor's hypothesis. We use the local coordinate system, such that the direction of sampling is taken to be $\hat{\mathbf{e}}_x$ and $\hat{\mathbf{e}}_x$ completes the orthogonal set in the x-y plane as described in section 3.3.1. The time-series constructed from the linear model are composed of 160 different frequencies spread equally on a logarithmic scale from 10^{-4} to 1 Hz, with each frequency composed of 900 different ϕ, with a distribution $\phi = [0 : 0.4 : 359.6]$. We then calculate the PSD in the local coordinate, such that P_y and P_x are calculated in the direction of sampling and the direction perpendicular perpendicular to both the background field and sampling respectively. The power ratio, P_y/P_x, is shown in Fig. 3.10 for different values of h. The power ratio has been calculated by averaging over 10 model runs, where three different values of $h = [1/4, 1/3, 1/2]$ are shown in blue, red and black respectively. The error-bars display the spread of analyzing our

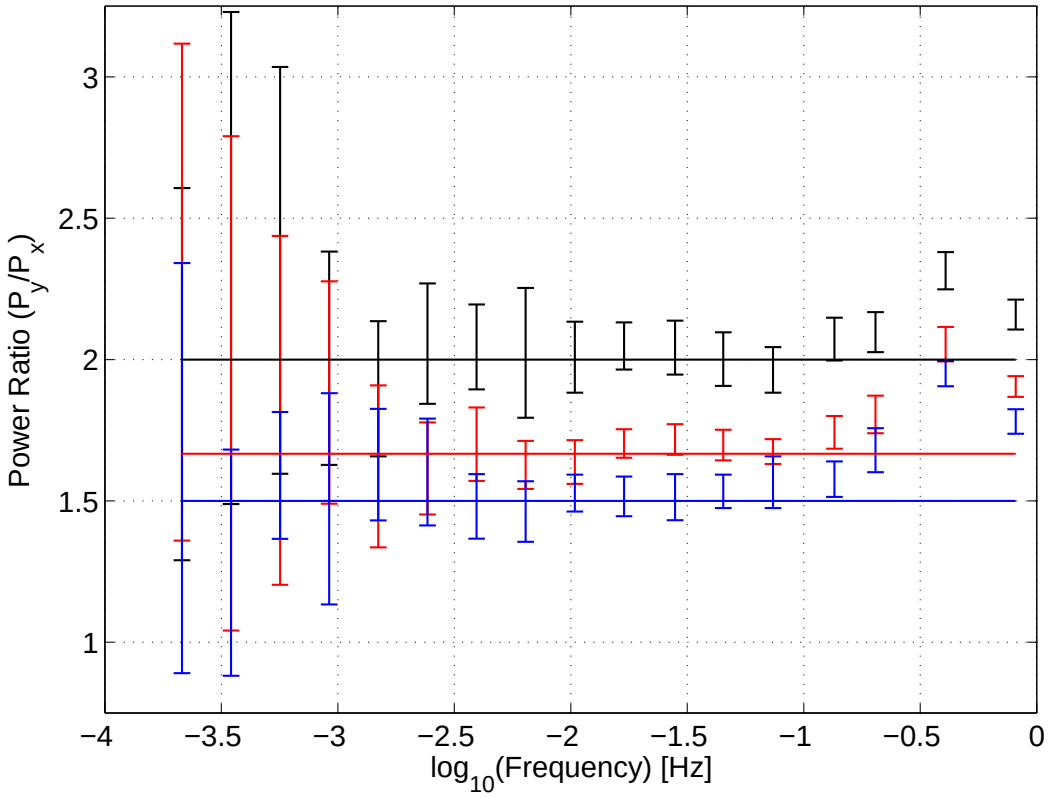

Figure 3.10: The nonaxisymmetry observed in the local coordinate system for the linear superposition model are displayed with errorbars. The solid lines correspond to the Hurst exponent used in the model. Three different exponent are shown, $h = [1/4, 1/3, 1/2]$, displayed in blue, red and black respectively.

linear model over ten separate constructions. The error-bars estimates display three standard error defined as, $\epsilon = 3\sigma/\sqrt{N}$, where σ is the standard deviation across N runs. The solid lines show the spectral density exponent that corresponds to the value of h.

It can be seen that for scales larger than approximately one decade of "inertial" range P_y/P_x is approximately equal to the value of the spectral exponent. It can also be seen the uncertainty increases rapidly as a function scale after approximately three decades of scaling. The increase in uncertainty must be attributed to the sensitivity of the analysis method for finite date length, as the linear model is self-similar on all scales displayed in Fig. 3.10.

3.4.2 MHD Direct numerical simulation

We consider two MHD simulations; Case I is that of a globally isotropic freely decaying turbulence, Case II is that of a forced turbulence simulation with a strong externally applied magnetic field B_0, such that $\delta B_{rms}/B_0 \sim 0.2$. The forced turbulence has a constant background magnetic field direction, such that it is possible to consistently sample approximately perpendicular to the local background magnetic field. Details of the simulations used are given in Müller and Grappin [2005]. An example of a snapshot of B_x for the forced simulation is shown in Fig. 3.11, where red and blue correspond to large magnitude positive and negative values of the magnetic field respectively.

Simulation I, which concerns globally isotropic freely decaying turbulence, is in initialized as smooth fields with random phases. There is an equipartition between the kinetic and magnetic field energy, with the fluctuation amplitudes distributed according to $\exp(-k^2/(2k_0^2))$, where $k_0 = 4$. Simulation II, which concerns forced turbulence, is initialized with an equipartition between the kinetic and magnetic field energy. The forcing maintains the ratio of fluctuations to background magnetic field strength, such that $\delta B_{rms}/B_0 \sim 0.2$. The forcing is implemented by freezing modes where $k \leq 2$.

We sample snapshots in time of the simulations of MHD turbulence. A snapshot in time enforces that there is no temporal evolution of the simulation whilst a sample path is created, and so a time-series generated from a sampling line through the simulation snapshot emulates a single satellite observing the magnetic field in-situ via Taylor's hypothesis. The simulation undergoes equidistant sampling, which defines the constant pseudo-macroscopic flow velocity $\mathbf{V}$.

3.4.3 Analytical Interpretation

A complete understanding of the nonaxisymmetric observations of the solar wind magnetic field fluctuations must reproduce the observations, such that the observed nonaxisymmetry is stronger in the kinetic range than the inertial range. This result is well reproduced by the linear superposition model. We formulate the linear superposition model in Fourier space to explain how the spectral exponent is related to the observed nonaxisymmetry. As with the superposition model, we consider the two-dimensional geometry, therefore $\mathbf{V}_{sw} \perp \mathbf{B}_0$. We fix the coordinate system, such that the solar wind velocity, $\mathbf{V}_{sw}$, and background magnetic field, $\mathbf{B}_0$, are directed along the y and z respectively. Thus, the magnetic fluctuations $\delta\mathbf{B}$ associated with the waves are in the x-y plane. If the Fourier amplitudes of the fluctuations are

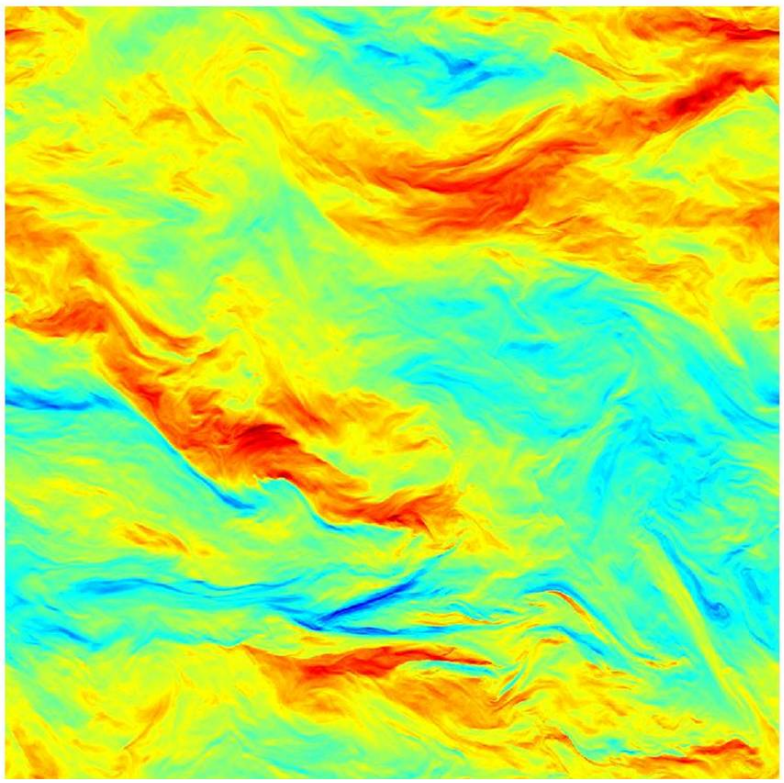

Figure 3.11: A snapshot of the B_x component produced by the MHD simulation. The positive and negative values are shown in red and blue respectively.

$\delta\mathbf{B}(\mathbf{k})$ then under Taylor's hypothesis the energy density $P_y(\omega)$ and $P_x(\omega)$ observed for the components parallel and perpendicular to $\mathbf{V}_{sw}$ are given by

$$P_{y,x}(\omega) = \frac{1}{8\pi}\int \mathrm{d}^3\mathbf{k}|\delta\mathbf{B}_{y,x}(\mathbf{k})|^2\delta(\omega - \mathbf{k}\cdot\mathbf{V}_{sw}), \tag{3.1}$$

where $\omega = 2\pi f$. We assume one may integrate over $\mathbf{k}_\parallel$ to obtain

$$P_y(\omega) = \int \mathrm{d}^2\mathbf{k}_\perp E_{2D}(\mathbf{k}_\perp)\delta(\omega - k_y V_{sw})\cos^2\phi, \tag{3.2}$$

$$P_x(\omega) = \int \mathrm{d}^2\mathbf{k}_\perp E_{2D}(\mathbf{k}_\perp)\delta(\omega - k_y V_{sw})\sin^2\phi, \tag{3.3}$$

where $E_{2D}(\mathbf{k}_\perp)$ is two dimensional spectrum of fluctuations and ϕ is the angle between $\mathbf{k}_\perp$ and $\mathbf{V}_{sw}\times\mathbf{B}_0$. Expressions (3.2) and (3.3) generally integrate to give $P_x(\omega) \neq P_y(\omega)$. In particular, for axisymmetric fluctuations $E_{2D}(\mathbf{k}_\perp) = E_{2D}(k_\perp) = Ck_\perp^{-\gamma-1}$, where γ corresponds to a one-dimensional spectrum, Eqs. (3.2-3.3) yield

$$P_y(\omega) = C\frac{\omega^2}{V_{sw}^2}\int\left(\frac{\omega^2}{V_{sw}^2} + k_x^2\right)^{-(\gamma+3)/2}\mathrm{d}k_x, \tag{3.4}$$

$$P_x(\omega) = C\int k_x^2\left(\frac{\omega^2}{V_{sw}^2} + k_x^2\right)^{-(\gamma+3)/2}\mathrm{d}k_x. \tag{3.5}$$

This can be integrated in terms of Beta functions and manipulated for $\gamma > 1$. Therefore, we obtain

$$P_y(\omega)/P_x(\omega) = 1/\gamma. \tag{3.6}$$

Thus, the ratio $P_y(\omega)/P_x(\omega)$ is a function of the spectral exponent as shown in the linear superposition model and observed in solar wind.

3.4.4 Results of 2D model

We plot the power ratios for MHD simulation, satellite observations and expected ratio of P_y/P_x in Fig. 3.12. We plot the estimated ratio, P_y/P_x, of the CLUSTER interval [Jan 20, 2007, 12:00-13:15 UT] and STEREO-A interval with 99% statistical uncertainty in blue and green respectively. We estimate the spectral exponent to be $\gamma = 1.5 \pm 0.1$ for both inertial ranges. We plot the expected value of P_y/P_x with this range of γ in the left-hand gray box. The right-hand gray box corresponds to the estimated range for the spectral exponent within the kinetic range displayed, approximately 2-11 Hz, as $\gamma = 2.76 \pm 0.5$. The red dashed and black solid lines

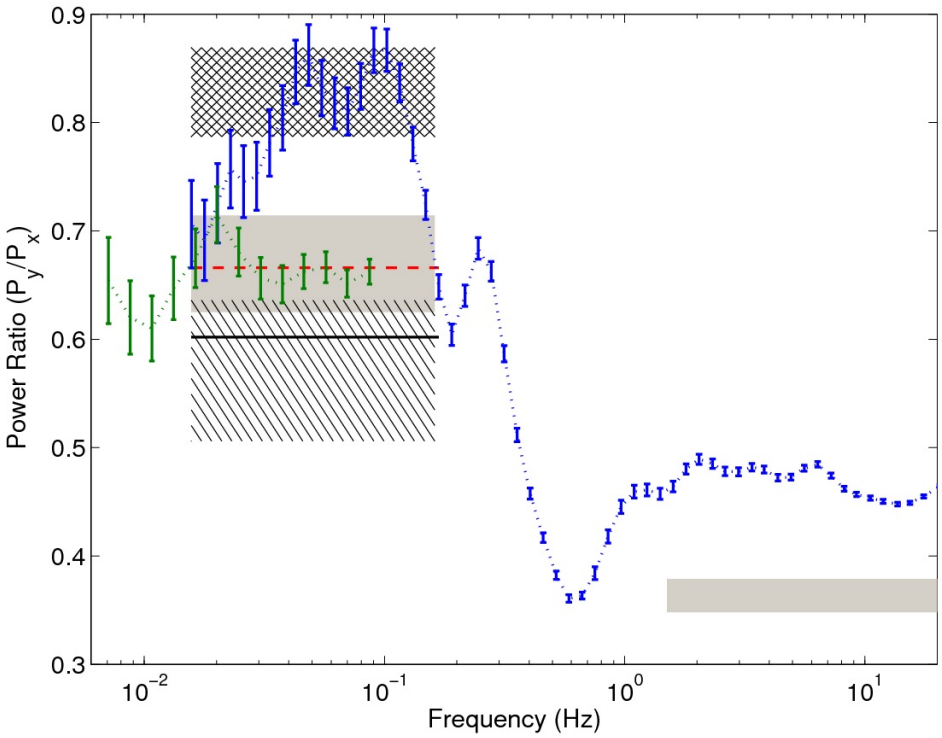

Figure 3.12: Nonaxisymmetric ratio for the CLUSTER and STEREO-A observations are shown in blue and green respectively. The freely decaying and forced MHD simulations are shown with cross-hatched and hatch areas. The expected value for the observed nonaxisymmetry from the observed γ, IK-like and K41-like scaling are shown by the gray areas, dashed red line and solid black line respectively.

correspond to a spectral exponent in the inertial range of $\gamma = 3/2$ and $\gamma = 5/3$ respectively. The cross-hatched and hatch area shown the values obtained from the freely decaying and forced MHD simulations respectively.

For the CLUSTER interval the kinetic scales have an approximately constant ratio. However the transition scales, approximately 0.1-1 Hz, are highly variable with a clear peak that corresponds to the spin-tone of the CLUSTER satellite. The scales between 0.001 to 0.1 Hz show a value that slowly tends to the expected value (left-hand gray box) as the scale increases. Compared to the STEREO-A interval, which is approximately constant and within the expected region for the spectral exponent. We tentatively speculate that the CLUSTER results are contaminated for scales within the range of approximately 0.05 to 1 Hz by a combination of the spin-tone and data merging process from the two instruments and suggest that if a significantly longer interval were available we would see increasing agreement with

the predictions from our model.

The main difference between the two MHD simulations, with respect to our analysis, is the geometry of $\mathbf{V}_{sw}$ relative to $\mathbf{B}_0$. As in the forced simulation a strong externally applied magnetic field serves to restrict the geometry to quasi-perpendicular sampling, i.e. $\theta = 90^\circ \pm 15^\circ$. It may be seen from the results of the two distinct MHD simulations that the observed nonaxisymmetry is strongest when the sampling direction is perpendicular to the background magnetic field.

There is an observed nonaxisymmetric variance power distribution in the inertial range, which becomes stronger in the kinetic range. We have binned the variance power as a function of solid angle on the surface of a sphere of constant scale and conducted Euler rotations to compare the alignment of the local coordinate system with that of the minimum variance coordinate system. It has been found that the nonaxisymmetric distribution always has a preferential direction, such that the direction $\hat{\mathbf{e}}_{\perp,x}(t,f) = \hat{\mathbf{e}}_B(t,f) \times \frac{\overline{\mathbf{V}}}{|\overline{\mathbf{V}}|}$ contains the dominant power. We have shown that this effect can be simulated with a simple superposition of transverse waves, such that $\nabla \cdot \mathbf{B} = 0$. We also find agreement with MHD simulations, where the reduced effect seen in the freely decaying simulation suggests that a the maximum power difference is observed when the geometry is restricted to sampling in the plane perpendicular to the background magnetic field, which is not possible in the freely decaying model due to the constant spatial/temporal evolution of the background magnetic field that results from the average of the root-mean-square of the fluctuations. Thus, our two dimensional model is capable of both predicting the level of observed nonaxisymmetry and can account for the observed increase in the difference between the two perpendicular directions in the kinetic range, as a consequence of the spectral exponent magnitude. We now consider how these observational results may be extended to the three-dimensional case and used as a tool to distinguish between models of turbulence.

3.5 Extension to Three-Dimensions

In this section we will see that it is possible to use the observed nonaxisymmtric variance power as a direct test for theories of turbulence. In order to discriminate between theories explicit information of the θ dependence is necessary. We consider two models of turbulence, that of Goldreich and Sridhar [1995] and a heuristic model known as "Slab + 2D" (S2D hereafter).

The S2D model assumes that the turbulent fluctuations are a linear combination of two components: a "slab" component that contains only wave vectors

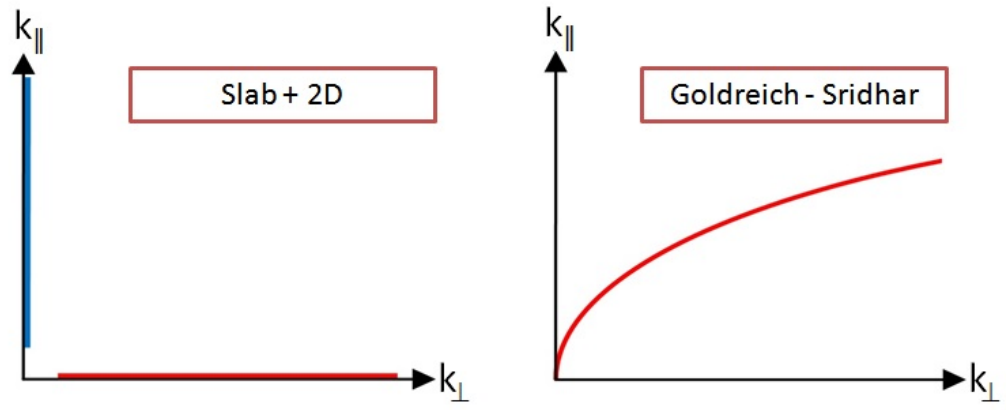

Figure 3.13: Schematic showing the main difference between the GS and S2D model of turbulence. Left panel: The S2D model is composed of two linearly independent components shown in red and blue. Right panel: The GS model is composed of one component that is a function of $k_{\parallel} \sim k_{\perp}^{2/3}$.

aligned to the background magnetic field and a "2D" element with wave vectors confined to the perpendicular plane with respect to the background magnetic field, which have been considered in the previous section. This model is supported by the so-called "Maltese cross" pattern seen in the magnetic field correlation function [Matthaeus et al., 1990] and is mathematically convenient in studies of cosmic ray scattering (e.g. see Shalchi [2009] and references within). A schematic of the difference between the S2D and Goldreich and Sridhar [1995] wave vectors is shown in Fig. 3.13. It is clear from Fig. 3.13 the two components of the S2D model are independent, with the slab and 2D components displayed in blue and red respectively. The scaling relation of $k_{\parallel} \sim k_{\perp}^{2/3}$ is displayed by one function in the GS model.

We begin by stating the three-dimensional form of equation 3.1, which may be expressed as

$$\tilde{P}_{ij}(f,\theta) = \int d^3k P_{ij}(\mathbf{k}) \delta(2\pi f - \mathbf{k}\cdot\mathbf{V}_{sw}). \tag{3.7}$$

where $\tilde{P}_{ij}(f,\theta)$ is the observed spectral tensor, $P_{ij}(\mathbf{k})$ is the actual spectral tensor as a function of wave vector and θ is the angle between the solar wind velocity and the background magnetic field direction. Therefore, it is possible to express the axisymmetry as

$$R(\theta, f) = \frac{\tilde{P}_{xx}(f,\theta)}{\tilde{P}_{yy}(f,\theta)} \tag{3.8}$$

We now calculate $R(\theta, f)$ for the GS and S2D models, such that a comparison with

observations may be made.

3.5.1 GS Nonaxisymmetry

We will assume that for the GS model all parallel components of the spectral tensor vanish so that $P_{zi}(\mathbf{k}) \equiv \mathbf{0}$, consistent with other studies Bieber et al. [1996]. The perpendicular components for the GS model are related to the power tensor in the following manner:

$$P_{ij}^{GS}(\mathbf{k}) = \frac{E(\mathbf{k})}{4\pi k_\perp^2}\Pi_{ij}, \tag{3.9}$$

where $\Pi_{ij} = \delta_{ij} - k_{\perp i}k_{\perp j}/k_\perp^2$ and from Ref. Goldreich and Sridhar [1995]:

$$E(\mathbf{k}) = C_K \frac{\varepsilon^{2/3}L^{1/3}}{k_\perp^{10/3}} g\left(\frac{k_\parallel L^{1/3}}{k_\perp^{2/3}}\right). \tag{3.10}$$

Here C_K is the Kolmogorov constant, L is the characteristic injection scale, ε is the energy dissipation rate and g is a positive symmetric function related to the scaling between $k_\parallel$ and $k_\perp$, where $g(0) = 1$ and $\int_0^\infty g(z)dz = 1$ [Goldreich and Sridhar, 1995]. The theoretical prediction of the GS model is determined by numerical integration of Eqs. (3.7), (3.9) and (3.10) substituted into Eq. (3.8). The result is not sensitive to the functional form of the scaling function g. We use the exponential function, such that $g = \exp(-L^{1/3}|k_\parallel|/k_\perp^{2/3})$.

We use the balanced MHD turbulence formalism of critical balance. However, turbulence in the fast solar wind is known to be imbalanced, such that the energy associated with $\mathbf{z}^+$ is greater than that of $\mathbf{z}^-$ [Bruno and Carbone, 2005]. An imbalanced extension to the GS model [Lithwick et al., 2007] predicts the same spectral exponents of both dominant and subdominant waves and the same scaling relation as the balanced GS model. Thus, given isotropy of the turbulence at the injection scale L, imbalance of the turbulence does not affect the ratio defined by equation (3.8).

3.5.2 S2D Nonaxisymmetry

We follow the prescription of Bieber et al. [1996]. However, we specify distinct spectral exponents q_s and q_{2D} for the slab and 2D components, such that they agree with observations (e.g. see Horbury et al. [2008]; Wicks et al. [2010] and references within). As $R(\theta, f)$ is sensitive to the perpendicular spectral exponent we consider only variation in q_{2D} and use a constant value of $q_s = 2$ throughout for simplicity.

In this case the ratio $R_{S2}(\theta, f)$ predicted by the S2D model is

$$R_{S2}(\theta, f) = \frac{A_c \left(\frac{2\pi f L}{V_{sw}\cos\theta}\right)^{1-q_s} + q_{2D}\left(\frac{2\pi f L}{V_{sw}\sin\theta}\right)^{1-q_{2D}}}{A_c \left(\frac{2\pi f L}{V_{sw}\cos\theta}\right)^{1-q_s} + \left(\frac{2\pi f L}{V_{sw}\sin\theta}\right)^{1-q_{2D}}}, \tag{3.11}$$

where L is the injection scale (we assume that both components have the same injection scale) and A_c is a constant that characterizes the energy ratio of slab and 2D components. Since $q_s \neq q_{2D}$ the relative power of the components is f dependent, as is the ratio $R_{S2}(\theta, f)$. Observations Bieber et al. [1996] give a $1:4$ energy ratio between slab and 2D components and we will fix this at the injection scale L, which fixes the constant $A_c \approx 0.5$.

We plot the theoretical predictions for both the GS and S2D model in Figure 3.14, for $\theta = [5°, 85°]$. The ratio R is plotted using normalized frequency $F = 2\pi f L/V_{sw}$ and we show two different cuts through the surface $R(\theta, F)$; for $F = 36$ (upper plot) and $F = 3$ (lower plot) in the left panels and for $\theta = 25°$ (upper plot) and $\theta = 45°$ (lower plot) in the right panels. The S2D model is indicated by red symbols on the plot, with circles for Kolmogorov $q_{2D} = 5/3$ and diamonds for Iroshnikov-Kraichnan $q_{2D} = 3/2$. The GS model prediction is indicated by the black squares. For completeness, we use the data to obtain $q_{2D} = 1.59$, this gives an S2D model result shown by the solid red line.

For underlying turbulence that is axisymmetric, with $E(k_\perp) \sim k_\perp^{-\gamma_\perp}$ the observed $R(\theta, f) \to \gamma_\perp$ for $\theta \to 90°$ for all of these curves, as seen in section the two-dimensional case considered earlier. It can be seen in the left panels of Figure 3.14 that the predicted $R(\theta, f)$ for the GS and S2D models are distinct for intermediate values of θ in the transition $R(\theta = 0° \to 90°, f)$. The GS model form is concave, whereas the S2D model is strongly convex. This provides a strong test against observations provided the statistical variability is smaller than the difference between the predicted curves. Importantly, the model predictions are maximally distinct for intermediate angles (i.e. $\theta \sim 20° - 40°$) and as we shall see, this is where the observations tend to be more statistically significant as there more samples.

3.5.3 Observations

We use the continuous wavelet transform (CWT) with a Morlet wavelet to resolve vector fluctuations $\delta\mathbf{B}(t, f)$ in time t and frequency f. The scale dependent local field is calculated via the convolution of a Gaussian window as outlined in previously. We use the Ulysses interval described in section 3.2, as it is possible to use 55 days of continuous fast wind. We verified that the systematic change of radial distance of

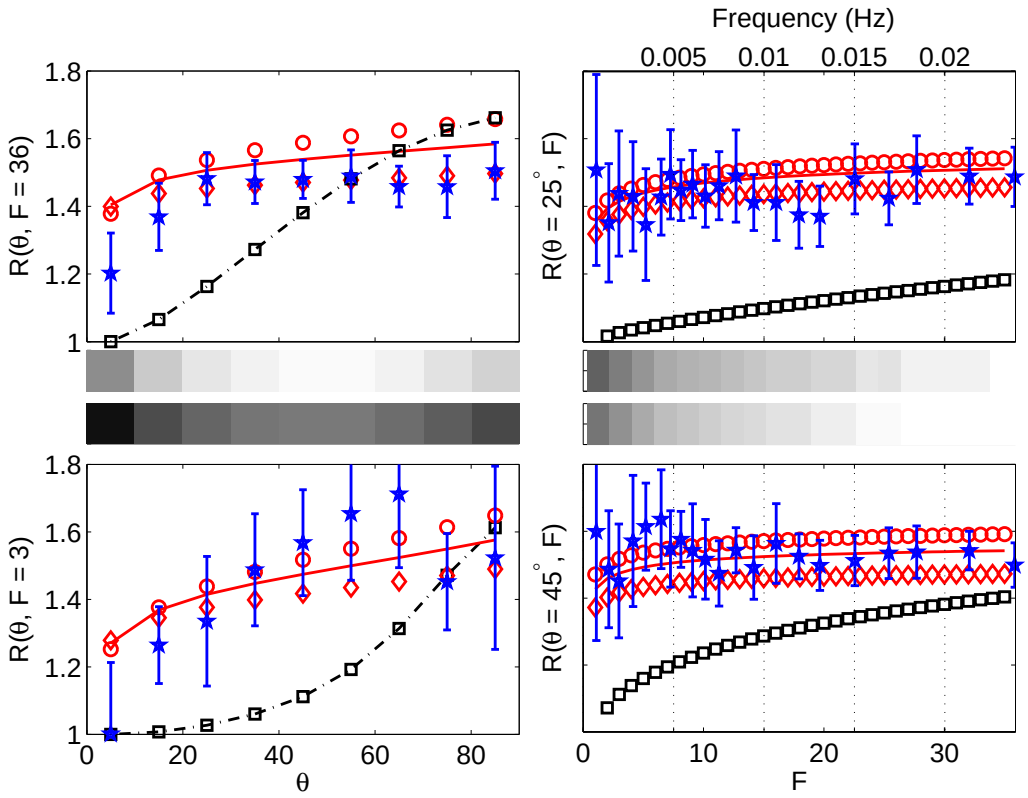

Figure 3.14: Left panels - θ dependence of the ratio $R(\theta, F)$ at two normalised frequencies: $F = 36$ (upper plot) and $F = 3$ (lower plot). Right panels – frequency dependence of the ratio $R(\theta, F)$ at $\theta = 25°$ (upper plot) and $\theta = 45°$ (lower plot). Observations are shown by blue stars, S2D model is in red with circles for Kolmogorov and diamonds for Iroshnikov-Kraichnan perpendicular scaling. A solid red line indicates the S2D model with the perpendicular scaling exponent from the data of $q_{2D} = 1.59$. All S2D models shown here use $q_s = 2$. The GS model is shown by black rectangles. Middle panels - Number of samples to form $\overline{R}$, where white = 1800 and black = 36 - this varies significantly with both frequency and angle.

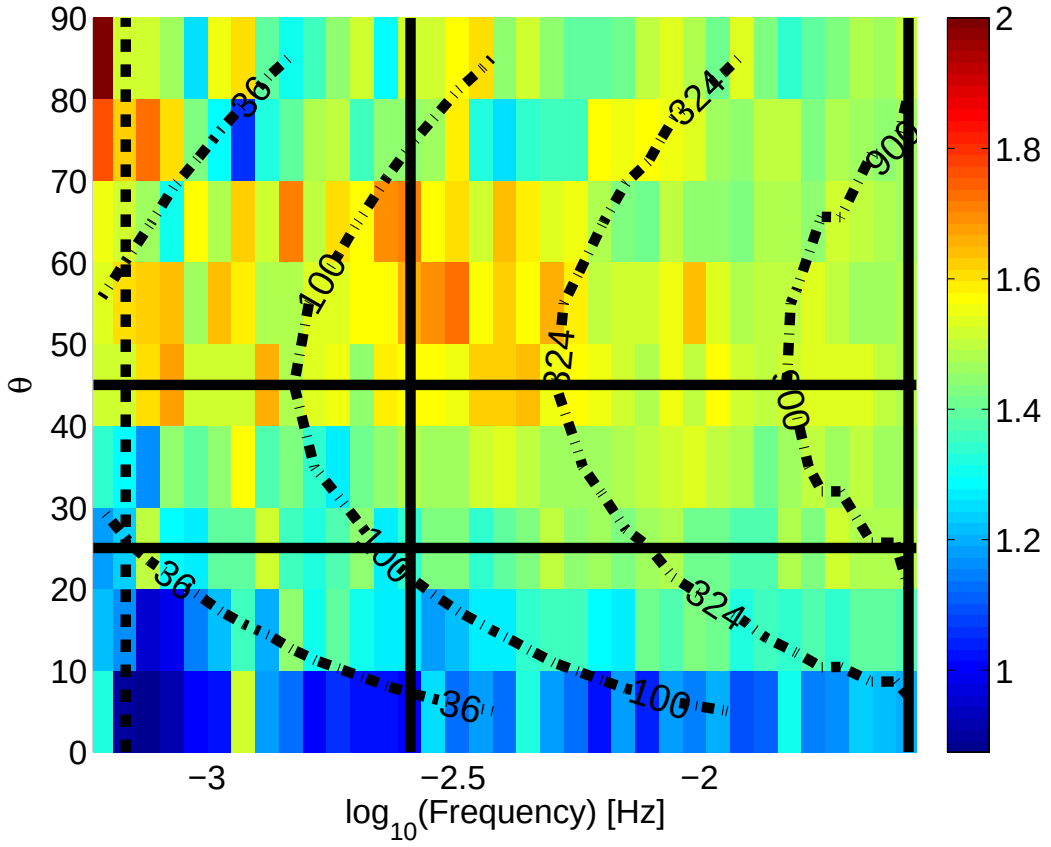

Figure 3.15: The surface $R(\theta, f)$ is shown in colour. The black solid lines indicate the cuts of $R(\theta, f)$ shown in Figure 3.14. The dashed line shows the start of the inertial range, F = 1. The dash-dot lines show contours of subinterval sample size. The colour bar shows the ratio $R(\theta, f) = \tilde{P}_{xx}(\theta, f)/\tilde{P}_{xx}(\theta, f)$

the satellite from 1.36 to 1.58 AU is not significant for our analysis. A long interval is necessary to obtain good statistical coverage across the sampling domain F, θ. In practice, the polar wind seen by Ulysses is stable and within 3° of the radial direction over the entire interval under study, so we replace $\hat{\mathbf{V}}$ by the radial unit vector $\mathbf{e}_R$ here, which corresponds to the coordinate system used by Belcher and Davis [1971].

For comparison between the models and the observations the data is normalized to $F = 1$ at the beginning of the inertial range, corresponding to a time-scale of 25 minutes. The ratio defined by equation (3.8) and a measure of the statistical variability for four specific cases of θ and F are indicated in Figure 3.14 by the blue stars.

The full surface $R(\theta, f)$ for our interval is shown in Figure 3.15. This shows

how the nonaxisymmetry between the perpendicular directions depends on the sampling domain. The surface is constructed by subdividing the entire interval into 1 day subintervals. $\tilde{P}_{xx}(t,f)/\tilde{P}_{yy}(t,f)$ is binned according to θ for each of these subinterval. As the distribution in each bin has a form close to log-normal the best measure of the subinterval average, $\overline{R}$, is the geometric mean Bieber et al. [1996]. In Figure 3.15 the contours indicate the number of samples in each $\overline{R}$, thus the contours may be interpreted as confidence contours. Each bin of the surface $R(\theta,f)$ has 55 realisations of $\overline{R}$. These realisations are used to calculate the statistical variability of the distribution $R(\theta,f)$ by calculating the median and interquartile range of the 55 values of $\overline{R}$. Figure 3.15 shows the median value for each bin and the stars in Figure 3.14 show the median value with statistical variability estimated to 99% certainty indicated by the error-bars.

The observations are reasonably matched by the two component heuristic model of S2D. We can also see that the GS model of turbulence fails to account for the observations. In the context of the S2D phenomenology the failing of the GS model is the lack of a significant $k_{\|}$ component, which has the physical motivation of propagating Alfvén waves. The method conducted here, where $R(F,\theta)$ is analyzed, highlights the strong 2D nature of the GS model.

For completeness it is possible to suggest two possible reasons for the lower than expected observed nonaxisymmetry in the kinetic range. One possible reason is an increase in compressibility, which corresponds to $\xi > 0$ in the formalization of the linear superposition model of section 3.4.1. Another possible reason is a dominant 2D wave vector geometry. A dominant 2D geometry produces a rapid reduction in the observed nonaxisymmetry as $\theta \to 0$, as seen for the GS model in the left panels of Fig. 3.14. The CLUSTER interval analyzed in Fig. 3.3 contains $\theta = 90^\circ \pm 30^\circ$. Therefore, the observed nonaxisymmetry in the kinetic range is likely to require a mixture of θ, ϕ, ξ to describe the observations completely within the linear model. This is a recommended extension for one interested in extending this analysis to the kinetic range, providing physical meaning is given to such combinations of θ, ϕ, ξ, however it is not clear *a priori* whether a unique solution is possible with the available number of free parameters.

3.6 Conclusions

In this chapter we have investigated the observed nonaxisymmetric power distribution in the perpendicular plane with respect to the local background magnetic field. The magnitude of nonaxisymmetry increases when observed in the kinetic range

compared to the inertial range. We conducted minimum variance analysis with Euler rotations to show conclusively that the bulk flow of the solar wind is correlated to the nonaxisymmetry. At first this may appear to imply that the fluctuations are ordered with respect to the bulk solar wind flow, and so the fluctuations are not frame invariant.

We constructed a simple linear model, composed by the superposition of transverse waves that represent Alfvén waves, and we used Taylor's hypothesis to sample two MHD direct numerical simulations. We also analytically modeled an axisymmetric energy distribution sampled via Taylor's hypothesis. It was found that an axisymmetric energy distribution sampled via Talyor's hypothesis is sufficient to reproduce the level of nonaxisymmetry observed in the solar wind. Importantly a direct relation between the magnitude of the nonaxisymmetry and the spectral exponent was found, which may explain the increased magnitude of the observed nonaxisymmetry in the kinetic range compared to the inertial range.

Finally, we extended the two-dimensional concept to three-dimensions in an attempt to investigate the wave vector anisotropy. We compared two models that are commonly used in the solar wind literature, that of Goldreich and Sridhar [1995] and "Slab+ 2D" [Bieber et al., 1996]. We found that the "Slab + 2D" model was able to reproduce the observations. However, the Goldreich and Sridhar [1995] model is unable to recover the observations, due to the strongly two-dimensional characteristics of the model. This work has demonstrated that the power spectral density alone is insufficient for testing models of turbulence and has provided another tool for discriminating between theories from observations.

Chapter 4

Discontinuities in the solar wind

The solar wind is thought to be a mixture of turbulence and structures, as suggested in Chapter 1. A key property of turbulence is the absence of a characteristic temporal/spatial scale within the inertial range. Therefore, for every spatial scale, k, there is an associated time-scales of evolution, τ_k. The time-scale is often referred to as the eddy turn-over time, such that $\tau_k \sim k^{-2/3}$ for K41 turbulence. The implication is that there is a finite amount of time required for a turbulence vector field to change direction, such that the gradient of change is constrained to $d\mathbf{u}/dk \sim k^{2/3}$ for K41 turbulence. Thus, an observed gradient greater than that expected by a specific turbulence theory may characterize a structure/discontinuity. In a system that may be described by ideal MHD there are different structures/discontinuities that may be supported, such as; contact discontinuities, tangential discontinuities, rotational discontinuities, shocks and pressure balance structures (e.g. see Kivelson and Russell [1995] and references within). Borovsky [2008] demonstrated that strong gradients in the magnetic field measurements coincide with a change in plasma properties such as flow velocity, density, pressure, temperature, etc. The aim of this chapter is to extract information relating to the turbulence, whilst excluding the time-series discontinuities. This will be done by analyzing *in-situ* observations of the solar wind prior and post application of a method to identify and remove the discontinuities.

To begin we demonstrate the characteristic features of a discontinuity/structure from observations. We plot the magnetic field observations for satellites 1 and 3 from the CLUSTER mission during the January 30th 2007 interval used in section 3.1. We have merged the FGM and STAFF-SC instruments to produce a time-series with a cadence of 450 Hz as in Chapter 3. The magnetic field from satellite 1 and 3 are shown by dotted and solid lines in Fig. 4.1, where the x, y and z component of the magnetic field are displayed in blue, green and red respectively. The vertical dashed

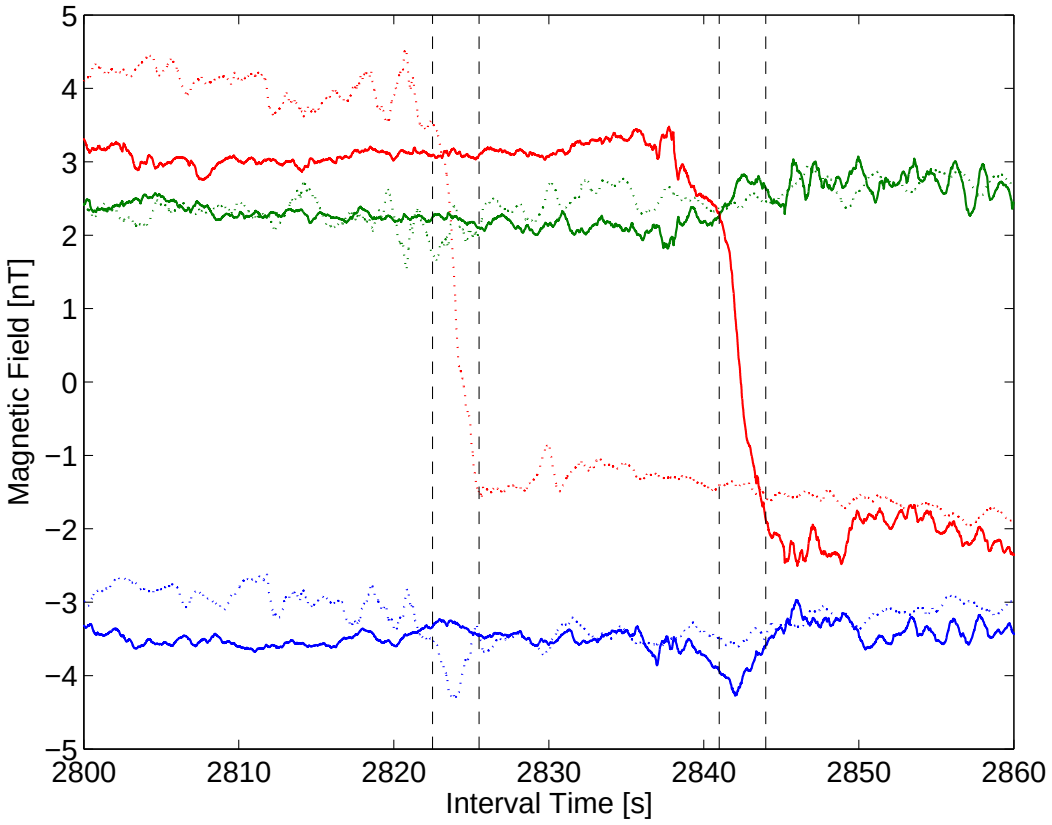

Figure 4.1: Magnetic field observations from satellite 1 and 3 of the CLUSTER mission during January 30th 2007 displayed with dotted and solid lines respectively. The x, y, z components are shown in blue, green and red respectively. The vertical dashed black line highlights a potential non-turbulent structure identified "by eye".

lines highlight the large gradients associated with a magnetic structure. Satellite 1 is ahead of satellite 3 by approximately 10000 km and the solar wind velocity is approximately 650 km/s, thus there is a delay of approximately 16 s between the two satellites due to advection.

The black vertical dashed lines are separated by 3 s, which corresponds approximately to inertial/kinetic transition scale. Thus, the black vertical dashed lines correspond to the smallest possible scale of the MHD turbulence. One can see the z component of satellite 1 undergoes a rapid change, which is advected by the solar wind flow and repeated in satellite 3. The highlighted feature is a candidate for a non-turbulent discontinuity due to the large gradient and stability of such a feature in the time-series.

In principle, it is possible to separate the population of fluctuations due to turbulence from those due to some other process. Methods developed to identify discontinuities include using: a minimum variance approach (Neugebauer et al. [1984]; Lepping and Behannon [1986]), identification of relatively large and fast changes in the plasma parameters/field direction (Tsurutani and Smith [1979]), the scaling of relatively large and fast changes in the field direction (Li [2008]) or a change in angle over a threshold value of the velocity and magnetic field direction at some pre-chosen scale (Borovsky [2008, 2010]; Zhdankin et al. [2012]) . However, these methods by construction introduce a characteristic scale and this is problematic in the study of scale-free phenomenology, such as turbulence. Any method to remove structures that is not also scale-free will impart a preferential scale on the remaining data and subsequent analysis.

The outline for the sections of this chapter is as follows; Section 4.2) Our new method for detecting discontinuities will be explained and we demonstrate a proof of concept for our method, Section 4.2.1) the background magnetic field will be discussed in detail as it is central to understanding this chapter, Section 4.3) our method is calibrated for the Ulysses data interval under investigation, Section 4.4) we introduce a surrogate dataset to demonstrate the effect of a discontinuous background magnetic field upon the PSD estimates. We determine a minimum estimate for the ratio of background field magnitude to root-mean-square fluctuations, which is important as a check on our method, Section 4.5) The results with/without discontinuities present in the analysis are presented for variance, power and intermitteny anisotropy.

4.1 Observations

We consider an extended interval of high latitude magnetic field observations recorded *in-situ* by Ulysses. We used an interval [day 91-146, 1995] of fast solar wind recorded at a heliographic latitude of 21° to 58° and a radial distance of 1.36 to 1.58 AU during solar minimum. The Ulysses interval has an average solar wind of 756 km/s and is recorded at a cadence of 1 s. To correct for data gaps and inhomogeneous sampling the data is linearly interpolated to a cadence of 2 s. Then for any period of missing data that lasts longer than 10 s the resulting region of interpolated data will be excluded from subsequent analysis.

4.2 Method Overview

We begin by introducing the null hypothesis we will be using to identify discontinuities within the *in-situ* observations. Our null hypothesis is that there exists a large-scale background magnetic field, where large refers to a spatial/temporal scale significantly larger than the inertial scales. The background magnetic field has a greater magnitude than the root-mean-square of the turbulent fluctuations. The background magnetic field is homogeneous or at least changes on a significantly longer time-scale than the turbulent fluctuations. Thus, we envisage a background magnetic field described by the predicted Parker spiral.

We separate the magnetic field observations into a slowly varying background field, $\mathbf{B}_0$, and fluctuations, $\Delta\mathbf{B}$, such that the magnetic field may be expressed as $\mathbf{B} = \mathbf{B}_0 + \Delta\mathbf{B}$, as in Chapter 2. Therefore, we write the magnitude at every time as $B^2 = \left(B_0 + \Delta B_\parallel\right)^2 + \Delta B_\perp^2$, where $\Delta B_{\perp,\parallel}$ are the turbulent fluctuations at a specific time in the perpendicular and parallel direction with respect to the background magnetic field. Taylor expansion leads to $|\mathbf{B}| = B_0\left[1 + \Delta B_\parallel/B_0 + \mathcal{O}\left(\Delta B_\perp^2/2B_0^2\right)\right]$. We consider two points separated by a time-scale, τ, such that

$$\delta|\mathbf{B}|(\tau) \equiv |\mathbf{B}_t| - |\mathbf{B}_{t+\tau}| \sim B_{0,t} + \Delta B_{\parallel,t} - B_{0,t+\tau} - \Delta B_{\parallel,t+\tau}. \tag{4.1}$$

Note, $\delta B_\parallel(t,\tau) = \Delta B_{\parallel,t} - \Delta B_{\parallel,t+\tau}$, where all quantities are distributions and only the measured fluctuation, $\delta B_\parallel(\tau)$, is explicitly a function of τ.

Providing there is no discontinuity within the time-scale τ, such that within the inertial range scales $B_{0,t} = B_{0,t+\tau}$, one arrives at the relation $\delta|\mathbf{B}| \sim \delta B_\parallel$. Under the null hypothesis this relation is always true. Therefore, we set our geometric condition as, $|\delta|\mathbf{B}\,(t,\tau)\,| - \delta B_\parallel\,(t,\tau)\,| < T\,(\tau)$, where $T\,(\tau)$ is a scale-dependent threshold to be found from the data that accounts for the approximations used to

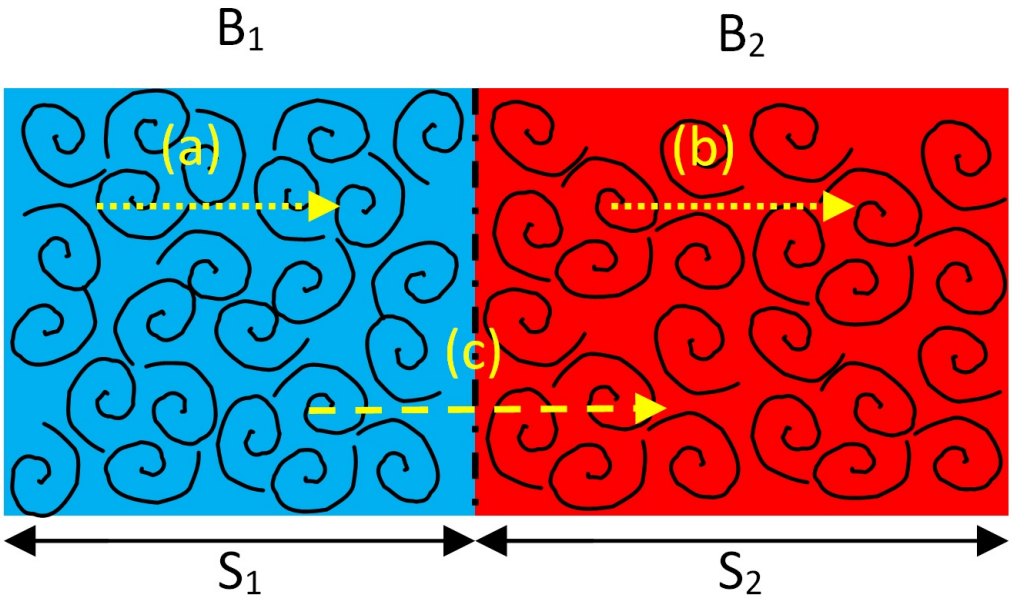

Figure 4.2: Schematic of two distinct background magnetic fields joined to produce a rapid time-series discontinuity. The magnetic field of $\mathbf{B}_1$ and $\mathbf{B}_2$, shown in blue and red respectively, have a domain sufficiently large to develop turbulence, i.e. $S_{1,2} \gg L$. The discontinuity is highlighted by the vertical dot-dashed black line. Sample paths (a) and (b) do not cross the discontinuity, whereas sample path (c) does.

arrive at $\delta|\mathbf{B}| \sim \delta B_{\parallel}$.

Our method is calculated scale-by-scale, such that it is expected that we will use a local background magnetic field and wavelet decomposition, as in Chapter 3. The rational for our choice of background magnetic field estimate is discussed in Section 4.2.1. Therefore, we express our criteria in Fourier space, $|\delta|\mathbf{B}\,(t,f)\,| - \delta B_{\parallel}\,(t,f)\,| < \tilde{T}\,(f)$. Thus our criteria for a discontinuity free time index at a specific frequency is:

$$|\delta|\mathbf{B}\,(t,f)\,| - \delta B_{\parallel}\,(t,f)\,| < \tilde{T}\,(f) = T_0 f^{-\beta}, \tag{4.2}$$

which is assessed independently for all scales/frequencies and at every time index. Here β represents how the threshold changes with scale/frequency and T_0 is a constant. We will determine both β and T_0 from the data. Finding β and T_0 will be covered in Section 4.3. Importantly, the threshold $T_0 f^{-\beta}$ is scale/frequency-dependent. It is not a constant threshold for all scales/frequencies, which corresponds to the case where $\beta = 0$. We will refer to a case as filtered where the fluctuations from times were the criteria of equation 4.2 is not realized are removed.

In order to visualize the scenario and how our method is able to detect

discontinuities within the time-series, we display a schematic of the situation in Fig. 4.2. In our schematic $\mathbf{B}_1$ and $\mathbf{B}_2$, shown in blue and red respectively, denote two distinct large-scale background magnetic fields, such that $S_{1,2} \gg L$, where L is the largest scale of the turbulent fluctuations. There is a discontinuity between S_1 and S_2 comparable to the ion gyro-scale. Thus, our schematic has qualitative similarities with the observations shown in Fig. 4.1. Using our method it is expected that the time-series from the dotted yellow sample paths (a) and (b) will pass our threshold, whereas the time-series from the yellow dashed sample path (c) will fail our threshold in the region of the discontinuity. The region containing reject data will increase with scale, as it is important to exclude any fluctuations that span the discontinuity, and so contain information about the discontinuity. Note also the local background magnetic field is not defined within a discontinuity.

Finally, as a proof of concept we measure the "discontinuity detection quantity", $|\delta|B| - \delta B_{\parallel}|$, as a function of time for three separate temporal-scales. In Fig. 4.3 we display the observations of satellite 1 for the same discontinuity as shown in Fig. 4.1. The observations are shown in magenta and the vertical black dashed lines mark the discontinuity as measured "by eye" in Fig. 4.1. Three temporal scales of approximately 3.5, 9.8, 27.3 s are displayed in blue, green and red respectively. The vertical dot-dashed lines correspond to the temporal uncertainty due to the Morlet wavelet, which is approximately $\pm 8\tau/5$.

One can see that the prescribed detection quantity, $|\delta|B| - \delta B_{\parallel}|$, increases in the vicinity of a discontinuity and that the value increases as the scale increases. Thus, the discontinuity detection quantity behaves as we would anticipate from the above discussion. The observations are consistent with the method expectations. The next step is to determine the correct threshold for the data. This will be covered in Section 4.2.1. However, we will first discuss the definition of the background field, which is fundamental to the method and understanding the detection method introduced in this chapter.

4.2.1 Background Magnetic Field

Currently there are two methods used to determine the background magnetic field. These are referred to as the "global" and "local" background magnetic field. However, the background magnetic field is not a trivial quantity, as we will see the method used to determine the background magnetic field may fundamentally affect the results.

The global background magnetic field is defined on a temporal scale sufficiently large, such that the "weak" stationarity criteria is achieved. Weak sta-

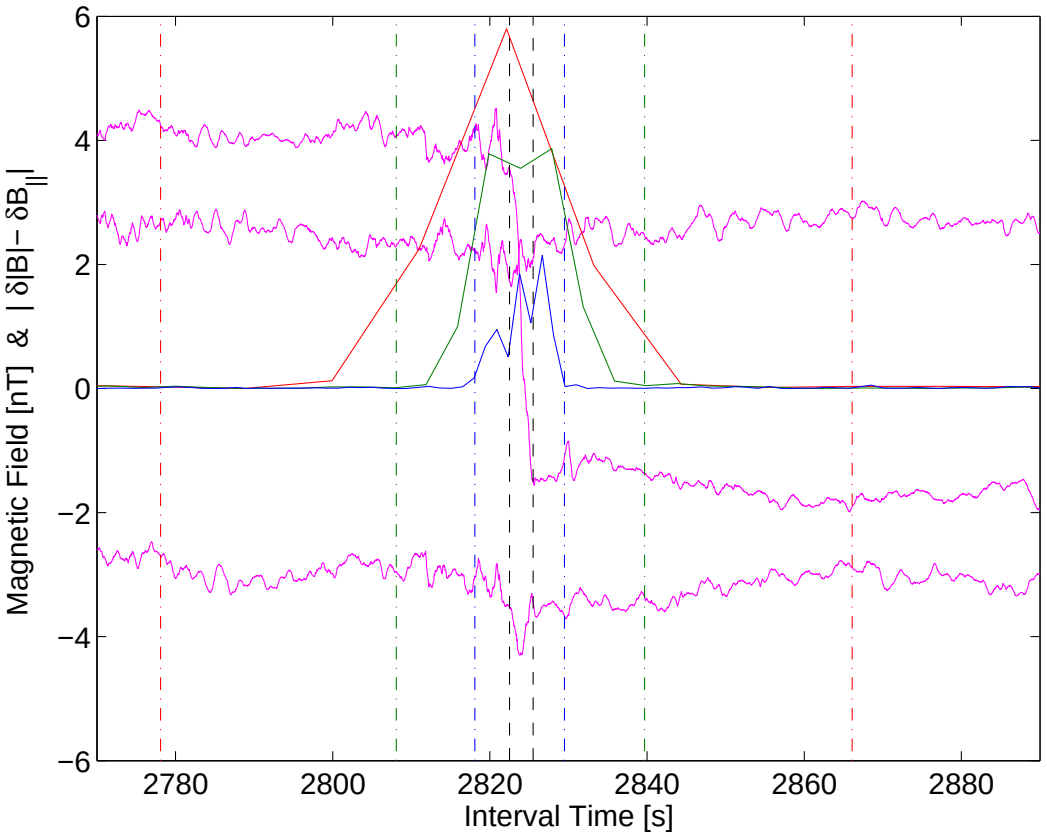

Figure 4.3: Behaviour of the "discontinuity detection quantity", $|\delta|B| - \delta B_{\|}|$. Observations from satellite 1 (same as shown in Fig. 4.1) are shown in magenta, where the vertical dashed black lines highlight the same discontinuity identified "by eye". The quantity $|\delta|B| - \delta B_{\|}|$ is shown as a function of time for 3.5, 9.8 and 27.3 seconds in blue, green and red respectively. The temporal uncertainty for each time-scale is shown by vertical dot-dashed lines.

tionarity implies that one may subtract the background magnetic field from the observations to produce the fluctuations, such that $\mathbf{B}(t) - \langle \mathbf{B} \rangle_T = \Delta \mathbf{B}$, and that the fluctuation distribution is time-stationary for the first and second moment. Under this formalization the background magnetic field for any individual analysis is defined at one temporal-scale, T, for which weak stationarity is realized. Typically T is of the order of hours/days. This method assumes that the background magnetic field is homogeneous superposed with a random process (Tu and Marsch [1995]), such that there are no discontinuities within the averaging period used to calculate the background field (Bavassano et al. [1982]). The global background field estimate requires carefully chosen start and finish points for the averaging interval. Matthaeus et al. [1986] showed that if the end points of the interval are shifted across a sector boundary (a sector boundary is essentially a strong discontinuity within a time-series) the analysis will undergo unacceptable changes. There is also concern that averaging over long periods in order to produce a good statistical convergence of the background field estimate may cause cancellation of structure that will misrepresent the resulting analysis (Tu and Marsch [1995]).

The local background magnetic field is calculated for all points in the time-series and all temporal/frequency scales of interest. The rationale for the introduction of the local background field is that the fluctuations of the magnetic field are influenced by the magnetic field that results from all scales greater than that of the fluctuation scale/frequency of interest. The background magnetic field felt by the fluctuations is the volume average $\mathbf{b}_r(\mathbf{s}) = 1/V_r \int_{V_r} \mathbf{B}(\mathbf{s}) d\mathbf{s}$, however the estimated background field using Taylor hypothesis is $\mathbf{b}_\tau(t) = 1/T \int_T \mathbf{B}(t) dt$. If the background field is inhomogeneous these two quantities are generally not equal. However, there may be temporal/spatial scales where the background field can be considered homogeneous, i.e. regions between structures/discontinuities. Thus, the local background field may be used to estimate the physical background field if estimates are not made in the vicinity of structures/discontinuities of the physical background field.

The local and global background magnetic fields coincide at approximately the temporal-scale, T. However, for scales of increasing frequency there are significant differences. For temporal-scales smaller than T the local background magnetic field method increases the observed anisotropy, compared to the global background field. Interestingly, if a surrogate dataset set is produced by randomizing the phase the enhancement of anisotropy is removed (Matthaeus et al. [2012]), implying that phase coherent structures, which includes time-series discontinuities, affect anisotropy estimates when using the local background field estimate.

Thus, the considerations investigated for the global background magnetic field, such as cancellation of structure and averaging end-points, are important for the local magnetic field. The potential differences for the local field estimate are; a) it is conducted over a smaller sample ensemble, and so may be more sensitive to discontinuities b) there is an introduction of scale-dependent structure cancellation under the operation of averaging, such that uncertainty of the background magnetic field becomes dependent upon the temporal-scale under investigation.

Therefore, the question as to which method to use for our method needs to be addressed. Consider magnetic field observations of the form, $\mathbf{B} = \mathbf{B}_0 + \mathbf{\Delta B}$, as defined above. We conduct an average at a specific temporal scale, such that $\mathbf{b}(t,\tau) = \langle \mathbf{B}_0 \rangle_\tau + \langle \delta \mathbf{B} \rangle_\tau$, where $\mathbf{b}(t,\tau)$ is the local background magnetic field estimate. We assume the distribution of $\mathbf{\Delta B}$ values is approximately symmetric. Thus, the mean of the fluctuations tends to zero as the ensemble increases in size, so if the background field is homogeneous then the estimated background field, $\mathbf{b}$, tends to the background field, $\mathbf{B_0}$. However, if the background field, $\mathbf{B_0}$, is inhomogeneous, containing strong deviations in direction, a greater ensemble size does not increase the accuracy of $\mathbf{b}$.

We have produced a surrogate background magnetic field that is inhomogeneous, in that there are sudden discontinuities present. The purpose of the surrogate time-series is to demonstrate the uncertainty that arises in estimating the background magnetic field with the two existing method (i.e. the "local" and "global" temporal average) in the presence of time-series discontinuities. Details of the surrogate dataset will be covered in detail in section 4.4. The time-series is generated at a cadence of 0.25 Hz, such that the discontinuity profile does not require modeling. The top panel of Fig. 4.4 displays a single component of the surrogate time-series in blue. Only part of the generated interval and a single component are shown for clarity. We consider a global background field averaged over the entire interval, which corresponds to approximately 5 days in green and the local background magnetic field at temporal-scales of approximately 2:46, 9:36 and 33:15 minute:seconds in red, black and magenta respectively. The bottom panel shows the angle in degrees between the constructed background field and the estimated background field.

The local background field becomes a less accurate estimate of the actual background field as the temporal scale increases. One can see that any window over which the background magnetic field is calculated by an averaging operation contains a significant deviation from the true background magnetic field, $\mathbf{B_0}$, for all times if the window contains more than on discontinuity. Thus, concerns of structure cancellation by an averaging operation are valid and are not unique to

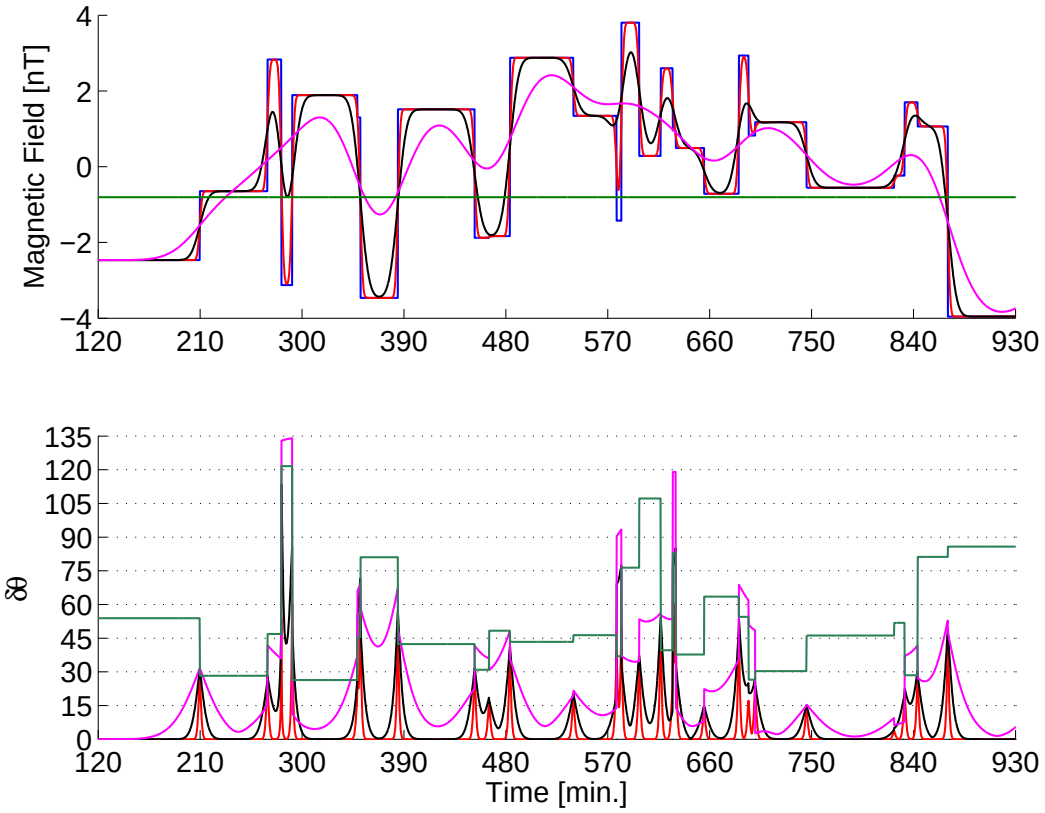

Figure 4.4: Top panel: One component of a surrogate dataset that represents a discontinuous background magnetic field is shown in blue. Bottom panel: The angle between the estimated background field and actual background field, $\cos^{-1}(\mathbf{b}\cdot\mathbf{B}_0)$, for different estimates. Both panels: The local background estimate method used at 2:46, 9:36, 33:25 minutes:seconds are displayed in red, black and magenta respectively. The global background field, where $G \sim 5$ days, is shown in green.

either method.

For our method we choose to use the local background magnetic field estimate. Our method uses equation 4.2 to compare two independent estimates of $\delta B_{\parallel}$, i.e. $\delta|\mathbf{B}|$ and $\mathbf{b}\cdot\delta\mathbf{B}$. For times where the two estimates are significantly different the local background magnetic field is poorly defined due to a discontinuity/structure. The data around times were discontinuities are detected by the above criteria are removed from subsequent analysis. Therefore, for the first time, we will be able to accurately estimate the background magnetic field for all data analyzed. Thus, we may determine the anisotropy of the turbulence within the solar wind.

4.3 Quantifying β and T_0

Now that we have established the method that will be used to determine the background magnetic field estimate it is possible to find both β and T_0 from the data. It is suggested from equation 4.1 that the power of the parallel component with respect to the background field, $P_{\parallel}$, and the modulus of the magnetic field fluctuations, $P_{|\mathbf{B}|}$, are approximately equal in the absence of discontinuities. Therefore, we systematically vary the values of T_0 and β with the aim to achieve the lowest root-mean-square-deviation (rmsd) between $P_{|\mathbf{B}|}$ and $P_{\parallel}$. The lowest rmsd is found by removing fluctuations from the $\delta B_{\parallel}$ population according to equation 4.2 and leaving the $\delta|\mathbf{B}|$ population unchanged. We chose to remove fluctuations from the $\delta B_{\parallel}$ population because $\delta B_{\parallel}$ is explicitly dependent upon the background magnetic field estimate. Therefore, we assume that the effect of discontinuities on the magnetic field magnitude for inertial range scales is marginal, which is consistent with the findings of Coleman [1968].

Here we estimate the values of T_0 and β by calculating the rmsd across 9 logarithmically spaced frequencies within the inertial range, which correspond to approximately $1 \rightarrow 10$ minutes. We explore the variable space of equation (4.2) for $T_0 = 10^{[-2.75,-0.25]}$ and $\beta = [0.25, 0.95]$. Hereon, for clarity we will refer to the value of T_0 by the logarithmic power only. A map displaying log_{10}(rmsd) is shown in Fig. 4.5. A unique solution for minimising the rmsd of $P_{|\mathbf{B}|}$ and $P_{\parallel}$ can be seen towards the centre of the figure. The bottom left of the figure shows a dark triangle as these values of T_0 and β remove the $\delta B_{\parallel}$ fluctuation population entirely for the larges temporal-scale. Thus, there is no data to construct $P_{\parallel}$ at the largest temporal-scale of approximately 10 minutes, and so the rmsd may not be calculated due to an uneven number of points to compare between $P_{\parallel}$ and $P_{|\mathbf{B}|}$.

In this chapter we consider four different combinations of $[\beta, T_0]$. We will

use the raw data, which may be expressed as $[0.95, -0.25]$ and the optimum case, which for this data set is found to be $[0.63, -1.51]$. For the other two cases either T_0 or β remain at the optimum value and the other is varied, such that the two cases have approximately the same degree of rmsd, i.e. they are on a contour of constant rmsd. These values of $[\beta, T_0]$ are $[0.71, -1.51]$ and $[0.63, -1.70]$. All four cases have been highlighted by a specific colour and letter on Fig. 4.5 that will be used to refer to the cases throughout the paper. These are I, II, III, IV displayed in black, blue, magenta and red respectively.

A novel and distinctive feature of our method is that the threshold changes with wavelet scale as specified by the exponent β. Therefore, it is important to check that the range of β values found by conducting a rmsd test are reasonable. We may estimate the value of β that would be expected if the first two central moments of the $\delta|\mathbf{B}|$ and $\delta B_{\parallel}$ populations may be approximated to be Gaussian. First we estimate how the standard deviation of the $\delta|\mathbf{B}|$ and $\delta B_{\parallel}$ populations scale with frequency. This may be estimated from the spectral exponent of these two quantities (See Section 4.5 for the spectral exponents). We estimate the spectral exponents to be $\gamma_{|\mathbf{B}|} = 1.4$ and $\gamma_{\parallel} = 1.8$ for the $\delta|\mathbf{B}|$ and $\delta B_{\parallel}$ populations respectively. Therefore, the standard deviation of the probability distributions scale as $\sigma^2_{|B|} \sim 0.4$ and $\sigma^2_{\parallel} \sim 0.8$. The standard deviation of $Z = \delta|\mathbf{B}| - \delta B_{\parallel}$ is $\sqrt{(\sigma^2_{|B|} + \sigma^2_{\parallel})}$, as it is the convolution of two Gaussian distributed probabilities. However, the threshold used depends on $\mathcal{P}(|Z|)$. The standard deviation of this probability distribution may be expressed as $\sqrt{(\sigma^2_{|B|} + \sigma^2_{\parallel})(1 - (2/\pi))}$. If we assume that the $\sigma^2_{\parallel,|B|}$ are known to an accuracy of ± 0.1 then we may expect the optimum range to be $\beta = 0.60 \rightarrow 0.71$. Comparing this estimated range of β with the optimum range displayed in Fig. 4.5 we can see reasonable agreement.

4.4 Criterion Check

4.4.1 Surrogate Data

The solar wind contains the signature of many distinct physical processes. The goal is to remove only those fluctuations that are not due to the underlying turbulence in the inertial range. Coherent structures such as shocks and flux tube boundaries will produce a rapid temporal variation (discontinuity) in the background field as seen by a satellite *in-situ*. It is these features that our method will remove. Therefore, we construct a surrogate dataset that represents a discontinuous background magnetic field.

Our surrogate dataset for the fast solar wind as seen by Ulysses contains a

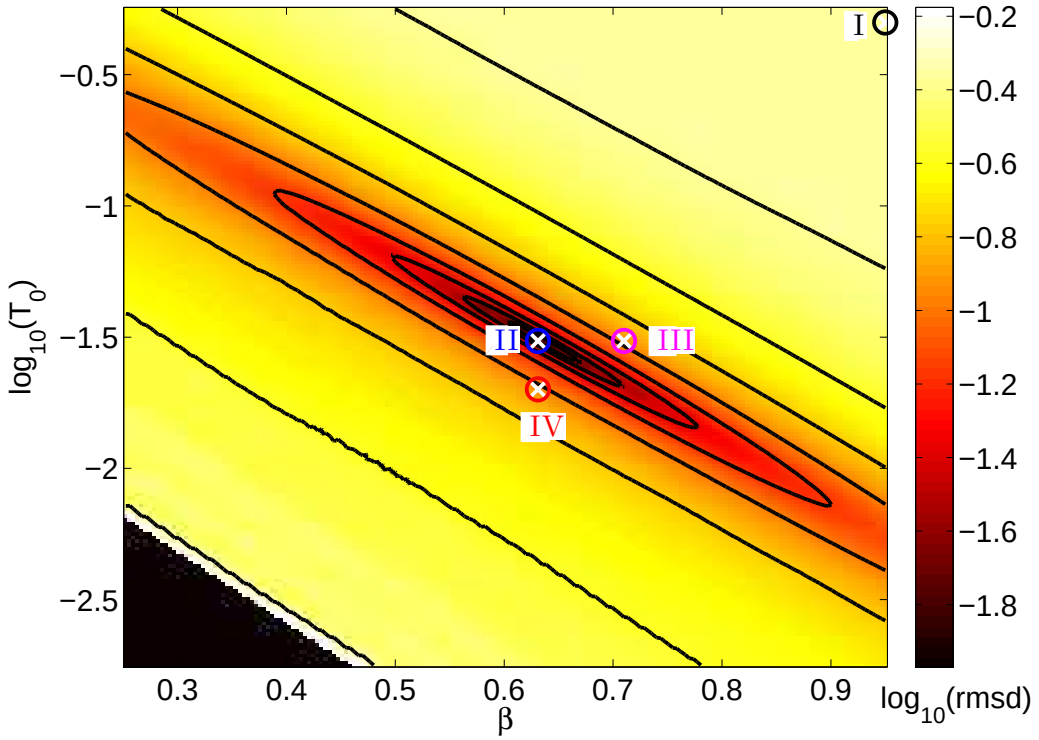

Figure 4.5: Intensity map in the range of 1 to 10 minutes of the root-mean-square-deviation between the power of the modulus of the magnetic field and the parallel component of the fluctuations with respect to the local background field under varies values of filtering defined by equation 4.2. The dark area corresponding to small β and T_0 contains no value as the largest time-scale point has been removed for the parallel component due to the threshold. The raw (I), optimum filtered (II), under-filtered (III) and over-filtered (IV) cases are show in black, blue, magenta and red with values of $[\beta, log_{10}(T_0)]$ of $[0.95, -0.25]$, $[0.63, -1.51]$, $[0.71, -1.51]$ and $[0.63, -1.70]$ respectively.

waiting-time distribution and preserves the angular probability distribution for the magnetic field vector. The surrogate dataset is composed of uncorrelated fluctuations to represent a set of uncorrelated discontinuities. The PSD of the surrogate dataset may be interpreted as a "noise floor" for all scales of the PSD, below which ensembles will be dominated by fluctuations related to temporal discontinuities of the background magnetic field direction. We will show this surrogate time series may be used to estimate the free parameters in equation (4.2) that determine the threshold for our method, although less precise than the rmsd method previously used. We will also use it to demonstrate the effect of discontinuities on statistical estimates.

There has been considerable work on the waiting-time distribution of discontinuities. There is a range of reported waiting time distributions, such as exponential (Burlaga [1969]), power-law (Bruno and Carbone [2005]) and lognormal (Vasquez et al. [2007]). We will demonstrate the effect of using an exponential and stretched-exponential waiting-time distribution on the observed PSD. The exponential waiting-time has the advantage that there is only one free parameter, that of the waiting-time mean. The stretched-exponential waiting time is considered here as it is possible to approximate the exponential, power-law and lognormal with a stretched exponential distribution depending on the scales used to determine the distribution.

Conventionally a surrogate dataset set would be made by preserving the Fourier amplitudes and randomising the phases (Schreiber and Schmitz [2000]). The use of such surrogate dataset methods suggests the importance of phase correlations on anisotropy measures (e.g. Matthaeus et al. [2012]). Here, our data, which is designed to reproduce the non-turbulent discontinuities, is constructed as a Markovian jump process, where the angular state space of the original data is preserved.

The Ulysses data is in **RTN** coordinates, where **R** is the radial direction from the Sun to the spacecraft, **T** is the direction perpendicular to the axis of rotation of the Sun and perpendicular to **R**. **N** competes the orthogonal set and is directed perpendicular to the ecliptic plane. Thus, the magnetic field data is in the form $\mathbf{B}_t = [B_R(t), B_T(t), B_N(t)]$. From this coordinate system we project to a spherical coordinate system, $\mathbf{B}_t = [|B|_t, \theta_t, \phi_t]$, such that θ is the angle in the **RT** plane and taken w.r.t **R**, and ϕ is the angle from the **RT** plane. In this coordinate system we define the joint probability density $P_{\theta,\phi}$, which is the probability of a jump pointing in a certain direction of θ-ϕ-space.

The waiting time between jumps, T_W, is drawn from a probability distri-

bution. The exponential distribution is described as $T_W \sim \lambda \exp(t/\lambda)$, whilst the stretched-exponential distribution is described by $T_W(t|\lambda, b) = \frac{b}{\lambda}(\frac{t}{\lambda})^{b-1} \exp(-(\frac{t}{\lambda})^b)$, where the $1/\lambda$ is the jump rate and b is a stretching factor. Both distributions are discretized and we allow only values that are greater than 20 s.

The value of our surrogate dataset at a specific time index, X_t, is constant within each waiting time, after which a jump occurs by selecting $\mathbf{B}_j$ from the observations, where j is a randomly selected index of the observations. The index, j, effectively randomises the correlation between successive discontinuities. Our surrogate may be written as

$$X_t = \begin{cases} [M_0, \theta\left(x'_1\right), \phi\left(x'_1\right)], & \text{if } t = 0 \\ X_{t-1}, & \text{if } t > 0 \text{ and } t - s < T_W \\ [M_0, \theta\left(x'_j\right), \phi\left(x'_j\right)], & \text{if } t > 0 \text{ and } t - s = T_W \end{cases} \tag{4.3}$$

where t is the time of the surrogate dataset, s is the time of the latest jump in the time-series, $\theta\left(x'_j\right)$ and $\phi\left(x'_j\right)$ are subsets from the same time index of the observations. M_0 is the constant magnitude of the vector, chosen such that there is agreement between the PSD of the observations and the surrogate date in the range $\tau = 1 - 7$ days when the surrogate has been projected back to **RTN** coordinates.

We display the PSD for the R-component of the observations and surrogate time-series with two different waiting-time distributions. Using the Welsh spectral estimate method we demonstrate the larger scales in Fig. 4.6 and smaller scales in Fig. 4.7. The spread in the PSD at high frequencies may be used as a proxy for the uncertainty across all scales. The Ulysses observations are displayed in blue, whilst the exponential and stretched-exponential waiting-distributions are shown in red and black respectively. For the exponential case there are two distinct behaviors with a rapid transition. This is shown by the small scale spectral index of f^{-2}, indicative of discontinuities, and a large scale spectral index of f^{-0}, indicative of uncorrelated fluctuations.

The two scaling behaviours can be understood by examining the behaviour of the mean, variance and correlation function of the surrogate dataset. It can be shown that all three of these quantities, which are important for weak time stationarity, tend to the stationary solution at a rate $\sim \exp(-\tau/\lambda)$ for the exponential waiting-time distribution (Gardiner [2003]; Jacobs [2010]). Therefore, the PSD is dominated by the apparent non-time-stationary nature of small ensembles until τ is approximately $1 - 2\lambda$, then there is a transition from f^{-2} to f^0 determined by the waiting-time distribution. Above approximately $5 - 10\lambda$ the ensembles become

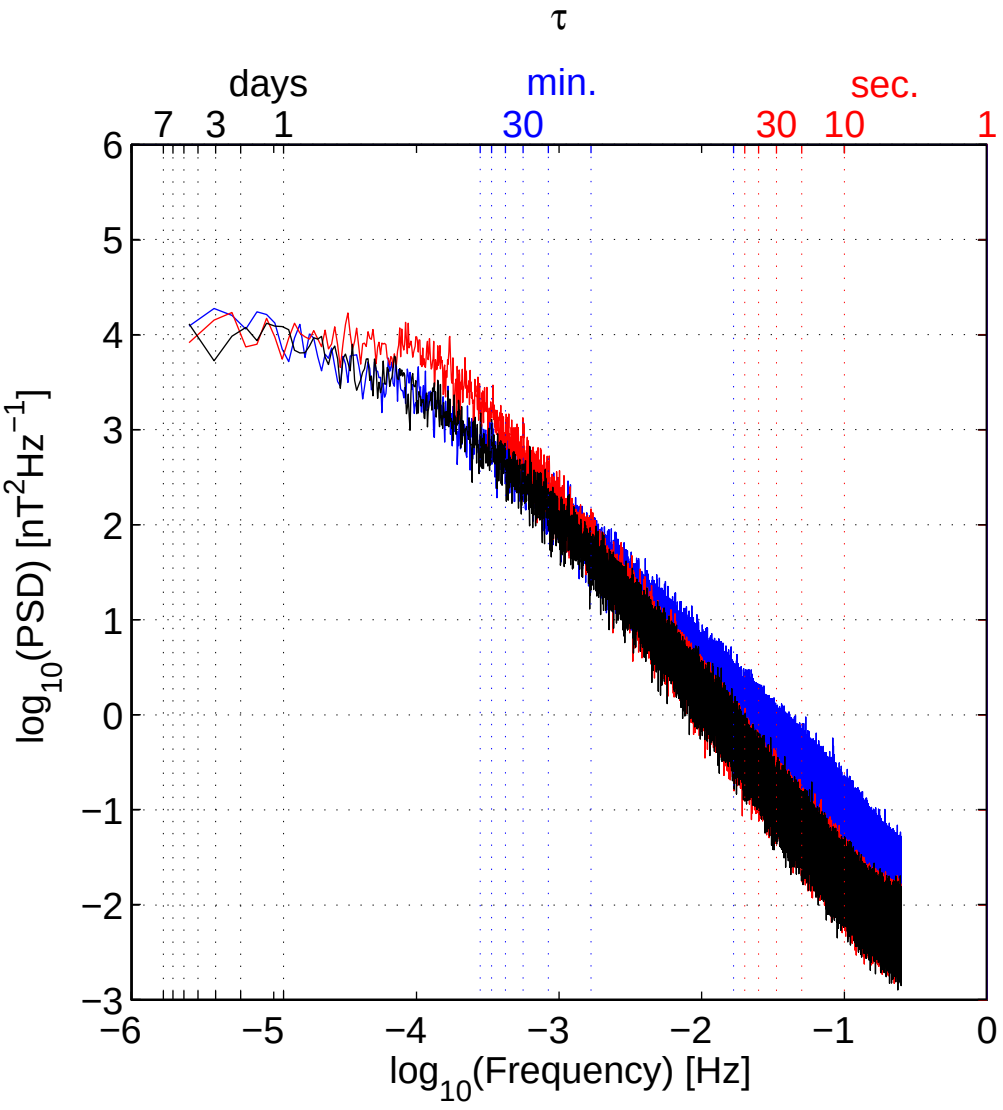

Figure 4.6: PSD for the Ulysses in blue. The surrogate dataset for a discontinuous background magnetic field where the waiting-time follows an exponential and stretched exponential distribution are shown in red and black.

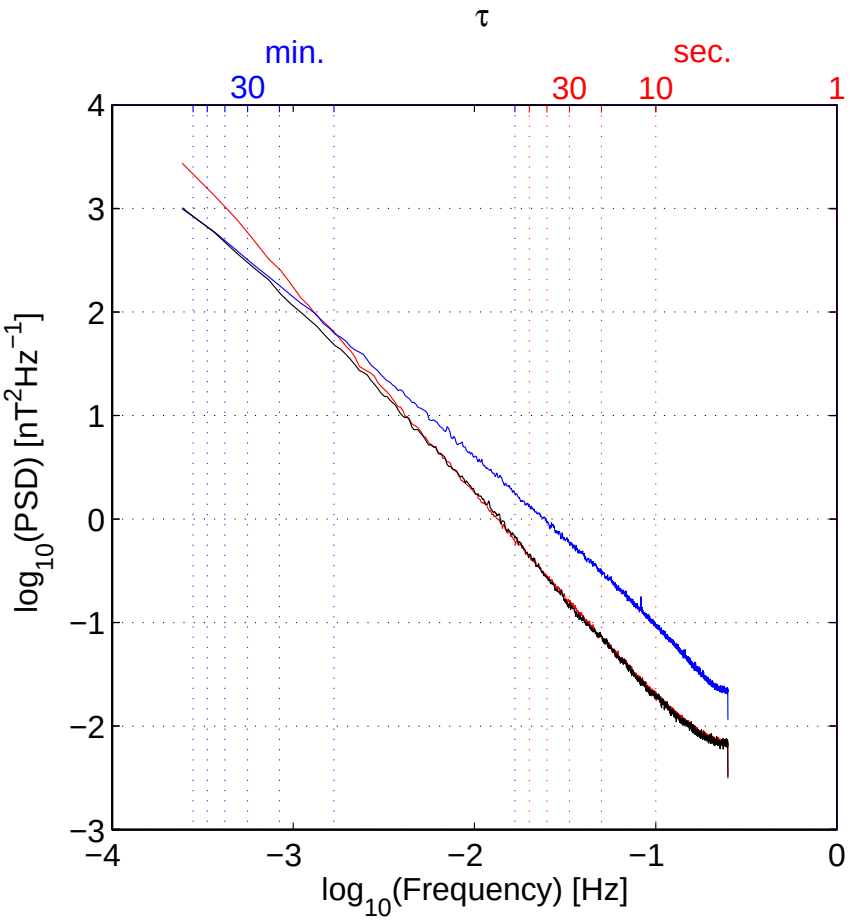

Figure 4.7: PSD for Ulysses data is shown in blue. The surrogate dataset for a discontinuous background magnetic field where the waiting-time follows an exponential and stretched exponential distribution are shown in red and black. Unlike Fig. 4.6 the Welch method is conducted with a smaller window to increase the accuracy of the PSD estimate within the inertial range scales.

approximately time stationary. The stretched exponential waiting-time distribution must show the same small and large scale behaviour. Importantly, like the observations the stretched exponential distribution is able to demonstrate a piece-wise transition region that resembles f^{-1}.

Therefore, we find three distinct regions of the PSD of our surrogate dataset, shown in Fig. 4.12, and so the PSD we would observe if the solar wind fluctuations were entirely discontinuities with an exponential or stretched-exponential waiting time distribution. In order to construct a time-series the waiting-time distributions are discreteized by rounding to the nearest integer. We chose to enforce a minimum jump time of 10 Δt and the time-series is constructed at a cadence of $\Delta t = 2$ s for both the exponential and stretched exponential distributions. For the exponential and stretched-exponential waiting-time distributions the average time between discontinuities is 20 and 13 minutes respectively. This is achieved by using a $\lambda = 20$ minutes for the exponential case and $\lambda = 75$ s, $b = 0.4$ for the stretched-exponential case. It should be noted that the solar wind has been observed to become weakly time stationary on times of 5-10 λ [Matthaeus and Goldstein, 1982] and temporal scales greater than 1 hour. This result is consistent with both waiting-time distributions used here.

The difference between the surrogate and Ulysses PSD in this range shows the power that arises from correlated fluctuations, such as turbulence. This highlights the importance of removing time-series discontinuities from further statistical measures that have the sole intention of understanding turbulence and the importance of understanding the waiting-time distribution between discontinuities.

4.4.2 Comparison with previous methods

A previously used measure to characterise discontinuities is the change of angle between two magnetic field vectors in the time-series separated by a time-scale, τ, such that $\Delta\theta\left(\tau\right) = \cos^{-1}\left(\frac{\mathbf{B}(t)\cdot\mathbf{B}(t+\tau)}{|\mathbf{B}(t)||\mathbf{B}(t+\tau)|}\right)$. This measure has been used previously in the detection of discontinuities (e.g. Borovsky [2008]; Li [2008]; Borovsky [2010]; Zhdankin et al. [2012]). It is anticipated that for small τ small values of $\Delta\theta$ will contain predominantly turbulent fluctuations, whereas the large $\Delta\theta$ will be populated exclusively by discontinuities. We will therefore use our surrogate dataset to find the distribution of discontinuities in this $\Delta\theta$ mapping for all scales of interest, and then use this distribution to separate fluctuations affected by discontinuities from the underlying turbulent distribution. The $\Delta\theta$ mapping of our surrogate time-series will provide another estimate of the values of T_0 and β that can be used.

In order to estimate a valid range of values for both T_0 and β the probability

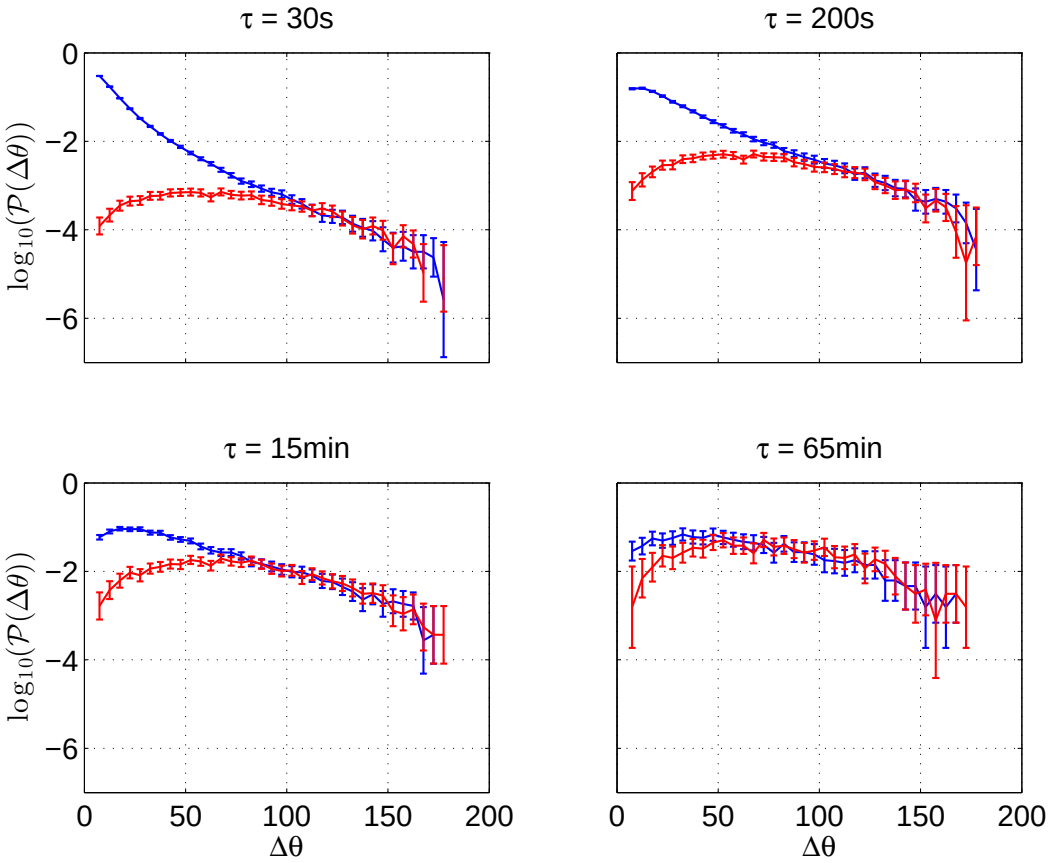

Figure 4.8: The probability distribution estimate at four different time-scales for the change in angle between magnetic field vectors in the time-series, $\Delta\theta$, as observed in the solar wind and the surrogate jump process with exponential waiting-time distribution in blue and red respectively.

distribution function of $\Delta\theta$, $\mathcal{P}(\Delta\theta)$, for different values of τ must be constructed from the raw Ulysses interval and surrogate time series. For this section we consider the exponential waiting-time surrogate time-series as there is only one free parameter, which is the outer-scale of the inertial range. In Fig. 4.8 the distribution of $\mathcal{P}(\Delta\theta)$ for the raw Ulysses interval and surrogate time-series can be seen in blue and red respectively. For sufficiently large τ, such that the $\tau > 3\lambda$, the raw Ulysses interval and the surrogate time series coincide for all $\Delta\theta$, agreement is also seen when $\Delta\theta > 100^\circ$ for all τ. The agreement between the surrogate time-series and the raw Ulysses interval demonstrates that these observations may be solely attributed to discontinuities at large τ or large $\Delta\theta$. Previous studies have suggested that a cut-off $\Delta\theta$ for turbulence fluctuations is: $\Delta\theta = 45^\circ, 50^\circ, 120^\circ$ by Borovsky [2008]; Li [2008]; Veltri and Mangeney [1999] respectively.

We have demonstrated that jumps where $\Delta\theta > 100^\circ$ is primarily due to discontinuities for all τ shown. Therefore, in order to estimate valid values for T_0 and β we slowly lower the value $\tilde{T}(f)$ independently for each frequency and calculate $\mathcal{P}(\Delta\theta)$ from all times where the difference in equation 4.2 is less than or equal to $\tilde{T}(f)$. $\mathcal{P}(\Delta\theta)$ is binned across 36 bins, each of 5° width. We collect the largest value of $\tilde{T}(f)$ at each frequency that results in no data falling into each $\Delta\theta$ bin greater than 100°, such that for each frequency there may be as many as 16 different values of $\tilde{T}(f)$. The spread of data in $\max(\tilde{T})$ for each frequency may be interpreted as the threshold required to avoid discontinuities, where discontinuities are purely characterised as a change in the magnetic field vector direction, as in other studies, such as Borovsky [2008]; Li [2008].

The scatter is shown in Fig. 4.9 where the 16 bins in the range $100^\circ < \Delta\theta < 180^\circ$ are plotted for each frequency. Frequency is plotted along the x-axis against the maximum value of $\tilde{T}(f)$ observed that keep each bin empty along the y-axis . The blue diamonds are the scatter of the raw Ulysses observations. There is a large spread and the ability to find a unique value for T_0 and β is not possible from this scatter. However it is possible to see that our optimal values of T_0 and β lie within this spread, specifically the optimum parameters lie towards the bottom of this scatter, which is expected if $\mathcal{P}(\Delta\theta)$ is limited to the smaller range of $100^\circ < \Delta\theta < 180^\circ$ for the turbulent population. The large spread in $\max(\tilde{T})$ for each frequency highlights the difficultly in using a method that relies on a fixed value of $\Delta\theta$ to discriminate between turbulence and discontinuities. One may see that using a method that depends on a fixed $\Delta\theta$ requires *a priori* selection of scale. However, there is no preferential scale within the inertial range, so *a priori* selection is not possible.

To compare our estimate with pre-existing estimates of $\mathcal{P}(\Delta\theta)$ we show

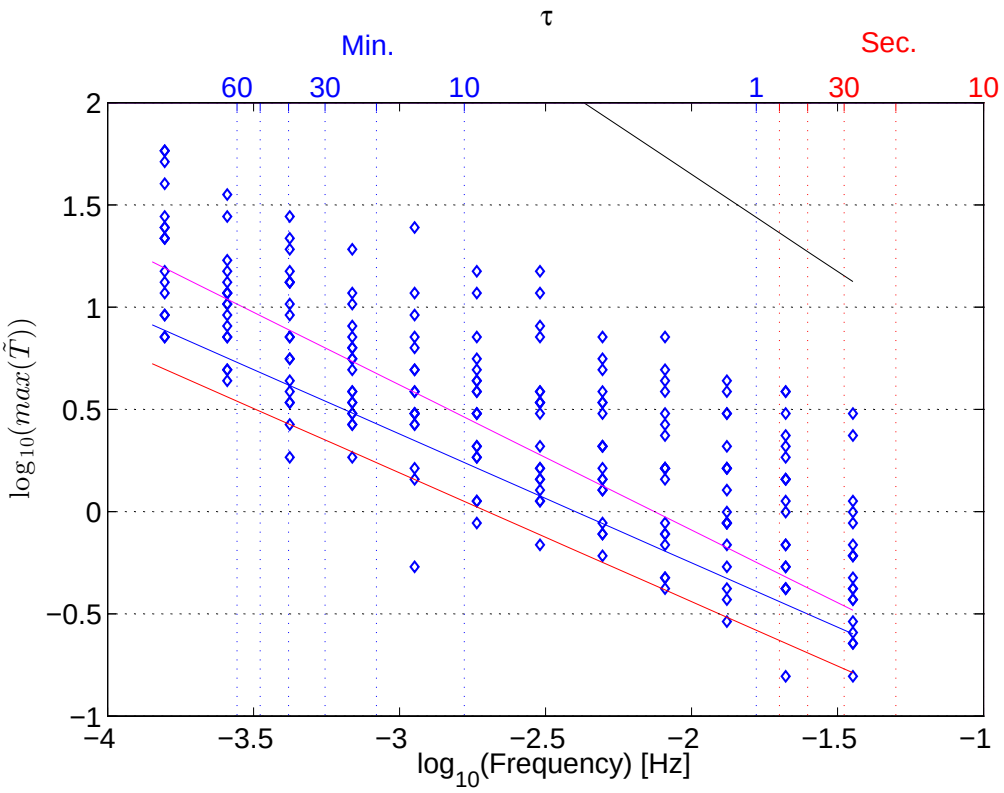

Figure 4.9: Scatter of the largest threshold value which results in the observed $\mathcal{P}(\Delta\theta)$ empty for values of $\Delta\theta > 100°$ in steps $\Delta\theta = 5°$ for the Ulysses observations, shown as blue diamonds. The solid lines refer to the level of filtering where the colours are the same as in Fig. 4.5, such that black, blue, red and magenta lines correspond to $[\beta, log_{10}(T_0)]$ of $[0.95, -0.25]$, $[0.63, -1.51]$, $[0.63, -1.70]$ and $[0.71, -1.51]$ respectively.

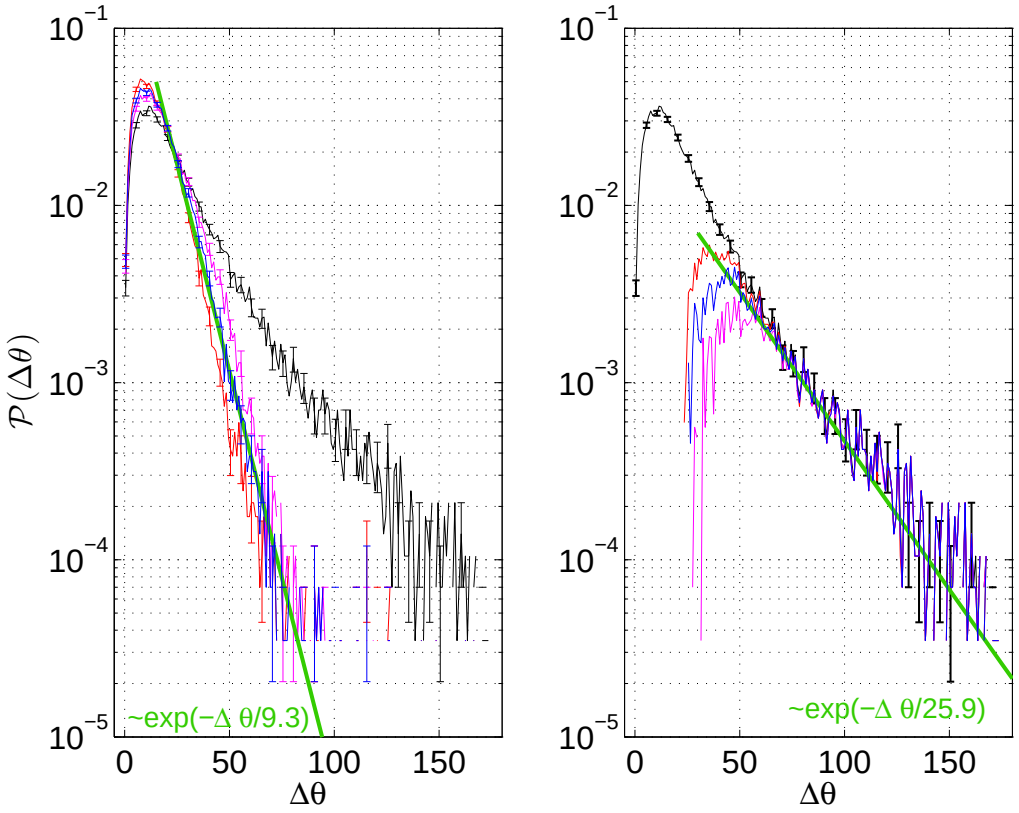

Figure 4.10: The estimated probability distribution for the change in magnetic field at a time-lag of 128s, $\mathcal{P}(\Delta\theta, \tau = 128s)$, where lack, blue, red and magenta lines correspond to filtering with equation 4.2 with $[\beta, log_{10}(T_0)]$ of $[0.95, -0.25]$, $[0.63, -1.51]$, $[0.63, -1.70]$ and $[0.71, -1.51]$ respectively. Left panel: The remaining population after filtering, i.e. the population due to turbulence. The solid green line shows a possible fit to the tail of the turbulent population. Right panel: The raw $\Delta\theta$ population minus the discontinuity filtered $\Delta\theta$ population, i.e. the $\Delta\theta$ population due to discontinuities. The solid green line shows a possible fit to the tail of the discontinuity population.

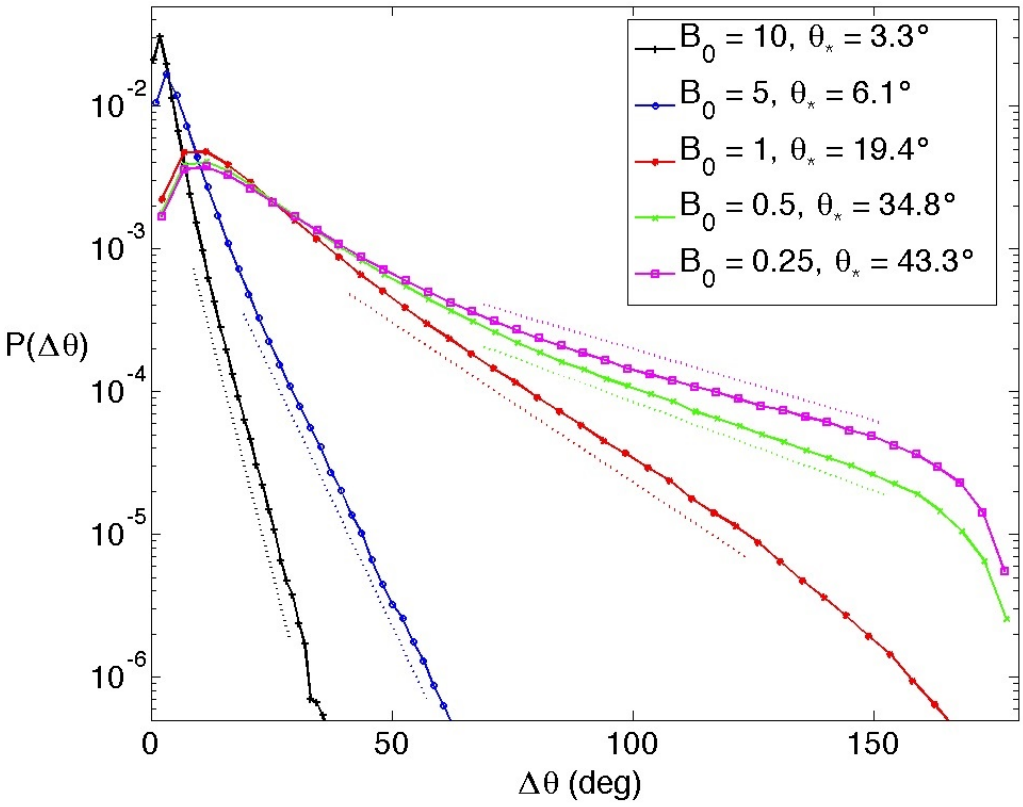

Figure 4.11: "The pdfs for the angular shifts in magnetic field with $\Delta x = 8$ and several background magnetic fields (where $b_{rms} = 1.3$). Each pdf has a region where it takes the form of $\exp(-\Delta\theta/\theta_*)$, where θ_* depends on B_0" after Zhdankin et al. [2012]. $\Delta x = 8$ is the grid point separation within the simulation.

the estimated $\mathcal{P}(\Delta\theta)$ for the turbulence and the discontinuities at the time-scale $\tau = 128s$ for our method using the four cases of T_0 and β displayed in Fig. 4.5. Specifically this allows direct comparison to figure 1 of Borovsky [2010] and an estimated comparison to $\mathcal{P}(\Delta\theta)$ found from MHD simulations by Zhdankin et al. [2012] for various background field strengths relative to the turbulent fluctuations. The figure from Zhdankin et al. [2012] is shown in Fig. 4.11.

The raw population of $\mathcal{P}(\Delta\theta)$ is shown in black for both panels of Fig. 4.10. The three filtered cases are displayed in both panels of Fig. 4.10. in the colours used in Fig. 4.5, such that black, blue, red and magenta correspond to the β and T_0 values of $[0.95, -0.25]$ (raw), $[0.63, -1.51]$ (optimal), $[0.63, -1.7]$ and $[0.71, -1.51]$ respectively. For the filtered cases the estimated turbulent population is displayed in the left panel, while the raw population minus the estimated turbulent population is displayed in the right panel, which corresponds to an estimate of $\mathcal{P}(\Delta\theta)$ for the

discontinuous population.

The estimated turbulent population predominantly occupies an area of the plot corresponding to $\Delta\theta < 100$, however it is not possible to characterise the found turbulent population by a rigid $\Delta\theta$ cut-off value. We have fitted both the turbulent and discontinuity population with a power-law in the tails and find remarkable agreement with that suggested in Borovsky [2010].

There are two possible interpretations; i) the raw $\mathcal{P}(\Delta\theta)$ is composed of two populations, that of turbulence and discontinuities, or ii) the raw $\mathcal{P}(\Delta\theta)$ is purely due to turbulence. As part of the argument that $\mathcal{P}(\Delta\theta)$ is purely due to turbulence we compare our result to that of Zhdankin et al. [2012], which is displayed in Fig. 4.11. It is apparent the functional form of the raw $\mathcal{P}(\Delta\theta)$ and those found from simulations of varying background field strength compared to the root-mean-square fluctuation strength, δB_{rms}, that it may be possible that the raw $\mathcal{P}(\Delta\theta)$ is due to a solely turbulent case where $B_0 < \delta B_{rms}$, such that $\delta B_{rms} \sim 5B_0$. However, if we compare the values of $\mathcal{P}(\Delta\theta)$ for our raw case and the case of a weak background field as shown in Fig. 4.11 we find that there is no agreement. Specifically the small $\Delta\theta$ probability, which is most accurately known, is under represented by approximately an order of ten in the weak background field MHD simulations compared to the observations. However, if we compare our filtered $\mathcal{P}(\Delta\theta)$ to those found by Zhdankin et al. [2012] there is a good agreement for the case where $B_0 \sim 1 - 5\delta B_{rms}$. This implies that $\mathcal{P}(\Delta\theta)$ is not solely due to turbulence. Agreement with Borovsky [2010] demonstrates the power of our method, as only magnetic field measurements have been used to discriminate between turbulence and discontinuities, implying that discontinuities may be accurately detected at the temporal resolution of the magnetic field measurements, which is often greater than other plasma parameters.

4.4.3 Estimating the background magnetic field magnitude relative to the turbulent fluctuations

We now use the surrogate time-series in conjunction with the observations to estimate the ratio $B_0/\delta B_{rms}$. We chose to use the surrogate time-series in conjunction with the observations because using solely the observations may be misleading, as background field discontinuities may be misinterpreted as random fluctuations with a large magnitude.

Our starting point is to use our surrogate time-series that solely consists of jumps and superpose a fractal Brownian motion (fBm) that is projected purely perpendicular with respect to the background field direction and limited in frequency extent. Limiting the frequency extent of the fBm produces a bound time-series,

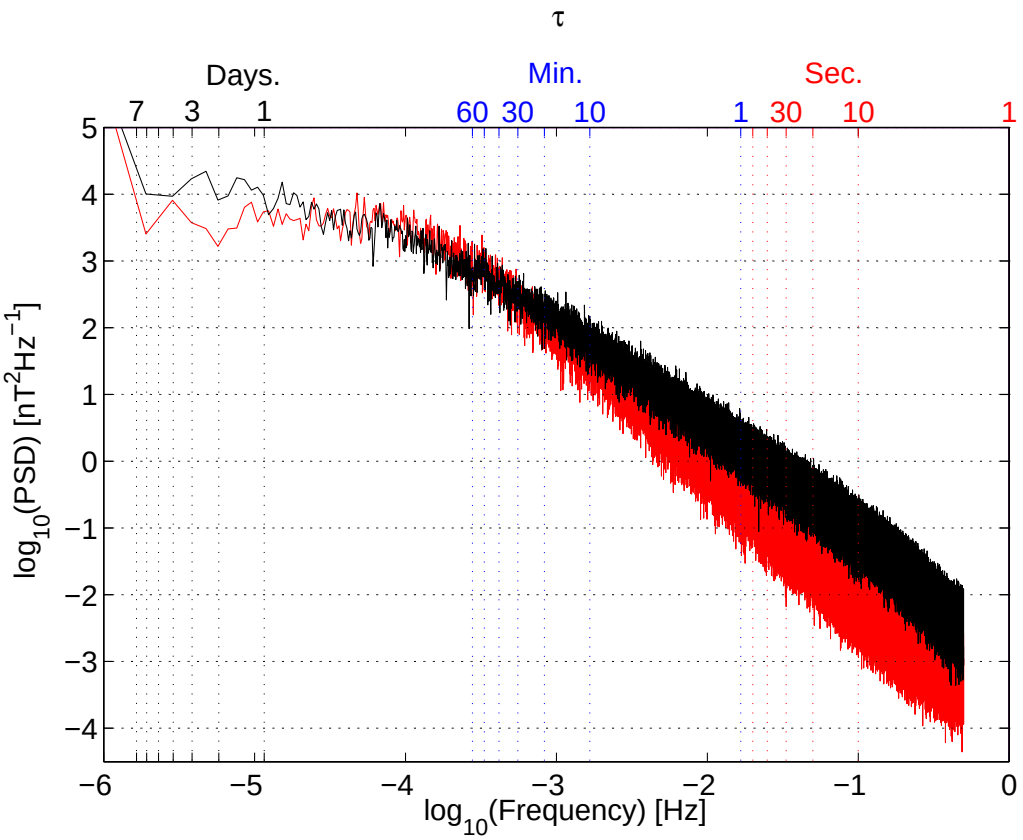

Figure 4.12: Ulysses observations are displayed in black. The surrogate dataset with exponential waiting-time distribution is shown in red. The magnitude, M_0, has been normalized to minimize the difference between the surrogate and observation for $\tau \sim 20$ minutes to 1 day, whilst preserving agreement between the two data at $\tau \sim 1 - 7$ days within uncertainty.

such that the fluctuations remain within a small range of values about zero. Here we will use the exponential waiting-time surrogate time-series and we reduce the magnitude, M_0, from that shown in Figs. 4.6-4.7, such that the magnitude of the background magnetic field discontinuities are reduced from the value that best fits the observations to the lowest magnitude that allows agreement with the observations within uncertainty, shown in Fig. 4.12. We choose to use the exponential waiting-distribution to minimise free parameters and reduce the magnitude such that we may find the lowest reasonable ratio of $B_0/\delta B_{rms}$ within the framework of a discontinuous background magnetic field and turbulence population. Minimizing the background magnetic field also has the effect of reducing the dominance of the background field PSD in the region of $\tau \sim 20$ min $\rightarrow$ 1 day. We will use a selection of δB_{rms} strengths, such that $B_0 = [1, 3, 5]\delta B_{rms}$ and we use an IK-like scaling for the fBm, such that the spectral exponent of the fBm time-series is $\gamma_s = -1.5$. We shall then compare the power spectral density and $\mathcal{P}(\Delta\theta)$ to estimate the actual value of $B_0/\delta B$ for our interval and compare this to the results Zhdankin et al. [2012] and the estimated ratio directly from the observations.

The power spectral density of the **R** component of the solar wind and our surrogate time-series may be seen in Fig. 4.13. The observations, background field jump process with exponential waiting-time and the superposed time-series with $B_0/\delta B_{rms} = 1, 3, 5$ are displayed in black, red, magenta, blue and green respectively. The best agreement between our surrogate time-series and the observations can be seen to coincide with the case where $B_0/\delta B_{rms} = 3$.

An estimate of $\mathcal{P}(\Delta\theta)$ for the observations, the superposed time-series with $B_0/\delta B_{rms} = 1, 3, 5$ and the turbulence population found from the observations are displayed in black, magenta, blue, green and red in Fig. 4.14. Again we find a good match between the observations and the superposed surrogate time-series with $B_0/\delta B_{rms} = 3$. Therefore, we conclude that the observations may be modeled as a mixture of a discontinuous background field and turbulence where $B_0 \gtrapprox 3\delta B_{rms}$ This fulfills the criteria that $\delta|B| \sim \delta B_{\parallel}$

The differences between the surrogate dataset and observations for $\mathcal{P}(\Delta\theta)$ is informative. For small $\Delta\theta$ differences are most likely due to modeling the probability distribution for the fluctuations of the plasma as a fBm, which is a very simplified model for turbulent fluctuations. The difference between the observations and the surrogate dataset in the region $40^\circ < \Delta\theta < 80^\circ$ highlights that the background field discontinuities do not occur randomly, but there is a non-trivial correlation between discontinuities. Such a correlation could be consistent with the suggestion of flux tubes dominating solar wind structure (e.g. see Ness et al. [1966]; Bruno and

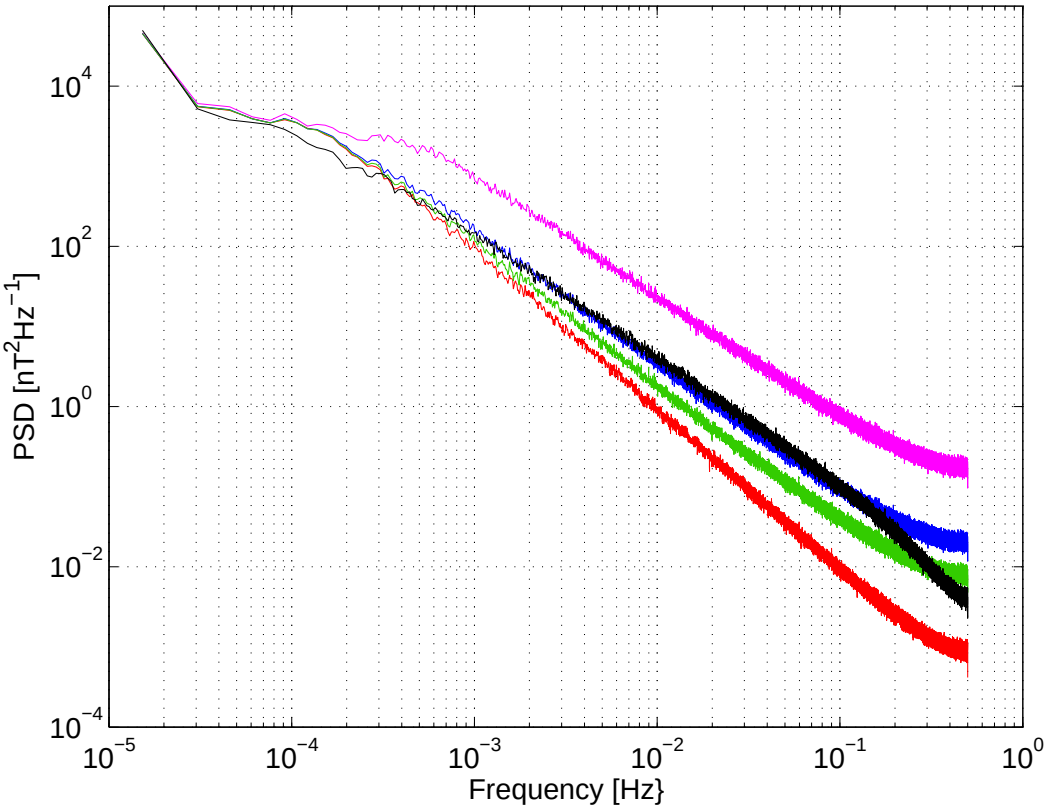

Figure 4.13: The PSD for inertial-range scales of the **R** component from observations and the surrogate dataset, which models observations as a background field described by jump process with exponential waiting-time superposed with a range of fluctuations described by a fractal Brownian probability distribution consistent with IK scaling to a frequency of approximately 3.7×10^{-4} ($\tau = 60$ minutes). Displayed are the raw observations, just the background jumps process and superposed ratios of $B_0/\delta b = 5, 3, 1$ as black, red, green, blue and magenta respectively.

Carbone [2005]; Borovsky [2008] and references within).

4.4.4 MHD turbulence simulations

We use snapshots of two distinct fully developed incompressible MHD turbulence simulations as possible models for the inertial range fluctuations due to turbulence. The MHD simulations will serve to confirm that the geometric considerations used in equation 4.1 are valid in for plasma turbulence. We will also attempt to find the temporal-scales for which the threshold may be taken to be valid, i.e. for what temporal-scales is equation 4.1 valid. The two simulations we used are: Case I is a $1024^2 \times 256$ forced turbulence simulation with a well defined background field of

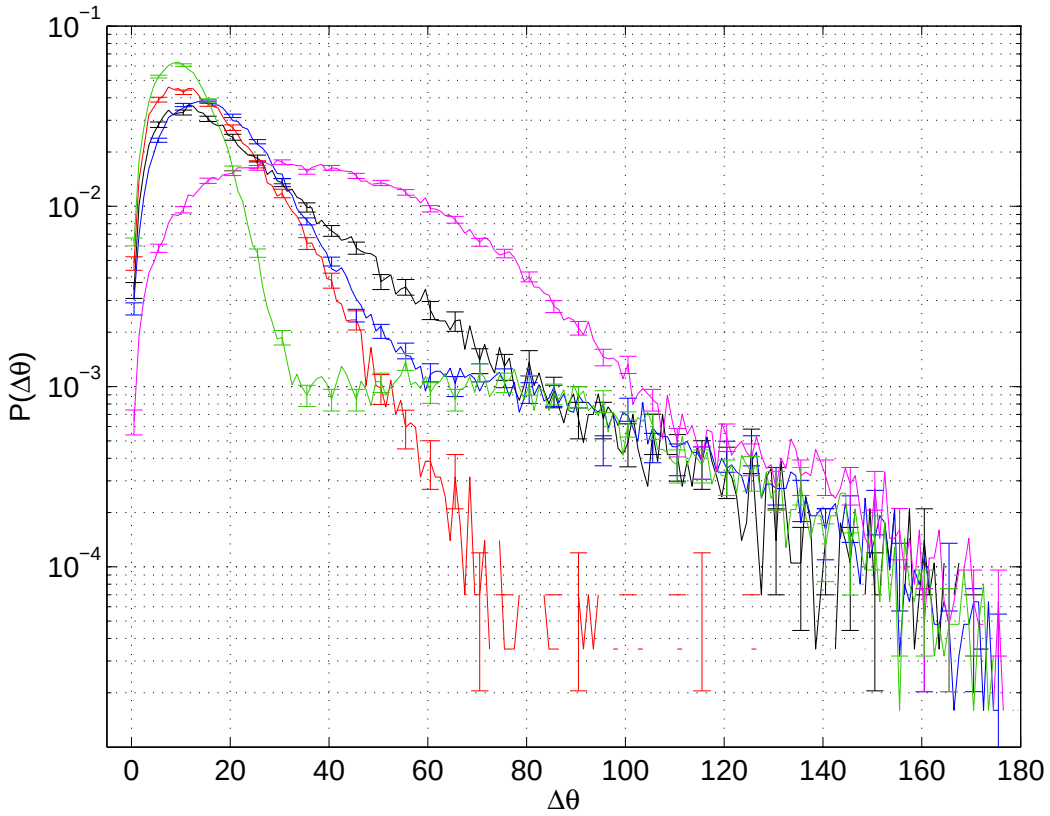

Figure 4.14: The estimated probability distribution for the change in magnetic field at a time-lag of 128s, $\mathcal{P}(\Delta\theta, \tau = 128s)$. The colours correspond to the same scenario as Fig. 4.13.

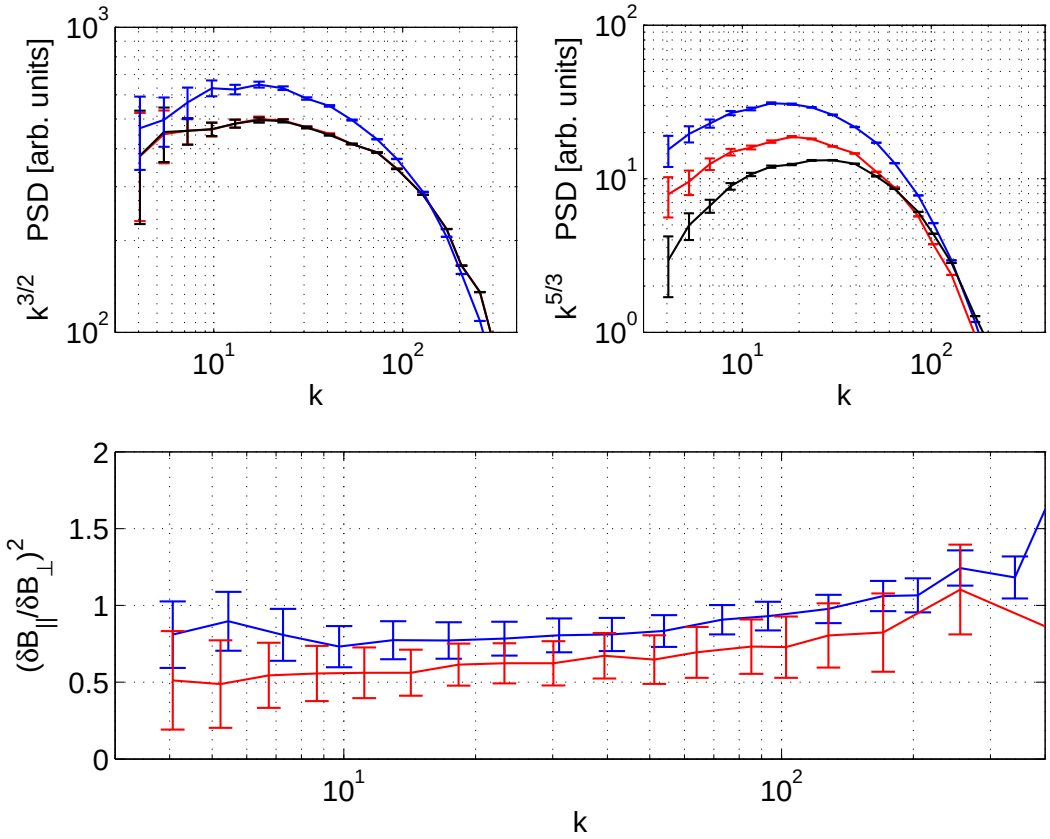

Figure 4.15: The top panels display the variance anisotropy of the MHD simulations. the perpendicular, parallel and modulus power are shown in blue, red and black respectively. Left panel: The forced simulation with $B_0 \sim 5\delta b_{rms}$. Right panel: The decaying simulation with $B_0 = 0$. Bottom panel: Dispays a proxy for the compressibility estimate used in the solar wind for the two simulations, such that blue and red correspond to the forced and decaying simulations respectively.

$B_0 \sim 5\delta B_{rms}$. Case II is globally isotropic freely decaying turbulence on a grid of 512^3. Therefore Case II does not have a background field, $\mathbf{B}_0$, but there is an effective local background field, $\mathbf{b}(r, f)$, created by the fluctuations themselves which is constantly evolving. The inertial range of both cases may be approximated by $k \sim [8 - 30]$. These simulations are identical to those used in Chapter 3, such that details may be found in Müller and Grappin [2005].

For each of the simulations we calculate the power spectral density of the fluctuations, $\delta\mathbf{B}(t, f)$ with respect to the local background field estimate, $\mathbf{b}(t, f)$. We estimate the power of the perpendicular and parallel components with respect to the local background field estimate and the modulus of the fluctuations. We have plotted the perpendicular component power, $P_\perp$, (blue) and parallel component power, $P_\parallel$,

(red) for both simulations with the power of the modulus of the fluctuations, $P_{|B|}$, (black) in the top panels of Fig. 4.15. The top left panel displays case I corrected by $k^{3/2}$ and the top right panel displays case II corrected by $k^{5/3}$. The bottom panel displays the ratio of the $P_{\parallel}/P_{\perp}$ as a function of scale for case I (blue) and case II (red). In the solar wind this may be used as a proxy for the compressibility estimate (e.g. TenBarge et al. [2012]; Kiyani et al. [2013]). The errorbars display three standard errors for all values plotted.

It can be seen that Case I (top-left panel) has an agreement between $P_{\parallel}$ and $P_{|\mathbf{B}|}$, whereas Case II shows a disagreement between $P_{\parallel}$ and $P_{|\mathbf{B}|}$. One could have anticipated that Case I would display agreement between $P_{\parallel}$ and $P_{|\mathbf{B}|}$, as the strong background magnetic field enforces $B_0 > \Delta B$, which is a key condition used in deriving equation 4.1. However, Case II does not have an externally applied background field, so $B_0 \ll \Delta B$, thus agreement between $P_{\parallel}$ and $P_{|\mathbf{B}|}$ is not found. Importantly, one can see that providing $\delta B_{rms} > B_0$ the criteria, $P_{\parallel} \sim P_{|B|}$ is true for all temporal/spatial scales.

Generally for turbulence $E(k) \sim k^{\gamma}$, where $\gamma < 0$. Therefore, the largest scale of the inertial range dominates the δB_{rms}. Thus, the simulations confirm the criteria for our method of detecting discontinuities is either true/untrue for all scales within the inertial range. This provides a valuable condition for determining whether discontinuities are present and significant, as these simulations by definition provides information on how the system behaves in the absence of discontinuities.

The bottom panel displays $P_{\parallel}/P_{\perp}$, which is a proxy for a measure of compressibility used in the solar wind (e.g. see TenBarge et al. [2012] and references within). Similar behaviour is shown for both simulation cases, that the compressibility estimate is not a function of scale within the inertial range. In principle this could be used as a condition to determine whether discontinuities are present in the solar wind by comparison with observations. However, in reality both a quantitative value and a trend are required. A quantitative estimate is not possible from these MHD simulations as there are "pseudo-Alfvén" waves present, which increases the perceived level of compressibility for this estimate. Importantly, the pseudo-Alfvén waves behave as a passive scalar, in that they are not able to influence the Alfvén wave turbulent cascade. Therefore, it is reasonable to conclude that the compressibility estimate of $P_{\parallel}/P_{\perp}$ should remain approximately constant if the observations are due solely to MHD turbulence.

All fluctuations and structures contained within the simulations are a result of simulating turbulence. Therefore, the results presented in this section are presented as is, i.e. there has been no filtering of the time-series cuts from the

simulations. Thus, the observations from the simulations offer a comparison for the discontinuity filtered solar wind data, and so, simple characteristics that should be recaptured if the discontinuities are completely removed from the observations.

4.5 Results

In the previous sections we presented a new scale-free method for detecting discontinuities in a time series of solar wind observations based on geometric considerations for the case where $B_0 > \delta B_{rms}$. We have also shown that our method is applicable to the solar wind, as we estimate $B_0 \sim 3\delta B_{rms}$ as a lower limit by using our surrogate dataset, previous works and observations. We have analyzed the variance of the modulus and parallel component with respect to the background magnetic field for the MHD simulations for two cases; i) $B_0 > \delta B_{rms}$ and ii) $B_0 \ll \delta B_{rms}$. We found that when $B_0 > \delta B_{rms}$ the expectation $P_{\parallel} \sim P_{|B|}$ (See equation 4.1) is realized for all temporal-scales of the turbulence. We shall now investigate how the discontinuities affect the results of conventional analysis carried out with regards to anisotropy, including variance anisotropy, trace anisotropy and intermittency.

4.5.1 Variance Anisotropy

The variance anisotropy is a measure of how the fluctuation power is orientated with respect to the background magnetic field. In order to obtain the variance anisotropy the background field needs to be estimated accurately, as any deviation will influence the result when decomposing $\delta\mathbf{B}(t, f)$ into components parallel and perpendicular to $\mathbf{b}(t, f)$, to produce $P_{\parallel}, P_{\perp}$ estimates. We examine the effect of discontinuities on the estimated variance anisotropy by using equation 4.2 with T_0 and β from section 4.2. Alongside, we demonstrate the effect of discontinuities with a model time-series. The model time-series is constructed by using the surrogate time-series that consists solely of discontinuities with an exponential waiting-time and a superposed fBm time-series projected to be perpendicular for all times of the time-series. The perpendicular fluctuations have a strength $B_0 = 3\delta B_{rms}$ and have IK-like scaling, i.e. a spectral exponent of $-3/2$. The fluctuations exist over a broad range of scales corresponding to approximately $1s \rightarrow 60$ min. This is the optimum model used in Section 4.4.1.

The perpendicular and parallel components of the variance anisotropy are plotted in the left and right panels of Fig. 4.16 respectively. The colours are the same as used for the parameters identified as I-IV in Fig. 4.5, such that $[\beta, T_0]$ =[0.95, −0.25], [0.63, −1.51], [0.63, −1.70], [0.71, −1.51] are displayed in black,

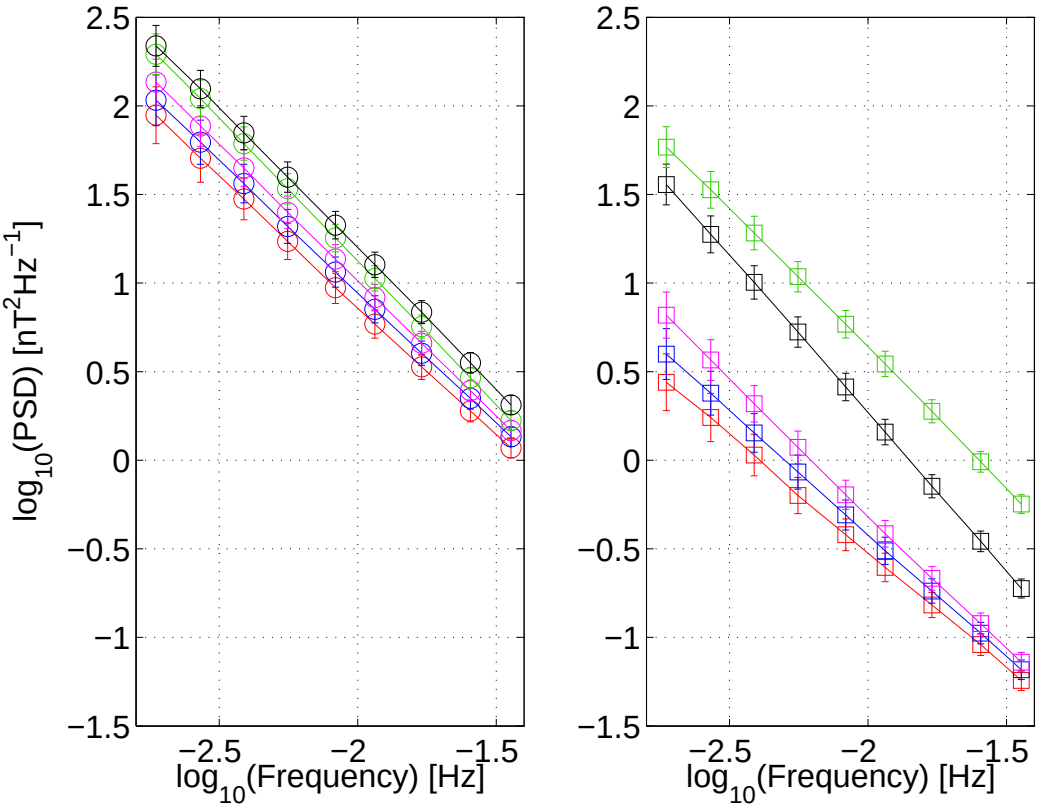

Figure 4.16: The variance anisotropy of the Ulysses interval, where $P_{\perp}$ and $P_{\parallel}$ are displayed in the left and right panel respectively. The variance anisotropy using the global background field, local background field and the three levels of filtering in green, black(I), magenta(III), blue(II) and red(IV) respectively, where Roman numerals correspond to Fig. 4.5. The left and right panels display the perpendicular and parallel components respectively.

blue, red and magenta respectively. The results of using a global mean field averaged over the entire time-series has been has also been added in green.

We find that discontinuities have an effect on both components. Both components display a greater spectral exponent within the inertial range scales when discontinuities are present. The greatest change in spectral exponent is found between the raw and filtered local background magnetic field for the parallel component, which is approximately $\Delta\gamma_{\parallel} \sim 0.4$. There is also a large change between the filtered case and the global background magnetic field for the parallel component, although the spectral exponent is similar. Significantly, signs of Kolmogorov-like scaling are removed when the local background magnetic field is filtered to remove discontinuities. Therefore, we will find that discontinuities have a significant influence upon the conclusions drawn from variance anisotropy analysis.

In an attempt to understand whether this is a reasonable result we will show how equation 4.1 suggests that the discontinuities do introduce additional scaling for the parallel component. We will also use the model data that contains only discontinuities and fluctuations that scale as $\gamma_{\perp} \sim -3/2$.

Consider a time-series with a discontinuity between $t \rightarrow t + \tau$, such that $\mathbf{B}_{0,1}$ and $\mathbf{B}_{0,2}$ are separate sides of the discontinuity. Allow the local estimated background field to be $\mathbf{b}_t$ and $\mathbf{b}_{t+\tau}$. Averaging across a discontinuity will result in $\mathbf{b}_t - \mathbf{b}_{t+\tau} < \mathbf{B}_{0,t} - \mathbf{B}_{0,t+\tau}$. Therefore, rearranging equation 4.1, $\delta B_{\parallel} \sim \delta|B| - (\mathbf{b}_t - \mathbf{b}_{t+\tau}) > \delta|B| - (\mathbf{B}_{0,t} - \mathbf{B}_{0,t+\tau})$. As $\delta|B|$ does not depend on the averaging scheme it is expected that the parallel component will be greater in the presence of discontinuities. As the scale increases $\mathbf{b}_t - \mathbf{b}_{t+\tau}$ reduces, until the limit where the whole time-series is averaged, such that $\mathbf{b}_t = \mathbf{b}_{t+\tau}$. This produces a scale dependent growth in the parallel component, and so produces artificial scaling.

We now consider our model time-series. The variance anisotropy is presented in Fig. 4.17, where the parallel, perpendicular and modulus power are shown in blue, red and black. The compressibility proxy estimate is displayed in green in Fig. 4.19. The similarity between the results of the model variance and that of the raw observation are remarkable. The variance PSD of the surrogate time-series may be compared to Fig. 4.18, whilst Fig. 4.19 allows comparison between the compressibility estimate for the surrogate time-series and with the observations where various method of calculating the background magnetic field are used. For the surrogate time-series the spectral index of the parallel component displays the greatest value within the inertial range, with a value of $\gamma_{\parallel} \sim -1.8$, the perpendicular spectral exponent is $\gamma_{\perp} \sim -5/3$ and the spectral exponent of the modulus of the fluctuations of $\gamma_{|B|} \sim -1.4$.

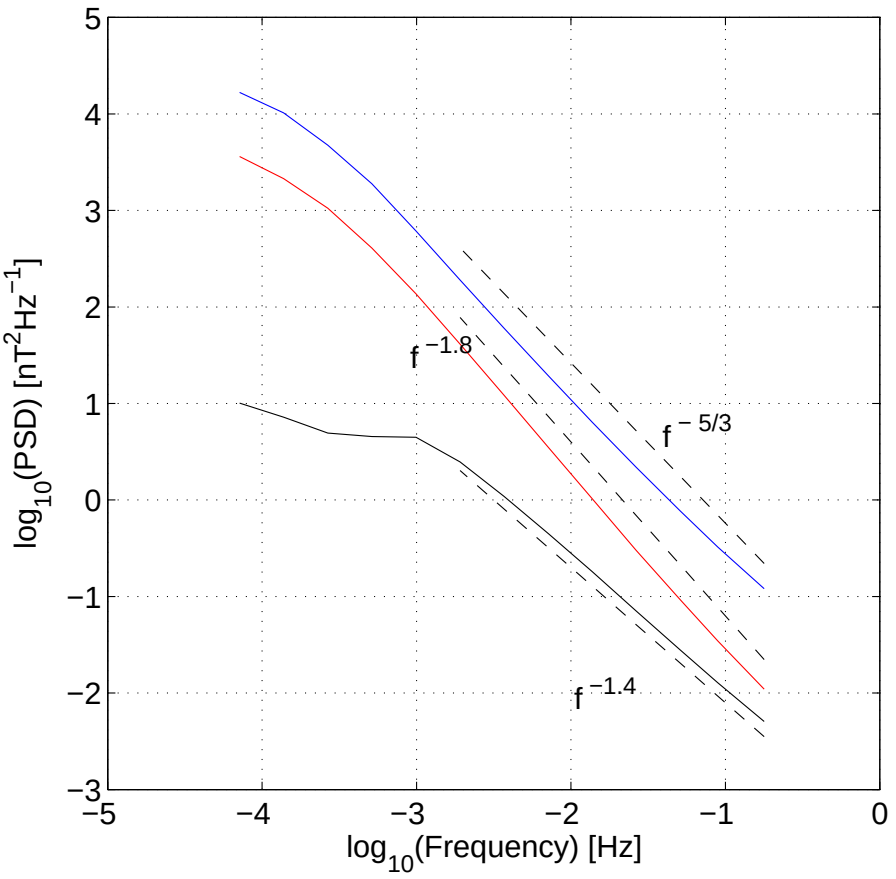

Figure 4.17: The variance anisotropy for the model data with $B_0 \sim 3\delta b_{rms}$. The variance anisotropy of the perpendicular, parallel and modulus power are in blue, red and black respectively. Power-law fits have been added with dashed black lines where appropriate for comparison with solar wind data.

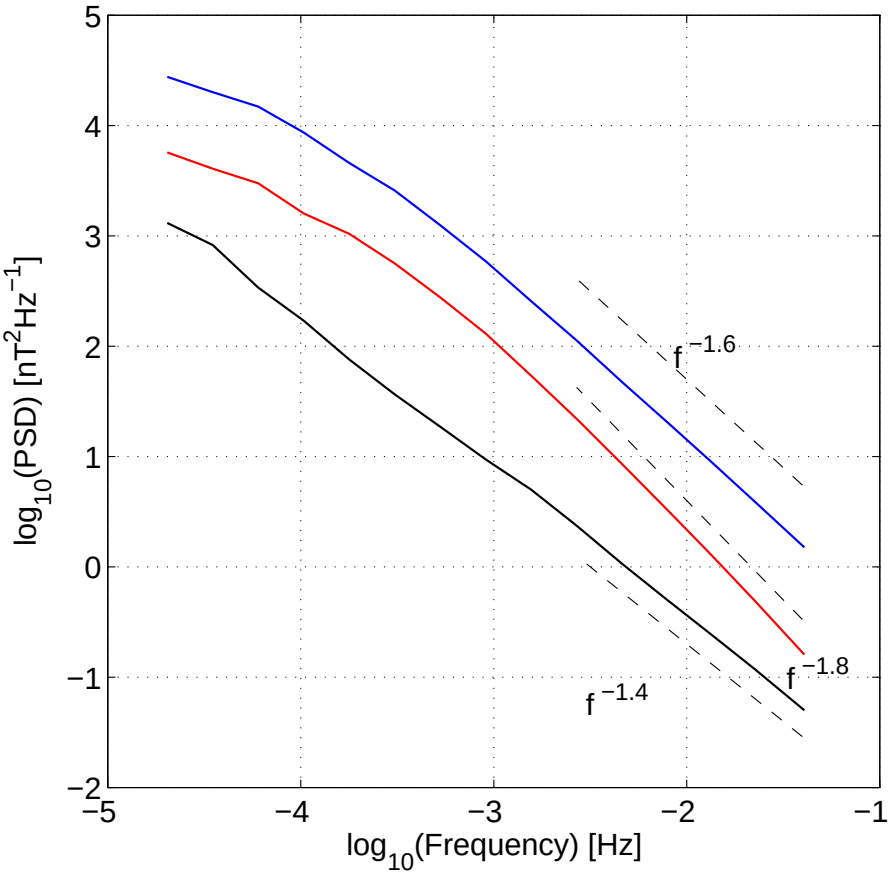

Figure 4.18: The variance anisotropy of the Ulysses data, where the perpendicular ($P_\perp$), parallel ($P_\parallel$) and modulus ($P_{|\mathbf{B}|}$) are displayed in blue, red and black respectively. The dashed black lines correspond to power-law fits to each component within the inertial range scales, such that the perpendicular, parallel and modulus are fit with $f^{-1.6}$, $f^{-1.8}$ and $f^{-1.4}$ respectively.

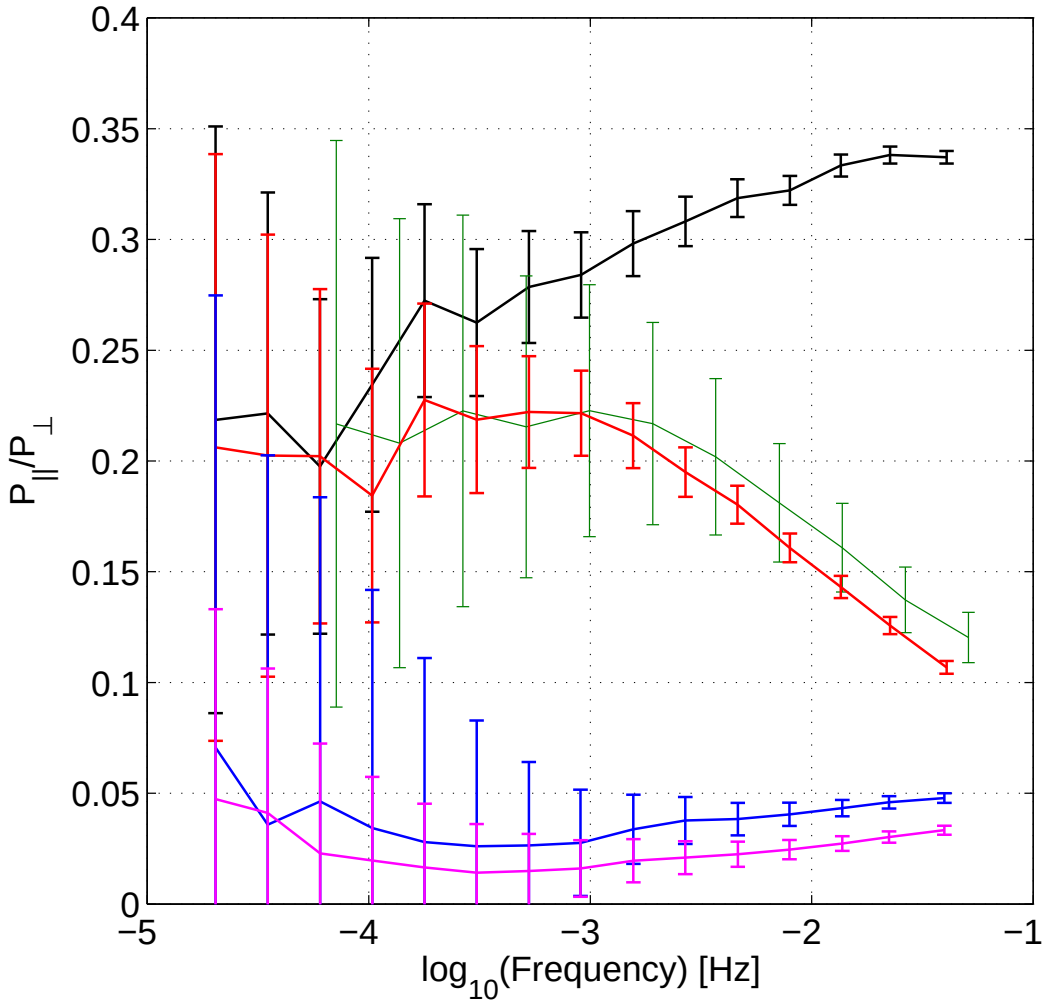

Figure 4.19: Compressibility estimates for various methods. The global background field method is shown in black. The raw local and optimized filtered cases are displayed in red and blue respectively. Magenta displays $P_{|\mathbf{B}|}/P_{\perp}$ for the raw data using the local background field. The $P_{\parallel}/P_{\perp}$ estimate from our surrogate dataset is shown in green.

The compressibility estimates shown in Fig. 4.19, $P_{\parallel}/P_{\perp}$, are displayed with one standard error. The optimum case for our discontinuity filtering method, such that β and T_0 are chosen to minimize the rmsd between $P_{\parallel}$ and $P_{|\mathbf{B}|}$, is shown in blue. In magenta $P_{|\mathbf{B}|}/P_{\perp}$ for the raw data is displayed, which may be considered as a pre-filtering estimate of $P_{\parallel}/P_{\perp}$, where $P_{|\mathbf{B}|}$ is used as a proxy for $P_{\parallel}$. The uncertainty in $P_{|\mathbf{B}|}/P_{\perp}$ is reduced compared to the filtered $P_{\parallel}/P_{\perp}$ estimate, as the ensemble of $P_{|\mathbf{B}|}/P_{\perp}$ is greater than that of $P_{\parallel}/P_{\perp}$ after the discontinuities have been filtered. The raw and surrogate $P_{\parallel}/P_{\perp}$ are shown in red and green, whilst the $P_{\parallel}/P_{\perp}$ estimate produced by using the global background field estimate is shown in black.

It can be seen that the values and functional form are similar between the model time-series and the raw local field method. The similarities found between the model data and the raw local background field estimate method suggest that the local field estimate introduces additional scaling due to the presence of discontinuities. Our model appears to be a reasonable approximation to the scaling of the solar wind where we use the following parameters; $B_0 \sim 3\delta B_{rms}$, $\gamma_{\perp} \sim -3/2$, $W_T \sim$ exponential and $\lambda = 20$ minutes. In our model no parallel fluctuations are explicitly included, however the perpendicular fluctuations do not conserve the magnitude of the field. Therefore, there are fluctuations in the modulus of the model time-series, which must also be interpreted as parallel fluctuations.

4.5.2 Trace Anisotropy

Consider the energy spectral density tensor sampled at-a-point via Taylor's hypothesis. The resulting one-dimensional spectral density observed will be $\tilde{P}_{ij}(f,\theta) = \int \mathrm{d}^3\mathbf{k} P_{ij}(\mathbf{k})\delta(2\pi f - \mathbf{k}\cdot\mathbf{V}_{sw})$, where $P_{ij}(k)$ is the energy spectral tensor, $\mathbf{V}_{SW}$ is the solar wind velocity and $\mathbf{k}\cdot\mathbf{V}_{SW} = 2\pi f$ is the plane in $\mathbf{k}$-space that is integrated over when using Taylor hypothesis to construct $\tilde{P}_{ij}(f,\theta)$. We consider the delta function that defines the integration plane, which we expand for clarity to $\delta(2\pi f/V_{sw} - k_{\perp}\sin\theta - k_{\parallel}\cos\theta)$. Clearly, if $\theta = 0^{\circ}$ or $\theta = 90^{\circ}$ only $k_{\parallel}$ or $k_{\perp}$ are sampled respectively. Therefore the trace, $P_{\theta}^{T} = \Sigma_i P_{ii}$, of the magnetic field is used to estimate the reduced one-dimensional k-spectra of turbulence theories in the solar wind [Horbury et al., 2008; Podesta, 2009; Tessein et al., 2009; Wicks et al., 2010; Chen et al., 2010; Li et al., 2011], such as Goldreich and Sridhar [1995].

Previous results (e.g. see Horbury et al. [2008]; Podesta [2009]; Wicks et al. [2010]; Chen et al. [2010] and references within) have been interpreted as consistent with Goldreich and Sridhar [1995], in that the spectral exponent of the trace power was found to depend on the sampling direction with respect to the local background

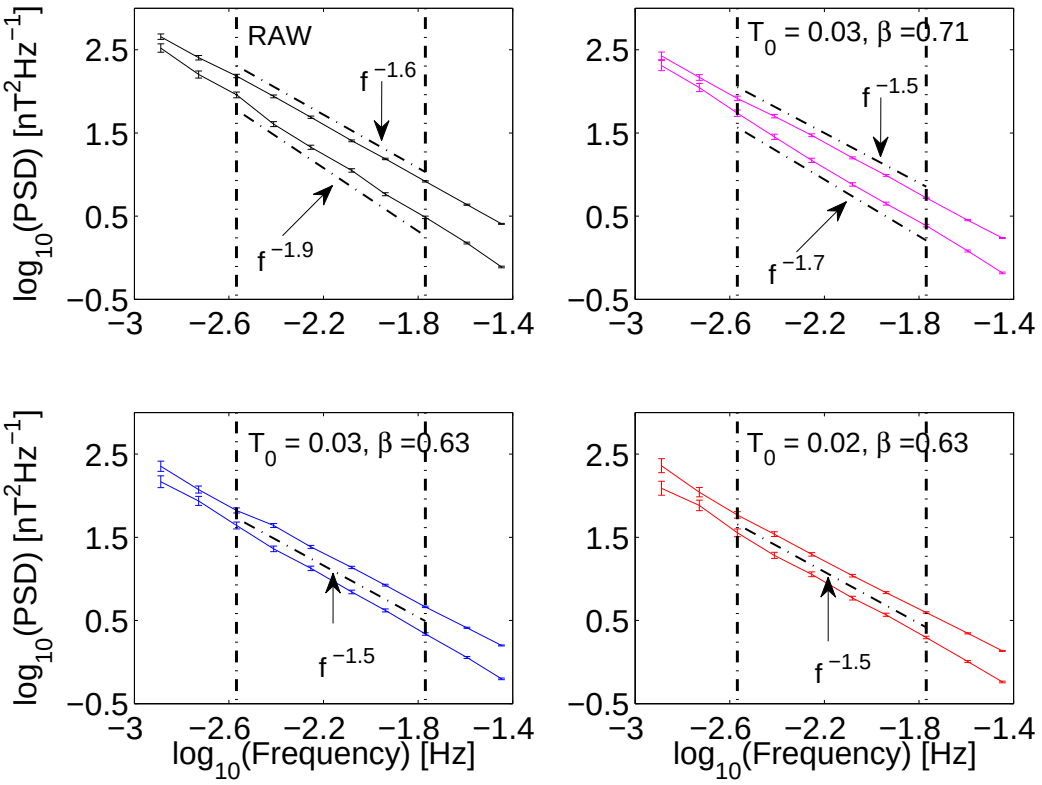

Figure 4.20: Trace anisotropy under discontinuity filtering
The trace PSD, where $P_{\perp}^{T}$ contains the greatest and $P_{\parallel}^{T}$ the least power in all panels. The raw and optimum filtered case are shown in left-top and left-bottom panels respectively. The under-filtered and over-filtered cases are shown in right-top and right-bottom panels respectively. The vertical dash-dot lines display the frequency limits used for the power-law fits in the inertial range.

magnetic field estimate. When the sampling direction is parallel ($P_{\parallel}^{T}$) to the local magnetic field, $\theta_{BV} = 0° - 10°$, the measured trace power PSD has a steeper spectral index than the perpendicular case ($P_{\perp}^{T}$), where $\theta_{BV} = 80° - 90°$. Typically the difference in spectral index is 1/3. As $P_{\parallel,\perp}^{T}$ corresponds to a direct measurements of the one-dimensional reduced spectra of $k_{\parallel,\perp}$ the observed spectral index difference suggests Goldreich and Sridhar [1995] phenomenology in the solar wind.

The trace power for both the raw and filtered data is shown in Fig. 4.20 for the Ulysses interval. All the panels display a different level of filtering according to Fig. 4.5, with the greatest power in $P_{\perp}^{T}$ and the smallest power in $P_{\parallel}^{T}$ for all panels and all scales. The top -left, to-right, bottom-left and bottom-right panels display the raw case, β greater than optimal, optimal and T_0 lower than optimal respectively.

Within the inertial range it can be seen that the removal of discontinuities from the observations produce a spectrally isotropic trace power, i.e. there is no dependence upon $\theta_{\mathbf{VB}}$. Our result is consistent with IK phenomenology, simulations by Grappin and Müller [2010] and previous observations by Li et al. [2011]. Thus, the discontinuities alone can be shown to be responsible for the raw observations displaying spectral exponents consistent with GS phenomenology, i.e. the trace spectral exponents depend on $\theta_{\mathbf{BV}}$, such that they scale as $P_{\perp}^{T} \sim -5/3$ and $P_{\parallel}^{T} \sim -2$.

4.5.3 Intermittency

We plot the perpendicular and parallel $\zeta(m)$ scaling in the left and right panels of Fig. 4.21 respectively. The global background field, raw local background field, optimum filtering, the over filtered and under filtered cases can be seen in green, black, blue, red and magenta respectively. In the right panel, the dashed black line shows the raw scaling of the modulus of the magnetic field. The $\zeta(m)$ was calculated at $\tau = 1 \rightarrow 10$ minutes and the error bars signify a 95% confidence interval estimated by separating the observations into 10 equally sized ensembles.

The parallel component of the distribution is most affected by the presence of discontinuities within the time-series. Where both the raw local and global background field overestimate the magnitude of the higher moments. The optimum filtering reproduces all moments of the modulus population displayed here within uncertainty. The perpendicular component shows little change, regardless of the method used.

The parallel distribution may be sensitive to discontinuities for the following reasons; 1) for a particular scale the perpendicular distribution is more extended to

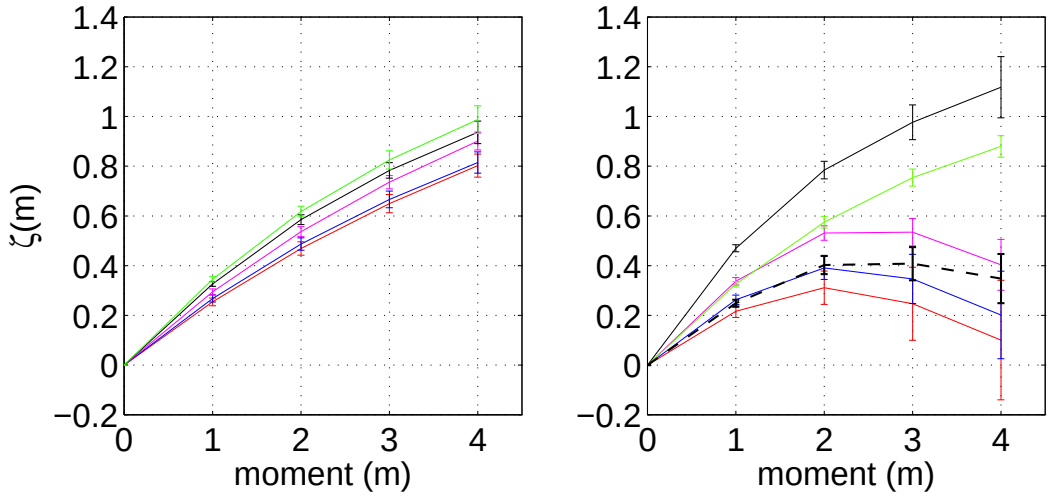

Figure 4.21: $\zeta(m)$ plots of the intermittency for $\delta B_{\perp}$ and $\delta B_{\parallel}$ are shown in the left and right panels respectively. The global background field, raw local background field, optimum filtered, under-filtered and over-filtered cases are displayed in green, black, blue, magenta and red respectively.

larger magnitudes than the parallel distribution, this is known from section 4.5.1. where it was estimated that approximately 95% of the power resides in the perpendicular component 2) the local background magnetic field is poorly estimated in the vicinity of a discontinuity. Therefore, if we consider a perpendicular fluctuation misinterpreted as a parallel fluctuation, then the fluctuation may exist in the poorly sampled wings of the parallel distribution, shown in red for the schematic of Fig. 4.22. However, if the converse is considered a parallel fluctuation will lie in the well sampled core of the perpendicular distribution, shown in blue in Fig. 4.22. Thus, a poorly defined background field has a greater effect when a perpendicular fluctuation is interpreted as a parallel fluctuation than vice versa. Importantly, neither of the parallel or perpendicular component from our intermittency analysis is best fit by a linear relation that passes through the origin. Thus, the internal intermittency (intermittency due to turbulence and not time-series discontinuities) is still present after filtering.

4.6 Conclusion

This chapter is focused on the concept of the local background magnetic field and discontinuities, which are both controversial topics in the field of solar wind analysis. We have demonstrated not only that non-turbulent discontinuities exist within the

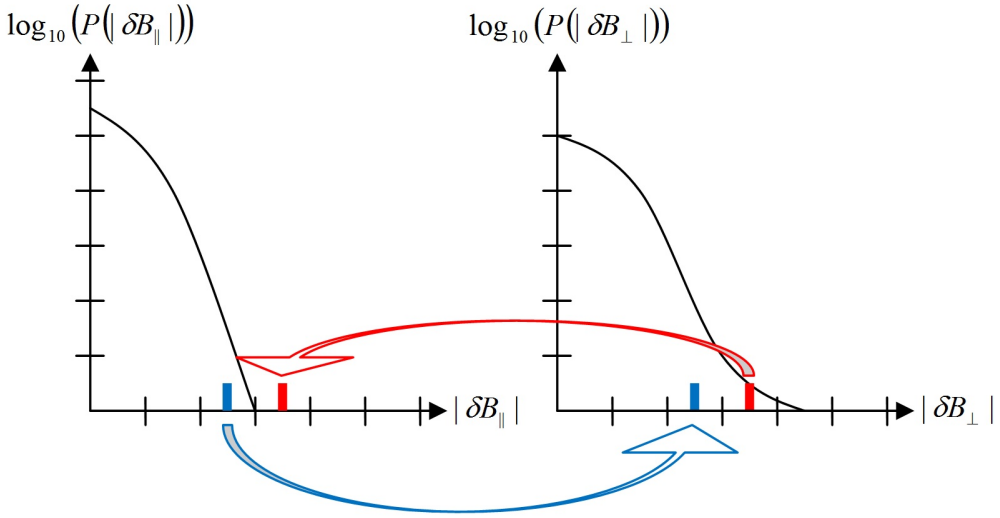

Figure 4.22: Schematic representation of the $\delta B_{\parallel}$ and $\delta B_{\perp}$ fluctuation distributions at a specific scale. A single fluctuation within the parallel and perpendicular distributions are shown by a small vertical bar in blue and red respectively. The blue (red) arrow shows a parallel (perpendicular) fluctuation being misinterpreted as a perpendicular (parallel) fluctuation due to discontinuities in the background magnetic field estimate.

observations, but that these features have a significant effect upon the conventional methods for determining the background magnetic field, specifically discontinuities result in anomalous scaling in the trace, variance and intermittency scaling.

We began by demonstrating a non-turbulent time-series discontinuity by using two satellites separated by a comparatively short distance in the solar wind. We then proposed a criterion to detect and remove the discontinuities for the observational time-series, which is only valid under the condition that the magnitude of the background magnetic field is greater than the turbulent fluctuations and the background magnetic field varies slowly on a spatial/temporal scale compared to the turbulence. In principle any contradictory criteria may be used to detect background magnetic field discontinuities, providing the fluctuations and background magnetic field are independently calculated, e.g. another criterion for detecting discontinuities might be to find times where $|\mathbf{B}|^2 \neq |\mathbf{B}_0|^2 + 2(\mathbf{B}_0 \cdot \delta\mathbf{B}) + |\delta\mathbf{B}|^2$, where $\mathbf{B}_0$ is the background magnetic field and $\delta\mathbf{B}$ is a magnetic fluctuation.

We discussed the background magnetic field estimate calculated via both the global average method and the local background magnetic field calculated over frequency specific windows. We demonstrated the uncertainty of the actual background magnetic field direction for both methods. It was shown that the global background

magnetic field has a consistently large uncertainty when the background magnetic field is structured. However, the local background magnetic field has an uncertainty that is dependent on the temporal-scale, and so becomes an increasingly poor estimate of the actual background field as the temporal-scale is increased.

We found the free parameters of our discontinuity filtering criteria for these Ulysses observations and tested our criteria. We constructed a surrogate dataset that represents a time-series that is solely composed of discontinuities with a specific waiting-time between jumps. We also estimated a lower bound for the magnitude of the fluctuations with respect to the background magnetic field. A lower estimate of $B_0 \sim 3\delta B$ was found, which is sufficient for our discontinuity filtering criteria.

We used our new method for detecting and removing discontinuities from the observations to reanalysis the variance, trace and intermittency anisotropy within the solar wind. We found that the parallel component of both the trace and variance estimate was most affected by discontinuities, as the parallel component has less power than the perpendicular component and comparable power to that of the discontinuities within the time-series. Our results do not support the Goldreich and Sridhar [1995] model within the solar wind and highlight the care that must be taken when defining the background magnetic field within the structured medium of the solar wind. Importantly, our criterion does not remove the internal intermittency, and so does not remove the turbulence, and structures associated with it, from the subsequent analysis.

Chapter 5

Inertial Range Turbulence at Small Scales

In this chapter we investigate the trace anisotropy of the smallest temporal/spatial scales of the inertial range. These scales are particularly interesting because the MHD model is progressively less satisfied as the temporal/spatial scale of interest tends towards the ion inertial/gyro scale. Thus, in the last decade of the inertial range the MHD model may no longer be valid.

The primary reason that the MHD model becomes invalid as one approaches the ion inertial/gyro scale is that the gyration of the ions about the background magnetic field may no longer be neglected. However, at the ion inertial/gyro scale the electron gyration scale is small, as $m_e/m_i = 1836$, so the electron gyration may be neglected. As a result the single-fluid model of MHD is no longer sufficient to describe the two fluids of the ions and electrons.

The difference in velocity between the ions and the electron produces a current, $\mathbf{j} = -n_e e(\mathbf{v}_e - \mathbf{v}_i)$, where n_e is the number density, e is the electron charge, $\mathbf{v}_e$ is the electron velocity and $\mathbf{v}_i$ is the ion velocity [Goossens, 2003]. The current produced by the difference in ion and electron velocity leads to the Hall term of Ohm's law becoming increasingly significant as the spatial scale decreases (See Chapter 1 for the general Ohm's law). Therefore, Hall-MHD is an extension of MHD that attempts to include finite gyration effects, such that the induction equation may be written as $\partial\mathbf{B}/\partial t = \nabla \times (\mathbf{v} \times \mathbf{B} - (\mathbf{j} \times \mathbf{B})/en_e)$.

However, the solar wind is a weakly collisional plasma, so a fluid approach may be invalid. Howes [2009] demonstrated the limitations of Hall MHD by comparing the damping rates and dispersion relation of the linear eigenfrequencies with that calculated using a Vlasov-Maxwell kinetic theory. It was found that for the

a weakly collisional plasma with plasma $\beta_i = 1$ the Hall MHD model is unable to capture the $k_\parallel$ Alfvén branch of the dispersion relation.

In this chapter we investigate the trace power, which gives the reduced one-dimensional energy spectral estimate for $E(k_\parallel)$ and $E(k_\perp)$ in the solar wind at the small scales of the inertial range, such that kinetic and/or Hall effects become important.

We find that after filtering for discontinuities in the observations the $E(k_\parallel)$ spectrum displays an additional small scale behaviour that is consistent with Alfvén wave dispersion and/or dissipation, whereas the $E(k_\perp)$ spectrum displays constant scaling for all scales of the inertial range. Both results for $E(k_\parallel)$ and $E(k_\perp)$ are consistent with the findings of Howes [2009] when one considers the $k_\parallel$ and $k_\perp$ Alfvén branch obtained using Vlasov-Maxwell kinetic theory. This is the first clear detection of damping and/or dispersion for the $k_\parallel$ Alfvén branch at the small-scales of solar wind inertial range.

5.1 Data Sets

To investigate the smaller scales of the inertial range we use magnetometer data from STEREO-A. The magnetometer is over sampled at a cadence of 8 Hz, with noise dominating the signal at frequencies greater than 1 Hz. The advantages of using a STEREO satellite is the high magnetometer sampling frequency, the ability to observe large uninterrupted intervals and there is no spin-tone created from the satellite.

We select the five longest intervals of stable fast solar wind streams recorded by STEREO-A during 2008. The intervals are recorded during the following periods; January 18-22, February 13-17, March 12-18, June 18-21 and August 12-15, which from hereon will be referred to as interval I, II, III, IV and V respectively. We also consider a super ensemble composed of all the intervals, which is referred to as VI. Throughout this chapter we will display only interval I, II, III and VI, which are representative of all intervals.

In this chapter we will be investigating the trace anisotropy, and so the nonaxisymmetry found in Chapter 3 does not contribute to the spectral scaling of the trace anisotropy [Wicks et al., 2012]. We chose to investigate the small scales of the inertail range, such that we do not consider scales smaller than the ion cyclotron scale. Therefore, the group and/or phase speed of the $k_\parallel$ fast magnetoacoustic branch and the $k_\perp$ Alfvén branch that map to the Whistler and Kinetic Alfvén Wave (KAW) is still small compared to the solar wind flow. Therefore, for the

spatial-temporal scale of investigation all chosen intervals fulfill Taylor's hypothesis, such that $|\mathbf{V}_{SW}| \gg |\mathbf{V}_{p,g}|$, where $|\mathbf{V}_{sw}|$ and $|\mathbf{V}_{p,g}|$ are the magnitudes of the solar wind and the max[phase,group] velocity of the waves present [Tu and Marsch, 1995].

5.2 Method

In this chapter we will use the method described in chapter 4 for removing discontinuities. We define a scale-by-scale threshold as; $|\delta|\mathbf{B}\,(t,f)\,| - \delta B_{\parallel}(t,f)| < T_0 f^{-\beta}$, where t is the time index, f is the frequency of interest, $\delta|\mathbf{B}\,(t,f)\,|$ is the fluctuation of the modulus of the magnetic field, $\delta B_{\parallel}(t,f)$ is the parallel fluctuation with respect to the background magnetic field, T_0 and β are constants to be found from the interval. A discontinuity is detected for all times where the inequality is not satisfied. Using this method allows for an accurate estimate of the local background field across all scales used.

In this chapter we investigate the trace anisotropy using Taylor's hypothesis, such that the resulting one-dimensional spectral density observed will be $\tilde{P}_{ij}(f,\theta) = \int \mathrm{d}^3\mathbf{k} P_{ij}(\mathbf{k})\delta(2\pi f - \mathbf{k}\cdot\mathbf{V}_{sw})$, where $P_{ij}(k)$ is the energy spectral tensor and $\mathbf{k}\cdot\mathbf{V}_{SW} = 2\pi f$ is the plane in $\mathbf{k}$-space that is integrated over when using Taylor hypothesis to construct $\tilde{P}_{ij}(f,\theta)$. Using $\theta = 0^\circ - 10^\circ$ and $\theta = 80^\circ - 90^\circ$ we estimate the trace, $P_\theta^T = \Sigma_i \tilde{P}_{ii}$, for the parallel and perpendicular wave vector respectively. Thus the estimated energy spectrum for the perpendicular and parallel wave vectors normalized to the ion gyro-scale, ρ_i, may be written, $E(k_\perp \rho_i) = \Sigma_i \tilde{P}_{ii}(f/f_{c,i}, 80^\circ - 90^\circ)$ and $E(k_\parallel \rho_i) = \Sigma_i \tilde{P}_{ii}(f/f_{c,i}, 0^\circ - 10^\circ)$, where $f_{c,i}$ is the gyro-frequency of the ions as defined in Chapter 1.

We begin by demonstrating that there is a need to remove the influence of discontinuities at the small scales of the inertial range by plotting the PSD for the perpendicular and parallel variance with respect to the background magnetic field and the variance of the modulus of the magnetic field. These quantities are plotted in blue, red and black of Fig. 5.1 respectively. The solid and dashed lines correspond to mean of 10 subintervals and the uncertainty to a level of 90%.

One can see that the variance of the parallel component with respect to the background magnetic field displays scaling close to $f^{-1.8}$ for temporal-scale greater than the gyro-frequency of the ions, $f_{c,i} = 0.4 \pm 0.05$ Hz. However, the variance of the modulus of the magnetic field displays scaling close to $f^{-1.4}$. Similar scaling was observed in the Ulysses interval and surrogate time-series displayed in the previous chapter. One may see that the variance of the modulus of the magnetic field and the parallel component with respect to the background field become distinct at

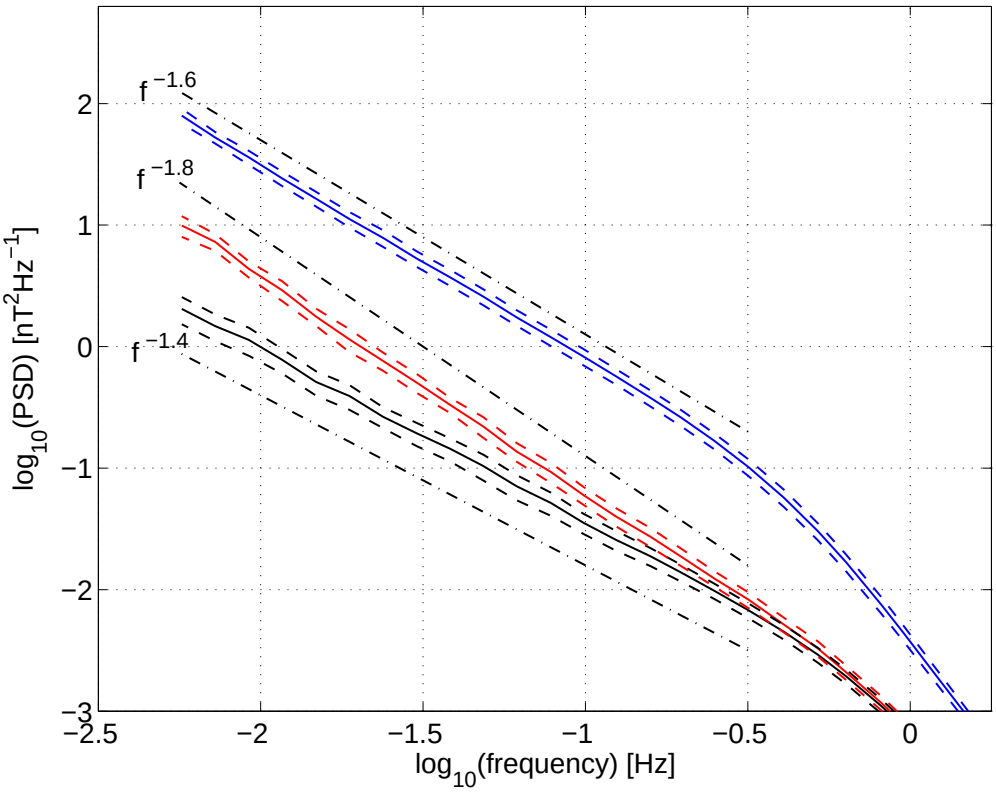

Figure 5.1: Variance anisotropy for interval III. The PSD for the variance of the perpendicular and parallel components with respect to the local background magnetic field and the modulus of the magnetic field are displayed in blue, red and black respectively. The solid and dashed lines display the mean across 10 subinterval and the spread to 90% certainty respectively. The black dot-dashed lines demonstrate specific scaling relations to be compared with the variance of the perpendicular and parallel components with respect to the local background magnetic field and the modulus of the magnetic field.

approximately half a decade of temporal scale less than the gyro-frequency, to a certainty of 90%. The significance to examining the variance of the small temporal-scales of the inertial range is two fold; i) one can see that for these temporal-scales there is a disagreement between $P_{\|}$ and $P_{|\mathbf{B}|}$, and so discontinuities must be considered, ii) it emerges from the variance analysis that there is no characteristic scale for which discontinuities emerge in temporal-scales of the inertial range, so no *a priori* assumption should be made regarding which temporal-scales should be filtered for discontinuities. Therefore, we apply our discontinuity filtering method from Chapter 4 to all temporal-scales of this investigation.

5.3 Results

In this section we will present the analysis of intervals I, II, III, and VI prior and post removal of discontinuities. We will present the trace anisotropy analysis prior to the removal of discontinuities to demonstrate that these intervals are "standard" fast solar wind intervals, in that the results are compatible with previous findings of Horbury et al. [2008]; Podesta [2009]; Wicks et al. [2010]; Chen et al. [2010]. These previous results, which do not filter for discontinuities, are interpreted as being in agreement with Goldreich and Sridhar [1995]. Then we will display the trace anisotropy that is found after discontinuities have been removed. Once discontinuities are excluded from the trace anisotropy analysis one can see that the additional scaling due to discontinuities serves to hide the small-scale anisotropy that results from kinetic effects, particularly in the $k_{\|}$ direction.

We begin by displaying the trace anisotropy prior to any filtering designed to remove discontinuities from the observational time-series. The trace anisotropy for intervals I, II, III, VI are shown in the top-left, top-right, bottom-left and bottom-right panels of Fig. 5.2 respectively. The estimated $E(k_{\|}\rho_i)$ and $E(k_{\perp}\rho_i)$ are presented in blue and red respectively. The solid and dashed lines demonstrate the average and 99% confidence level, calculated by separating the ensemble of $E(k_{\|}\rho_i)$ and $E(k_{\perp}\rho_i)$ data into 10 subintervals. Both $E(k_{\|}\rho_i)$ and $E(k_{\perp}\rho_i)$ in Fig. 5.2 have been multiplied by $f^{5/3}$ respectively, such that Kolmogorov-like scaling may be seen as a horizontal line. $E(k_{\perp}\rho_i)$ has been adjusted vertically so that approximate agreement may be seen with $E(k_{\|}\rho_i)$ at the largest scales.

One can see that the PSD for $E(k_{\perp}\rho_i)$ is approximately horizontal, and so approximately displays the "standard" Kolmogorov-like scaling. The scaling for $E(k_{\|}\rho_i)$ is steeper than that of $E(k_{\perp}\rho_i)$. Typically the reported observations are close to $E(k_{\|}\rho_i) \sim k_{\|}^{-2}$. Therefore, we plot the power spectral density estimate for

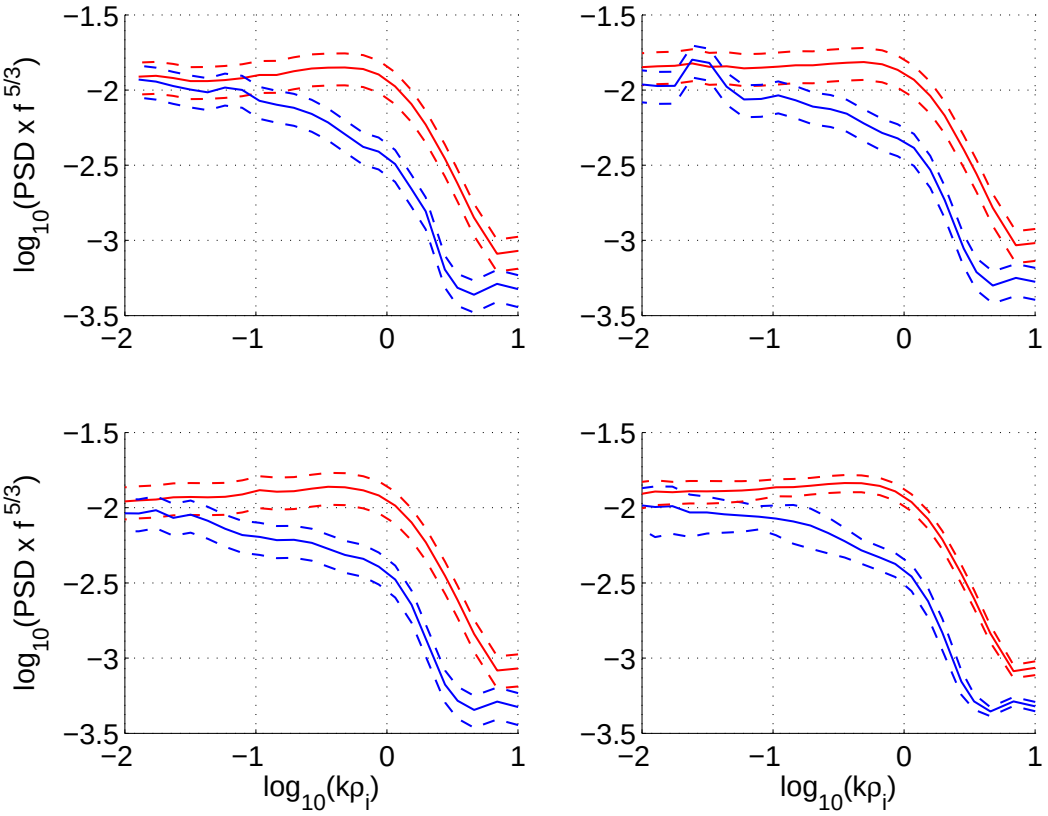

Figure 5.2: Compensated trace anisotropy prior to discontinuity filtering for intervals I, II, III and VI are displayed in the top-left, top-right, bottom-left and bottom-right panels. The estimated $E(k_{\|}\rho_i)$ and $E(k_{\perp}\rho_i)$ are presented in blue and red respectively. The solid and dashed lines demonstrate the average and 99% confidence level. The x-axis is in units of $k\rho_i$, where k is $k_{\|}$ and $k_{\perp}$ for the blue and red cases respectively. The PSD has been compensated by $f^{5/3}$ to highlight Kolmogorov-like scaling.

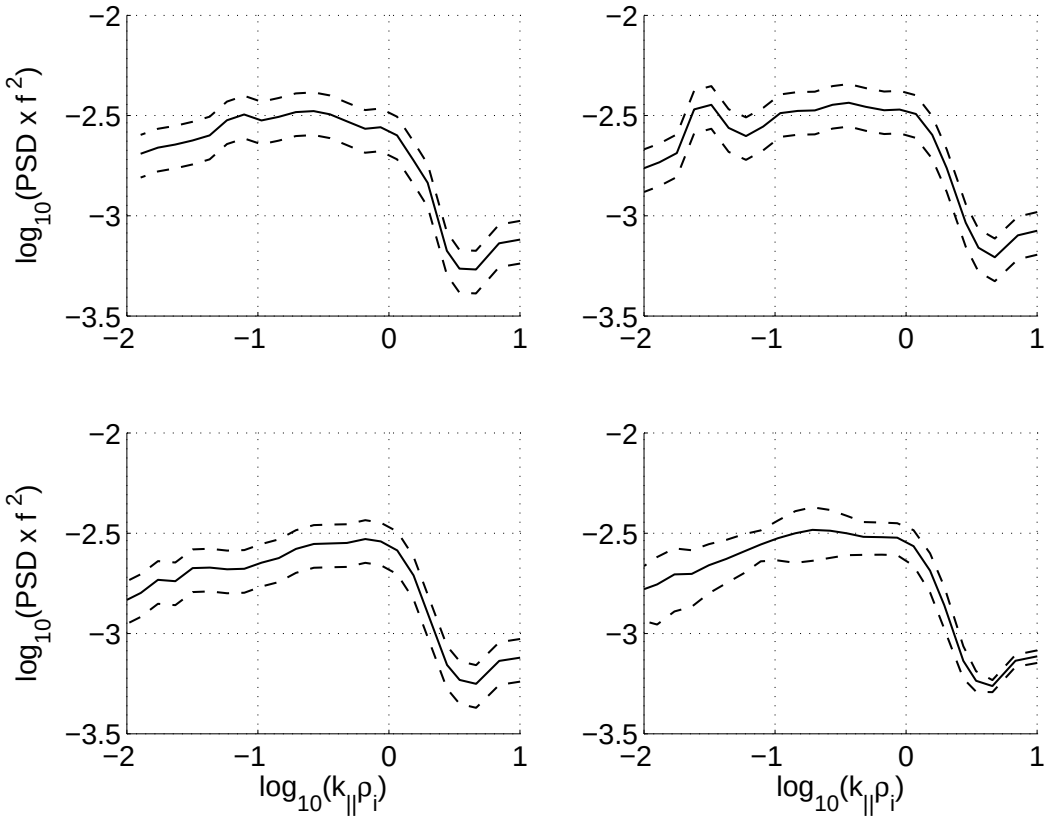

Figure 5.3: The estimated $E(k_{\|}\rho_i)$ prior to discontinuity filtering for intervals I, II, III and VI are displayed in the top-left, top-right, bottom-left and bottom-right panels. The solid and dashed lines demonstrate the average and 99% certainty. The PSD has been compensated by f^2.

$E(k_{\|}\rho_i)$ multiplying by f^2 in Fig. 5.3, where the solid and dashed lines demonstrate the average and 99% confidence level. One can see that the established result for $E(k_{\perp}, k_{\|})$ scaling that is consistent with Goldreich and Sridhar [1995] is recovered.

We now consider the case where the time-series discontinuities have been removed via the method described in chapter 4. The values of $[\beta, T_0]$ found for intervals I, II, III, IV, V and VI are $[0.64, 0.1931]$, $[0.62, 0.1931]$, $[0.61, 0.24]$, $[0.60, 0.1931]$, $[0.64, 0.1931]$, $[0.70, 0.1905]$ respectively. The filtered trace anisotropy for intervals I, II, III, VI are shown in the top-left, top-right, bottom-left and bottom-right panels of Fig. 5.4 respectively. The PSD estimates for $E(k_{\|}\rho_i)$ and $E(k_{\perp}\rho_i)$ are shown in blue and red respectively. Where the solid and dashed lines demonstrate the average and 99% certainty, calculated by separating the ensemble of $E(k_{\|}\rho_i)$ and $E(k_{\perp}\rho_i)$ data into 10 subintervals. The vertical axis has been compensated by multiplying the PSD by $f^{3/2}$

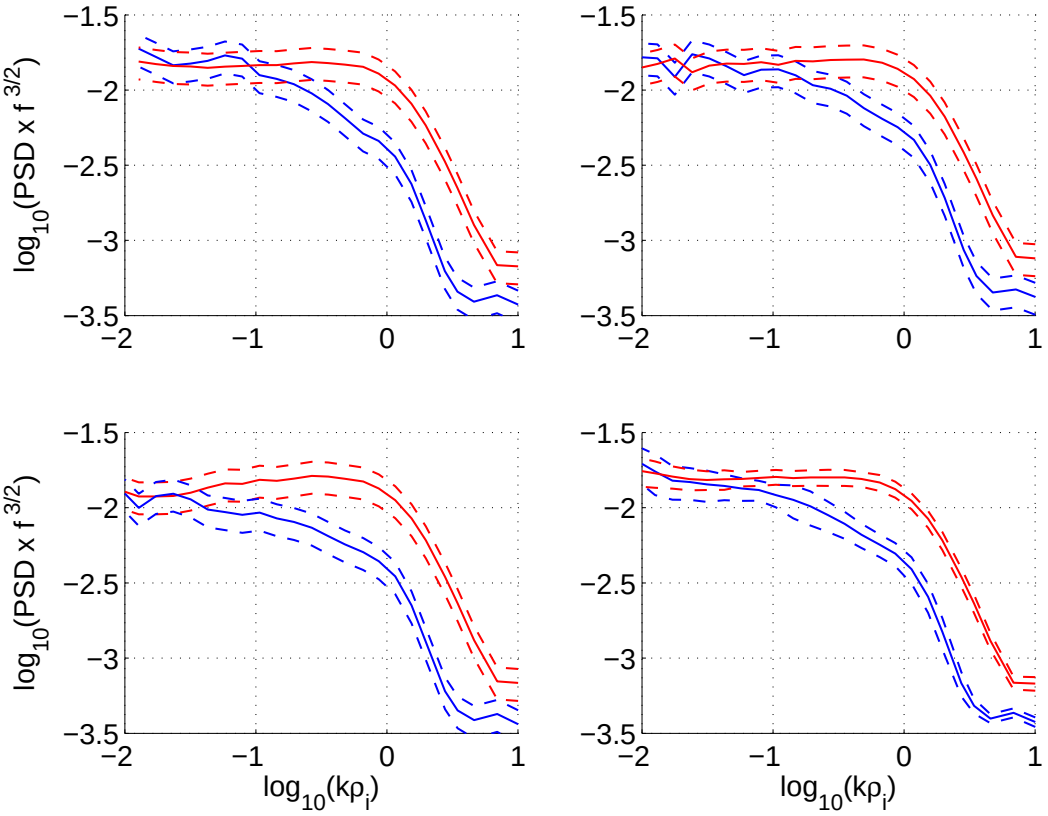

Figure 5.4: Compensated PSD of the trace anisotropy post discontinuity filtering for intervals I, II, III and VI are displayed in the top-left, top-right, bottom-left and bottom-right panels. The estimated $E(k_{\parallel}\rho_i)$ and $E(k_{\perp}\rho_i)$ are presented in blue and red respectively. The solid and dashed lines demonstrate the average and 99% certainty. The x-axis is in units of $k\rho_i$, where k is $k_{\parallel}$ and $k_{\perp}$ for the blue and red cases respectively. The PSD has been compensated by $f^{3/2}$ to highlight IK-like scaling.

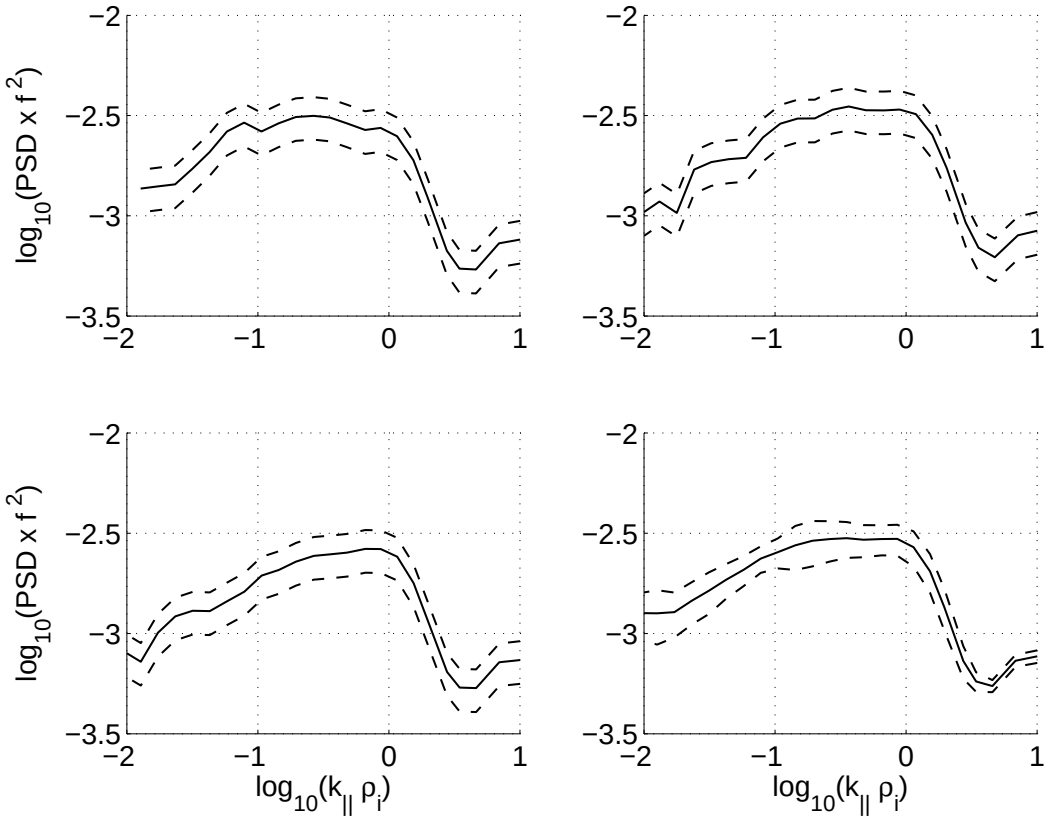

Figure 5.5: Compensated PSD of the estimated $E(k_{\|}\rho_i)$ post discontinuity filtering for intervals I, II, III and VI are displayed in the top-left, top-right, bottom-left and bottom-right panels. The solid and dashed lines demonstrate the average and 99% certainty. The x-axis is in units of $k_{\|}\rho_i$. The PSD has been compensated by f^2.

It can be seen that for the largest-scales shown, which corresponds approximately to scales greater than $k\rho_i \sim 0.1$, the estimated PSD for $E(k_{\|}\rho_i)$ and $E(k_{\perp}\rho_i)$ returns scaling consistent with that found from the Ulysses interval in chapter 4, that of $E(k_{\perp}\rho_i, k_{\|}\rho_i) \sim k^{-3/2}$. However, one can see that there is approximately a decade of steeper scaling in the range $k\rho_i \sim 0.1 - 1$ for $E(k_{\|}\rho_i)$. As in Fig. 5.3 we plot $E(k_{\|}\rho_i)$ multiplied by f^2. This may be seen in Fig. 5.5. One can see that the scaling for $E(k_{\|}\rho_i)$ between $k\rho_i \sim 0.1 - 1$ may be approximated by $E(k_{\|}) \sim k^{-2}$.

5.3.1 Discussion

By comparing Fig . 5.3 and Fig. 5.5, one can see that the region of interest is $k\rho_i \sim 0.1 - 1$. It is also important to understand why the power-law slope of $E(k_{\|}\rho_i)$ is affected and $E(k_{\perp}\rho_i)$ is unaffected in this region, as can be seen in Fig.

5.4. However, it is not possible to use MHD theory in this region. Therefore, we refer to two plots from Howes [2009] in order to understand the physics in this region.

The plots we refer to from Howes [2009] demonstrates the limitations of Hall MHD in a weakly collisional plasma, where Fig. 5.6 - 5.7 display the dispersion relation and dissipation rate for the linear eigenfrequencies of a weakly collisional plasma with $\beta_i = 1$ for $k_\parallel \rho_i$ and $k_\perp \rho_i$ respectively. The dispersion relation and dissipation rate for $k_\parallel \rho_i$ and $k_\perp \rho_i$ are shown in the top and bottom panels respectively. In the top panel the dispersion relation using Hall MHD and Vlasov-Maxwell kinetic theory are shown with dashed and dotted lines, where A', F', S' and A, F, S denote the Alfvén, fast and slow branch for both models respectively. The bottom panel displays the damping rate from Vlasov-Maxwell kinetic theory.

One can see that the $k_\parallel$ Alfvén branch undergoes both dispersion and dissipation in the range $k_\parallel d_i \sim 0.1 - 1$, note that d_i is the ion inertial length and is related to gyro-radii by $d_i = \rho_i/\sqrt{\beta_i}$, thus the two quantities are equivalent for $\beta_i = 1$. This is not the case for the $k_\perp$ Alfvén branch, which continues past the gyro-scale to become the kinetic Alfvén wave. We compare the behaviour of the Alfvén branch from Vlasov-Maxwell kinetic theory with the observations displayed in Fig. 5.4. One can see that $E(k_\perp \rho_i)$ is unchanged with a spectral index close to 3/2 until close to the ion gyro-scale, whereas $E(k_\parallel \rho_i)$ demonstrates a dramatic change in the region $k_\parallel \rho_i \sim 0.1 - 1$, where the spectral index changes from 3/2 to 2.

In the "collisionless" solar wind plasma it is hypothesized that the turbulent cascade is dominated by the interaction of Alfvén waves. As we can see from Fig. 5.6 the Alfvén waves are increasingly damped in the $k_\parallel$ direction, but not the $k_\perp$ direction. Therefore, it is reasonable to assume that the nonlinear Alfvén cascade with $k_\parallel$ will be increasingly damped in this region, whilst the cascade with $k_\perp$ will not be damped significantly. In principle this last decade of the inertial range may be able to fulfill a critical balance condition similar to Goldreich and Sridhar [1995], such that the turbulence becomes increasingly two-dimensional. If this were the case one would expect to observe $E(k_\parallel) \sim k_\parallel^{-2}$. However, as the perpendicular cascade is non-unique, we observe $E(k_\perp) \sim k_\perp^{-(5+\alpha)/(3+\alpha)}$, where $\alpha = 1$ would fit the observations here [Boldyrev, 2005].

This analysis suggests that discontinuities have affected conclusions drawn from observations in two ways; 1) with discontinuities present the trace anisotropy seems to support Goldreich and Sridhar [1995] across all scales of the inertial range, which is not seen when the discontinuities are removed. 2) with discontinuities present the interesting physics relating to $E(k_\parallel)$ in the range $k_\parallel d_i \sim 0.1 - 1$ is hidden, this region is a clear site of increased dispersion and/or dissipation once

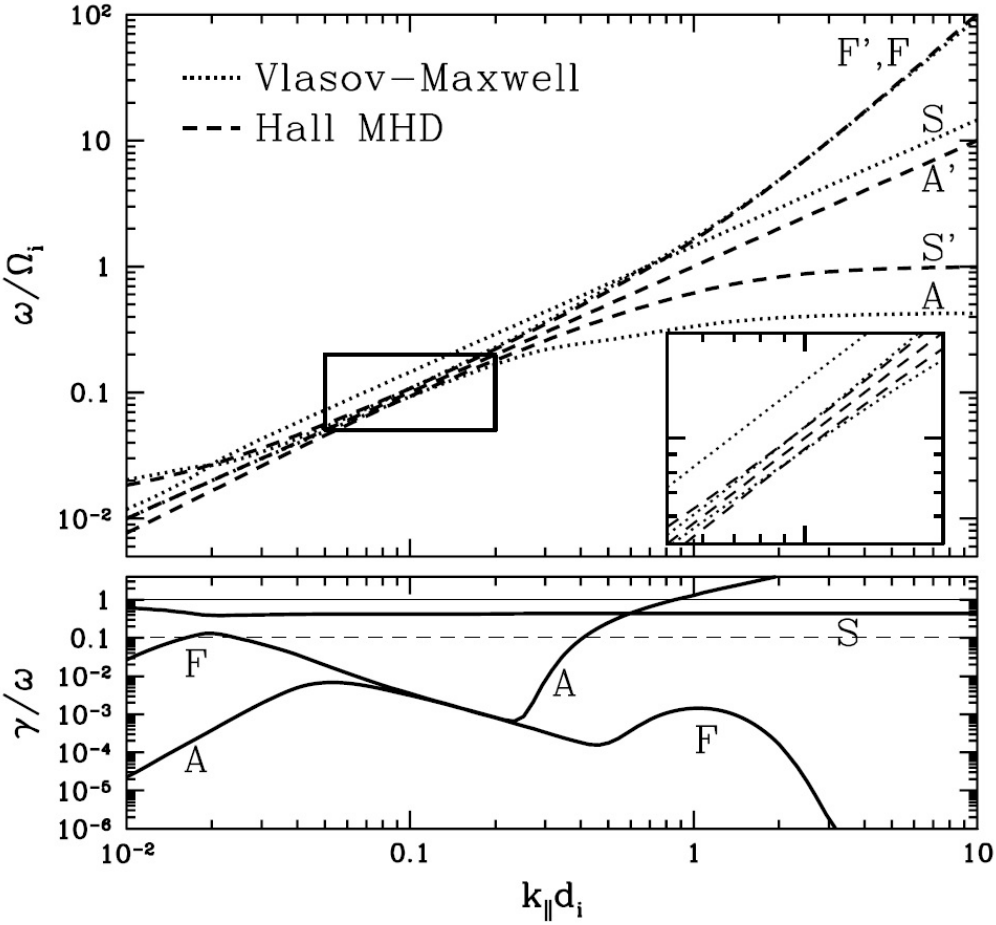

Figure 5.6: "Top: Normalized real frequency ω/Ω vs. parallel wavenumber $k_\parallel d_i$ for the Hall-MHD (dashed) fast (F'), Alfvén (A'), and slow (S') modes and for the kinetic theory (dotted) fast (F), Alfvén (A) and slow (S) modes for the parameters $\beta_0 = 1$, $T_i/T_e = 1$, and $k_\perp d_i = 10^{-2}$. Inset is an expanded view of the boxed region. Bottom: Normalized damping rate γ/ω vs. parallel wavenumber $k_\parallel d_i$ for the same three low-frequency modes from kinetic theory (solid)" after Howes [2009]

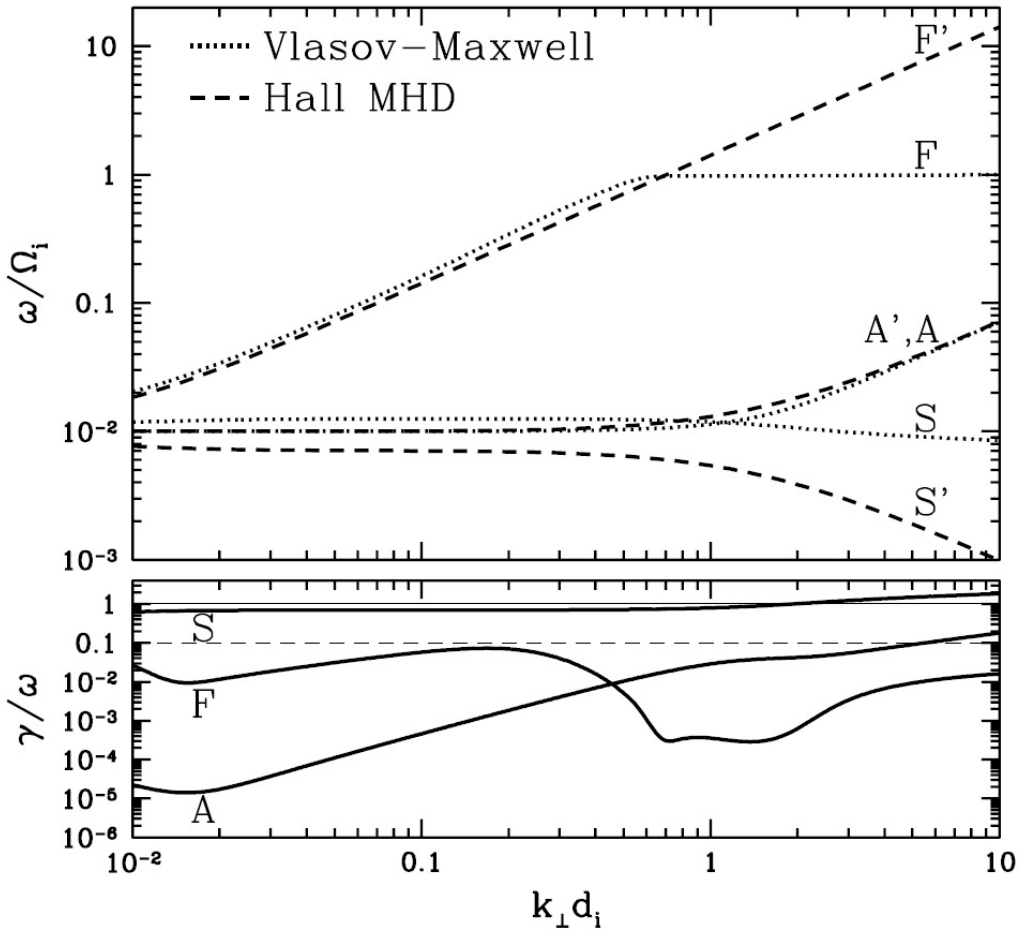

Figure 5.7: "Top: Normalized real frequency ω/Ω vs. perpendicular wavenumber $k_\perp d_i$ for the Hall-MHD (dashed) fast (F'), Alfvén (A'), and slow (S') modes and for the kinetic theory (dotted) fast (F), Alfvén (A) and slow (S) modes for the parameters $\beta_0 = 1$, $T_i/T_e = 1$, and $k_\parallel d_i = 10^{-2}$. Inset is an expanded view of the boxed region. Bottom: Normalized damping rate γ/ω vs. perpendicular wavenumber $k_\perp d_i$ for the same three low-frequency modes from kinetic theory (solid)" after Howes [2009]

discontinuities have been removed from the analysis.

Chapter 6

Conclusion of Thesis

In this thesis we have investigated the inertial range within the solar wind. We have found that the observed difference in variance power for the two perpendicular directions with respect to the background magnetic field is due primarily to sampling a solenoid field at-a-point with Taylor's hypothesis. This observed nonaxisymmetry may be used as a tool to distinguish between the theories of turbulence within the solar wind.

We have designed a criteria that is able to find non-turbulent discontinuities within the observational time-series. The discontinuities are then removed from subsequent analysis, mainly because the background magnetic field is not defined within a discontinuity. The removal of time-series discontinuities was shown to alter our understanding of standard turbulence analysis methods, such as the variance, trace and intermittency anisotropy with respect to the background magnetic field.

Finally we investigated the smallest temporal-spatial scales of the inertial range within the solar wind. We found that in the last decade of the inertial range the scaling of the $k_{\parallel}$ branch dramatically changed. We suggested that discontinuities have made this region undistinct in previous solar wind studies. We compared the $k_{\parallel}$ and $k_{\perp}$ observations to that predicted by kinetic theory in Howes [2009]. It was found that there was good agreement, and so, the observations are likely to correspond to dissipation and/or dispersion of the $k_{\parallel}$ Alfvén branch.

The commonly held picture of the solar wind is that there are three distinct scaling ranges, that of the f^{-1}, inertial and kinetic range of the PSD. Each of these ranges are regarded to have their own unique physical process, which may be investigated by a careful selection of spatial-temporal scales. This picture is demonstrated by Goldstein et al. [1995] in Fig. 6.1. We have found that this model for the solar wind is oversimplified, such that the correct selection of spatial-temporal

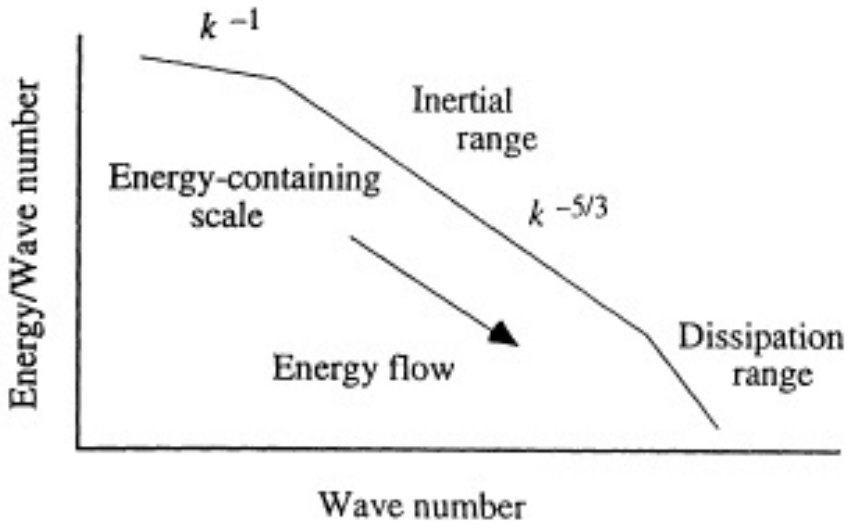

Figure 6.1: After figure 1 of Goldstein et al. [1995]. A schematic of the observed power spectrum of magnetic field fluctuations is shown, split into the three key areas of "Energy-containing scale", "Inertial range" and "Dissipation range".

scale alone is not sufficient to investigate turbulence within the inertial range.

A schematic of our interpretation of the solar wind as a function of spatial-temporal scale is displayed in Fig. 6.2. In our interpretation the solar wind is an inhomogeneous and structured medium on the large spatial-temporal scale, which is displayed in blue. We have found that the effect of structures ranges from the transition thickness of the structures to the largest spatial-temporal scales. It is also the waiting-time distribution between structures that is responsible for the f^{-1} scaling range observed. At the smallest scales of the inertial range the ion kinetics become significant, such that the $k_{\|}$ Alfvén branch becomes damped and dispersive. Therefore, the kinetic range may be argued to begin within the last decade of the inertial range. The scales at which the ion kinetics become important are shown in red. Between the two areas dominated by structures and kinetic effect is the inertial range, which is shown in yellow.

We have found that in order to investigate the turbulence within the inertial range one must also consider the effect of structures, for which there is an increasing power contribution to the PSD as the spatial-temporal scale increases. Importantly, once discontinuities are taken into account we have found no support for the Goldreich and Sridhar [1995] model in the solar wind.

The work within this thesis has been limited to the *in-situ* magnetic field measurements of the solar wind and the main implication of this work is that struc-

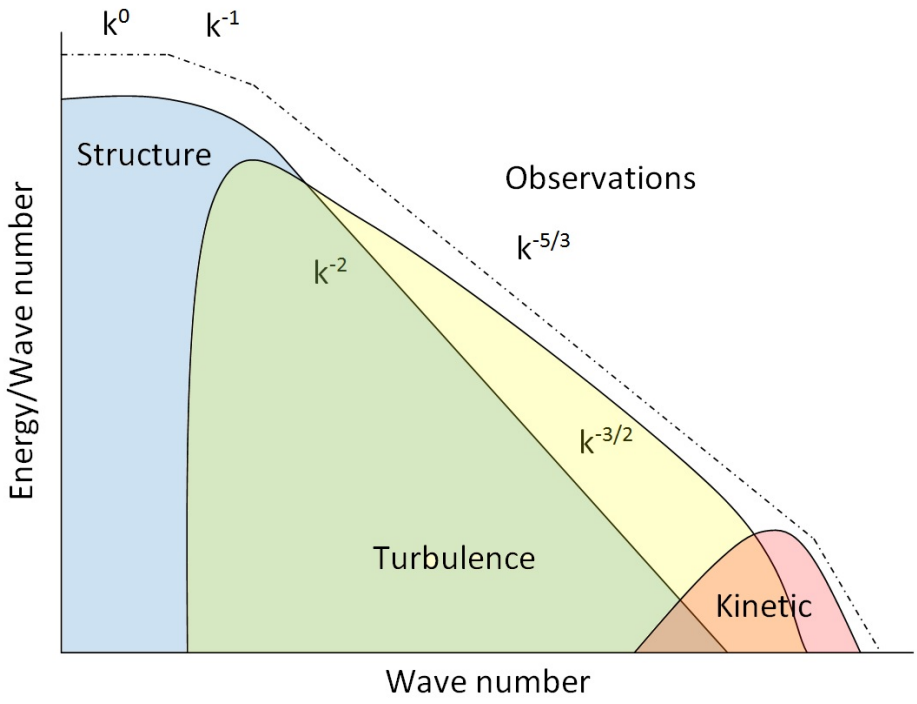

Figure 6.2: A schematic of the solar wind power spectral density for the magnetic field fluctuations. The observed power spectral density is shown by the dot-dashed line. However, the dominant physical process that contribute to the observed power spectral density are shown underneath, where the influence of structures, turbulence and kinetic physics are represented in blue, yellow and red respectively.

tures/discontinuities must be considered within solar wind analysis. Therefore, there are three clear directions of future study from this work; i) The development of other independent methods of detecting and removing discontinuities from the analysis, ii) investigate other fields within the solar wind (E.g Electric field, velocity, flux, Elsässer variables) and determine whether these quantities are susceptible to discontinuities within the solar wind, iii) revisit previous studies/surveys and determine if discontinuities within the observations were significant.

Bibliography

O. Alexandrova, A. Mangeney, M. Maksimovic, C. Lacombe, N. Cornilleau-Wehrlin, E. A. Lucek, P. M. E. DéCréAu, J.-M. Bosqued, P. Travnicek, and A. N. Fazakerley. Cluster observations of finite amplitude Alfvén waves and small-scale magnetic filaments downstream of a quasi-perpendicular shock. *Journal of Geophysical Research (Space Physics)*, 109:A05207, 2004.

H. Alfvén. Existence of electromagntic-hydrodynamic waves. *Nature*, 150:405, 1942.

A. Balogh, M. W. Dunlop, S. W. H. Cowley, D. J. Southwood, J. G. Thomlinson, K. H. Glassmeier, G. Musmann, H. Luhr, S. Buchert, M. H. Acuna, D. H. Fairfield, J. A. Slavin, W. Riedler, K. Schwingenschuh, and M. G. Kivelson. The Cluster Magnetic Field Investigation. *Space Science Reviews*, 79:65–91, 1997.

G. K. Batchelor. *The Theory of Homogeneous Turbulence*. Oxford University Press, 1953.

B. Bavassano, M. Dobrowolny, F. Mariani, and N. F. Ness. Radial evolution of power spectra of interplanetary Alfvenic turbulence. *Journal of Geophysical Research*, 87:3617–3622, 1982.

J. W. Belcher and Jr. L. Davis. Dynamics of the interplanetary gas and magnetic fields. *Journal of Geophysical Research*, 76(16):3534, 1971.

J. W. Belcher and C. V. Solodyna. Alfven waves and directional discontinuities in the interplanetary medium. *Journal of Geophysical Research*, 80:181, 1975.

A. Beresnyak and A. Lazarian. Strong imbalanced turbulence. *Astrophysical Journal*, 682:1070, 2008.

J. W. Bieber, W. Wanner, and W. H. Matthaeus. Dominant two-dimensional solar wind turbulence with implications for cosmic ray transport. *Journal of Geophysical Research*, 101:2511–2522, 1996.

D. Biskamp. *Magnetohydrodynamic Turbulence*. Oxford University Press, 2003.

T. Bohr, M. H. Jensen, G. Paladin, and A. Vulpiani. *Dynamical Systems Approach to Turbulence*. Oxford University Press, 1998.

S. Boldyrev. On the spectrum of magnetohydrodynamics. *Astrophysical Journal*, 626, 2005.

J. E. Borovsky. Flux tube texture of the solar wind: Strands of the magnetic carbet at 1 au? *Journal of Geophysical Research*, 113, 2008.

J. E. Borovsky. Contribution of Strong Discontinuities to the Power Spectrum of the Solar Wind. *Physical Review Letters*, 105(11):111102, 2010.

Roberto Bruno and Vincenzo Carbone. The solar wind as a turbulence laboratory. *Living Reviews in Solar Physics*, 2(4), 2005. URL `http://www.livingreviews.org/lrsp-2005-4`.

L. F. Burlaga. Directional Discontinuities in the Interplanetary Magnetic Field. *Solar Physics*, 7:54–71, 1969.

L. F. Burlaga. Intermittent turbulence in the solar wind. *Journal of Geophysical Research*, 96:5847, 1991.

L. F. Burlaga and J. M. Turner. Microscale 'alfven waves' in the solar wind at 1 au. *Journal of Geophysical Research*, 81:73, 1976.

C. Canuto, M. Y. Hussaini, A. Quarteroni, and T. A. Zang. *Spectral Methods in Fluid Dynamics*. Springer, 1991.

C. Canuto, M. Y. Hussaini, A. Quarteroni, and T. A. Zang. *Spectral Methods: Evolution to complex Geometries and Applications to Fluid Dynamics*. Springer, 2007.

J. P. Cassinelli. Stellar winds. *Annual Review of Astronomy and Astrophysics*, 17: 275, 1979.

B. D. G Chandran. Strong anisotropic mhd turbulence with cross helicity. *Astrophysical Journal*, 685:646, 2008.

S. C. Chang and A. Nishida. Spatial structure of transverse oscillations in the interplanetary magnetic field. *Astrophysics and Space Science*, 23:301, 1973.

C. H. K. Chen, T. S. Horbury, A. A. Schekochihin, R. T. Wicks, O. Alexandrova, and J. Mitchell. Anisotropy of solar wind turbulence between ion and electron scales. *Physical Review Letters*, 104:255002, 2010.

Jr. P. J. Coleman. Turbulence, viscosity, and dissipation in the solar-wind plasma. *Astrophysical Journal*, 153:371, 1968.

N. Cornilleau-Wehrlin, P. Chauveau, S. Louis, A. Meyer, J. M. Nappa, S. Perraut, L. Rezeau, P. Robert, A. Roux, C. de Villedary, Y. de Conchy, L. Friel, C. C. Harvey, D. Hubert, C. Lacombe, R. Manning, F. Wouters, F. Lefeuvre, M. Parrot, J. L. Pincon, B. Poirier, W. Kofman, and P. Louarn. The Cluster Spatio-Temporal Analysis of Field Fluctuations (STAFF) Experiment. *Space Science Reviews*, 79: 107–136, 1997.

P. A. Davidson. *Turbulence: An Introduction For Scientists and Engineers*. 2004.

K. U. Denskat, H. J. Beinroth, and F. M. Neubauer. Interplanetary magnetic field power spectra with frequencies from 2.4 x 10 to the -5th hz to 470 hz from helios-observations during solar minimum conditions. *Journal of Geophysics*, 54:60, 1983.

P. H. Diamond, S. I. Itoh, and K. Itoh. *Modern Plasma Physics. Volume 1: Physical Kinetics of Turbulent Plasmas*. Oxford University Press, 2010.

T. Dudok de Wit and V. V. Krasnosel'skikh. Non-gaussian statistics in space plasma turbulence: fractal properties and pitfalls. *Nonlinear Processes in Geophysics*, 3 (4):262–273, 1996.

W.M. Elsässer. The hydromagnetic equations. *Phys. Rev.*, 79:183, 1950.

M. Forman, R. T. Wicks, and T. S. Horbury. Detailed fit of "critical balance" theory to solar wind turbulence measurements. *Astrophysical Journal*, 733(2):76, 2011.

U. Frisch. *Turbulence*. Oxford University Press, 1995.

S. Galtier, S. V. Nazarenko, A. C. Newell, and A. Pouquet. A weak turbulence theory for incompressible magnetohydrodynamics. *Plasma Physics*, 63:447, 2000.

C. Gardiner. *Stochastic Methods: A handbook for the natural and social sciences*. Springer, 2003.

S. P. Gary and C. W. Smith. Short-wavelength turbulence in the solar wind: Linear theory of whistler and kinetic alfvén fluctuations. *Journal of Geophysical Research*, 114, 2009.

M. Ghil, M. R. Allen, M. D. Dettinger, K. Ide, D. Kondrashov, M. E. Mann, A. W. Robertson, A. Saunders, Y. Tian, F. Varadi, and P. Yiou. Advanced Spectral Methods for Climatic Time Series. *Reviews of Geophysics*, 40:1003, 2002.

G. Gogoberidze. On the nature of incompressible magnetohydrodynamic turbulence. *Physics of Plasmas*, 14:022304, 2007.

G. Gogoberidze, S. M. Mahajan, and S. Poedts. Weak and strong regimes of incompressible magnetohydrodynamics. *Physics of Plasmas*, 16:072304, 2009.

P. Goldreich and S. Sridhar. Towards a theory of interstellar turbulence. 2: Strong alfvénic turbulence. *Astrophysical Journal*, 438:763, 1995.

M. L. Goldstein. Major unsolved problems in space plasma physics. *Astrophysics and Space Science*, 277:349, 2001.

M. L. Goldstein and D. A. Roberts. Magnetohydrodynamic turbulence in the solar wind. *Physics of Plasmas*, 6:4154, 1999.

M. L. Goldstein, D. A. Roberts, and W. H. Matthaewus. Magnetohydrodynamic Turbulence in the Solar Wind. *Annual Review of Astronomy and Astrophysics*, 33:283, 1995.

M. Goossens. *An Introduction to Plasma Astrophysics and Magnetohydrodynamics*. Kluwer Academic Publishers, 2003.

R. Grappin and W.-C. Müller. Scaling and anisotropy in magnetohydrodynamic turbulence in a strong mean magnetic field. *Physics Review E*, 82(2):026406, 2010.

R. Grappin, W.-C. Müller, and Ö. Gürcan. Quasi-isotropic cascade in MHD turbulence with mean field. *ArXiv e-prints*, September 2012.

A. Guadagnini, S. P. Neuman, and M. Riva. Numerical investigation of apparent multifractality of samples from processes subordinated to trucated fbm. *Hydrological Processes*, 26:2894, 2012.

H. J. Haganaar, C. J. Schriver, and A. M. Title. The distribution of cell sizes of the solar chromosphere network. *Astrophysical Journal*, 481:998, 1997.

A. Hasegawa. Particle accelerated by mhd surface wave and formation of aurora. *Journal of Geophysical Research*, 81:5083, 1976.

T. S. Horbury and A. Balogh. Structure function measurements of the intermittent mhd turbulent cascade. *Nonlinear Processes in Geophysics*, 4:185, 1997.

T. S. Horbury, A. Balogh, R. J. Forsyth, and E. J. Smith. The rate of turbulent evolution over the sun's poles. *Astronomy and Astrophysics*, 101:405, 1996.

T. S. Horbury, M. Forman, and S. Oughton. Anisotropic scaling of magnetohydrodynamics. *Physical Review Letters*, 101(17):175005, 2008.

G. G. Howes. Limitations of hall mhd as a model for turbulence in weakly collisional plasmas. *Nonlinear Processes in Geophysics*, 16:219, 2009.

P. S. Iroshnikov. Turbulence of a conduction fluid in a strong magnetic filed. *Astronomicheskii Zhurnal*, 40(4):742, 1963.

K. Jacobs. *Stochastic Processes for Physics: Understanding Noisy Systems*. Oxford University Press, 2010.

B. B. Kadomstev. *Plasma Turbulence*. Academic, New York, 1965.

M. G. Kivelson and C. T. Russell. *Introduction to Space Physics*. Oxford University Press, 1995.

K. Kiyani, S. C. Chapman, and B. Hnat. Extracting the scaling exponents of a self-affine, non-Gaussian process from a finite-length time series. *Physics Review E*, 74(5):051122, 2006.

K. H. Kiyani, S. C. Chapman, and N. W. Watkins. Pseudononstationarity in the scaling exponents of finite-interval time series. *Physics Review E*, 79(3):036109, 2009.

K. H. Kiyani, S. C. Chapman, F. Sahraoui, B. Hnat, O. Fauvarque, and Y. V. Khotyaintsev. Enhanced Magnetic Compressibility and Isotropic Scale Invariance at Sub-ion Larmor Scales in Solar Wind Turbulence. *Astrophysical Journal*, 763: 10, 2013.

L. W. Klein, D. A. Roberts, and M. L. Goldstein. Anisotropy and minimum variance directions of solar wind fluctuations in the outer heliosphere. *Journal of Geophysical Research*, 96:3779, 1991.

B. Knaepen and R. Moteau. Magnetohydrodyuanmic turbulence at low magnetic reynolds number. *Annual Review of Fluid Mechanics*, 40:25, 2008.

A. N. Kolmogorov. Disspation of energy in locally isotropic turbulence. *Proc. R. Soc. Lond. A*, 434:15, 1991.

R. H. Kraichnan. Inertial-range spectrum of hydromagnetic turbulence. *The Physics of Fluids*, 8(7), 1965.

N. A. Krall and A. W. Trivelpiece. *Principles of Plasma Physics*. McGraw-Hill Inc., US, 1973.

L. D. Landau and E. M. Lifshitz. *Quantum Mechanics (Non-Relativistic Theory), Course of Theoretically Physics*. Pergamon, 1977.

R. P. Lepping and K. W. Behannon. Magnetic field directional discontinuities - Characteristics between 0.46 and 1.0 AU. *Journal of Geophysical Research*, 91: 8725–8741, 1986.

M. Lesieur. *Turbulence in Fluids Third Revised and Enlarged Edition*. Kluwer Academic Publishers, 1997.

G. Li. Identifying Current-Sheet-like Structures in the Solar Wind. *Astrophysical Journal*, 672:L65–L68, 2008.

G. Li, B. Mioa, Q. Hu, and G. Qin. Effect of current sheets on the solar wind magnetic field power spectrum from the ulysses observations: From kraichnan to kolmogorov scaling. *Physical Review Letters*, 106(12):125001, 2011.

Y. Lithwick, P. Goldreich, and S. Sridhar. Imbalanced strong mhd turbulence. *Astrophysical Journal*, 655:269, 2007.

R. L. Lysak and W. Lotko. On the kinetic dispersion relation for shear alfvén waves. *Journal of Geophysical Research*, 101:5085, 1996.

F. Mariani, B. Bavassano, U. Villante, and N. F. Ness. Variations of the occurrence rate of discontinuities in the interplanetary magnetic field. *Journal of Geophysical Research*, 78:8011, 1973.

E. Marsch and C. Y. Tu. On the radial evolution of mhd turbulence in the inner heliosphere. *Journal of Geophysical Research*, 95:8211, 1990.

L. N. Martin, P. Dmitruk, and D. O. Gomez. Energy spectrum, dissipation, and spatial structures in reduced hall magnetohydrodynamics. *Physics of Plasmas*, 19:052305, 2012.

W. H. Matthaeus and M. L. Goldstein. Measurement of the rugged invariants of magnetohydrodynamic turbulence in the solar wind. *Journal of Geophysical Research*, 87:10347, 1982.

W. H. Matthaeus, M. L. Goldstein, and J. H. King. An interplanetary magnetic field ensemble at 1 au. *Journal of Geophysical Research*, 91(1):59, 1986.

W. H. Matthaeus, M. L. Goldstein, and D. A. Roberts. Evidence for the presence of quasi-two-dimensional nearly incompressible fluctuations in the solar wind. *Journal of Geophysical Research*, 95:20673–20683, 1990.

W. H. Matthaeus, S. Servidio, P. Dmitruk, V. Carbone, S. Oughton, M. Wan, and K. T. Osman. Local Anisotropy, Higher Order Statistics, and Turbulence Spectra. *Astrophysical Journal*, 750:103, 2012.

P. Moin and K. Mahesh. Direct numerical simulation: A tool for turbulence research. *Annual Review of Fluid Mechanics*, 30:539, 1998.

W. C. Müller and R. Grappin. Spectral energy dynamics in magnetohydrodynamic turbulence. *Physical Review Letters*, 95:114502, 2005.

NASA. sunspots, 2013a. URL `http://http://solarscience.msfc.nasa.gov/images/bfly.gif`.

NASA. sun, 2013b. URL `http://umbra.nascom.nasa.gov/images/`.

N. F. Ness, C. S. Scearce, and S. Cantarano. Preliminary results from the pioneer 6 magnetic field experiment. *Journal of Geophysical Research*, 71(13):3305, 1966.

M. Neugebauer, D. R. Clay, B. E. Goldstein, B. T. Tsurutani, and R. D. Zwickl. A reexamination of rotational and tangential discontinuities in the solar wind. *Journal of Geophysical Research*, 89:5395–5408, 1984.

A. M. Oboukhov. On the distribution of energy in the spectrum of a turbulent flow. 32:22, 1941.

E. N. Parker. Dynamics of the interplanetary gas and magnetic fields. *Astrophysical Journal*, 128:664, 1958.

G. Paschmann and P. W. Daly. *Analysis Methods for Multi-Spacecraft Data*. International Space Science Institute, 1998.

J. C. Perez and S. Boldyrev. Role of cross-helicity in magnetohydrodynamic turbulence. *Physical Review Letters*, 102:025003, 2009.

S. Perri and A. Balogh. Stationarity in solar wind flows. *The Astrophysical Journal*, 714(1):937, 2010.

S. Perri, E. Yordanova, V. Carbone, P. Veltri, L. Sorriso-Valvo, R. Bruno, and M. André. Magnetic turbulence in space plasmas: Scale-dependent effects of anisotropy. *Journal of Geophysical Research*, 114, 2009.

F. Plunian, R. Stepanov, and P. Frick. Shell models of magnetohydrodynamics turbulence. *Physics Reports*, 523:1, 2013.

J. J. Podesta. Dependence of solar-wind power spectra on the direction of the local mean magnetic field. *Astrophysical Journal*, 698(2):986, 2009.

H. Politano and A. Pouquet. Model of intermittency in magnetohydrodynamic turbulence. *Physics Review E*, 52:636, 1995.

O. Reynolds. An experimental investigation of the circumstances which determine whether the motion of water shall be direct and sinuous, and the law of resistance in parallel channels. *Phil. Trans. Roy. Soc.*, page 51, 1883.

L. F. Richardson. Atmospheric diffusion shown on a distance-neighbour graph. *Proc. R. Soc. A.*, 110:709, 1926.

R. S. Rogallo and P. Moin. Numerical simulations of turbulent flows. *Annual Review of Fluid Mechanics*, 16:99, 1984.

T. Roudier and R. Muller. Structure of the solar granulation. *Sol. Phys.*, 107:11, 1986.

C. S. Salem, G. G. Howes, D. Sundkvist, S. D. Bale, C. C. Chaston, C. H. K. Chen, and F. S. Mozer. Identification of kinetic alfvén wave turbulence in the solar wind. *Astrophysical Journal*, 745(1), 2012.

T. Schreiber and A. Schmitz. Surrogate time series. *Physica D Nonlinear Phenomena*, 142:346–382, 2000.

A. Shalchi. *Nonlinear Cosmic Ray Diffusion Theories*. Springer, 2009.

Z. S. She and E. Leveque. Universal scaling laws in fully developed turbulence. *Physical Review Letters*, 72:336, 1994.

R. A. Shine, G. W. Simon, and N. E. Hurlburt. Supergranule and mesogranule evolution. *Sol. Phys.*, 193:313, 2000.

G. W. Simon and R. B. Leighton. Velocity feilds in the solar atmosphere. Part III: Large-scale motion, the chromospheric network, and magnetic fields. *Astrophysical Journal*, 140:1120, 1964.

B. U. Ö. Sonnerup and Jr. L. J. Cahill. Magnetopause structure and attitude from explorer 12 observations. *Journal of Geophysical Research*, 72(1):171, 1967.

R. Srikanth, J. Singh, and K. P. Raju. Distribution of supergranule sizes. *Astrophysical Journal*, 534:1008, 2000.

F. R. Stephenson. Historical evidence concerning the sun: Interpretation of sunspot records during the telescopic and pretelescopic eras. *Royal Society of London Philosophical Transactions, Series A*, 330:499, 1990.

S. P. Sutera and R. Skalak. The history of poiseuille's law. *Annual Review of Fluid Mechanics*, 25:1, 1993.

G. I. Taylor. The specrtum of turbulence. *Proc. R. Soc. A.*, 164:476, 1938.

J. M. TenBarge, J. J. Podesta, K. G. Klein, and G. G. Howes. Interpreting Magnetic Variance Anisotropy Measurements in the Solar Wind. *Astrophysical Journal*, 753: 107, 2012.

J.A. Tessein, C. W. Smith, B. T. MacBride, W. H. Matthaeus, M. A. Forman, and J.E. Borovsky. Spectral indices for multi-dimensional interplanetary turbulence at 1 au. *Astrophysical Journal*, 692:684, 2009.

K. M. Thieme, E. Marsch, and R. Schwenn. Spatial structures in high-speed streams as signatures of fine structures in coronal holes. *Annales Geophysicae*, 8:713, 1990.

A. M. Title, T. D. Tarbell, K. P. Topka, S. H. Ferguson, R. A. Shine, and the SOUP Team. Statistical properties of solar granulation derived from the SOUP instrument on Spacelab 2. *Astrophysical Journal*, 336:475, 1989.

B. T. Tsurutani and E. J. Smith. Interplanetary discontinuities - Temporal variations and the radial gradient from 1 to 8.5 AU. *Journal of Geophysical Research*, 84:2773–2787, 1979.

C. Y. Tu and E. Marsch. *MHD Structures, Waves and Turbulence in the Solar Wind*. Kluwer Academic Publishers, 1995.

C.-Y. Tu, Z.-Y Pu, and F.-S. Wei. The power spectrum of interplanetary alfvenic fluctuations derivation of the governing equation and its solution. *Journal of Geophysical Research*, 89:13575, 1984.

B. J. Vasquez, C. W. Smith, K. Hamilton, B. T. MacBride, and R. J. Leamon. Evaluation of the turbulent energy cascade rates from the upper inertial range in the solar wind at 1 AU. *Journal of Geophysical Research (Space Physics)*, 112: A07101, 2007.

P. Veltri and A. Mangeney. Scaling laws and intermittent structures in solar wind MHD turbulence. In S. R. Habbal, R. Esser, J. V. Hollweg, and P. A. Isenberg, editors, *American Institute of Physics Conference Series*, volume 471 of *American Institute of Physics Conference Series*, pages 543–546, 1999.

M. Wan, K. T. Osman, W. H. Matthaeus, and S. Oughton. Investigation of intermittency in magnetohydrodynamics and solar wind turbulence: Scale-dependent kurtosis. *Astrophysical Journal*, 744:6, 2012.

R. T. Wicks, T. S. Horbury, C. H. K. Chen, and A. A. Schekochihin. Power and spectral index anisotropy of the entire inertial range of turbulence in the fast solar wind. 407(1), 2010.

R. T. Wicks, M. A. Forman, T. S. Horbury, and S. Oughton. Power Anisotropy in the Magnetic Field Power Spectral Tensor of Solar Wind Turbulence. *Astrophysical Journal*, 746:103, 2012.

V. Zhdankin, S. Boldyrev, J. Mason, and J. C. Perez. Magnetic Discontinuities in Magnetohydrodynamic Turbulence and in the Solar Wind. *Physical Review Letters*, 108(17):175004, 2012.